Conductivity-Based Nanocomposite Structural Health Monitoring via Electrical Impedance Tomography

by

Tyler N. Tallman

A dissertation submitted in partial fulfillment
of the requirements for the degree of
Doctor of Philosophy
(Mechanical Engineering)
in the University of Michigan
2015

Doctoral Committee:

Professor Kon-Well Wang, Chair
Professor Bogdan Epureanu
Professor Jerome P. Lynch
Emeritus Professor Anthony M. Waas

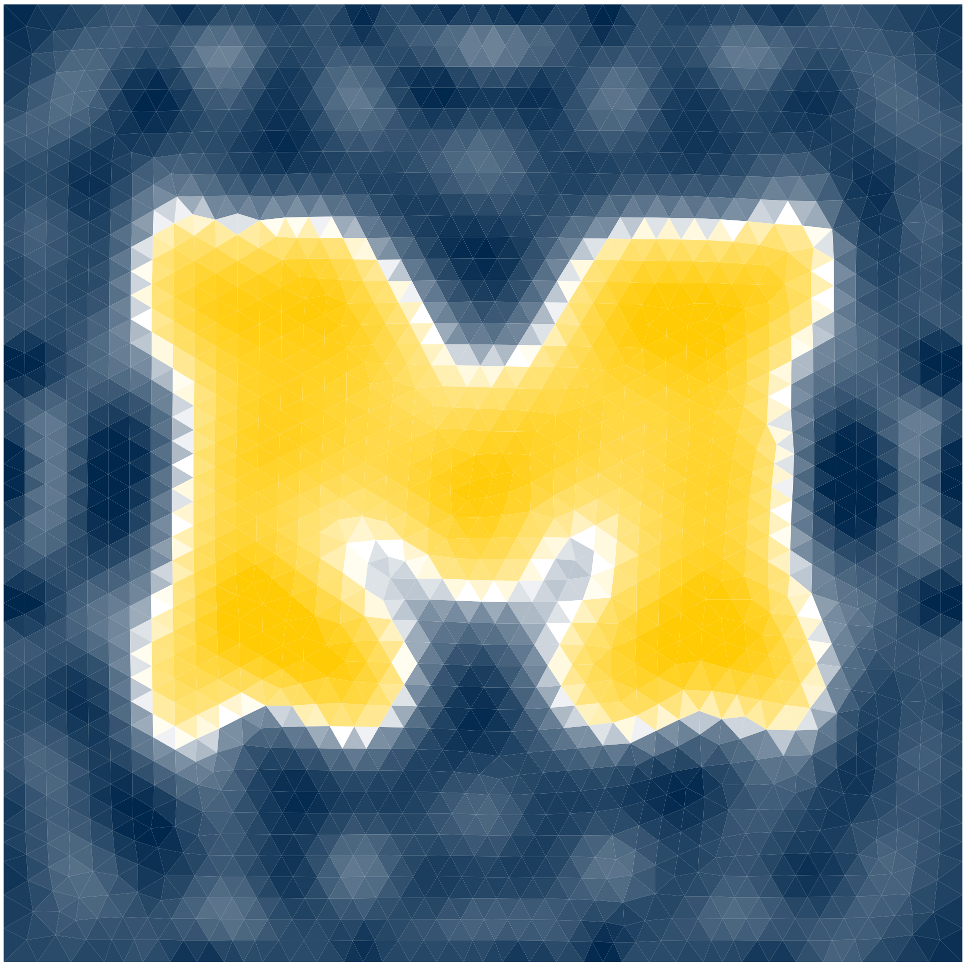

For Cat.

ACKNOWLEDGMENTS

First and foremost, I want to thank my advisor, Professor Kon-Well Wang. I feel truly blessed to have had such an outstanding advisor and mentor for my doctoral experience. Thank you, Professor Wang.

I gratefully thank my committee members, Professor Bogdan Epureanu, Professor Jerome Lynch, and Professor Anthony Waas for enlightening conversations, expert insight, and even letting me use lab equipment.

Much of this work proceeded under a collaborative project with colleagues at Penn State University. I gratefully thank Professor Charles Bakis and his former student Dr. Sila Gungor for manufacturing the nanocomposites and being excellent collaborators.

I also want to thank Professor Fabio Semperlotti. His daily help and guidance was invaluable when I started graduate school.

Thank you, Royan D'Mello (EIS at elevated temperatures), Sunil Pai and Solver Thorsson (GFRP impact), Andrew Burton (CNF/PU tensile testing), and Dr. Pilar Herrera-Fierro (SEM imaging) for your experimental assistance.

This research has been supported by the US Army Research Office (W911NF-10-1-00267), the National Science Foundation (CMMI-DS-1232436), and the Michigan Space Grant Consortium Fellowship. I gratefully thank these sponsors.

Thank you for your day-to-day help, past and present SDCL'ers.

Lastly, I thank my friends and family for making my time at Michigan pretty great.

TABLE OF CONTENTS

Chapter

LIST OF FIGURES

LIST OF APPENDICES

LIST OF ABBREVIATIONS

CB carbon black

CEM complete electrode model

CFRP carbon fiber reinforced polymer

CNF carbon nanofiber

CNT carbon nanotube

DAQ data acquisition

EIS electrical impedance spectroscopy

EIT electrical impedance tomography

GFRP glass fiber reinforced polymer

MAP maximum a posteriori

MWCNT multi wall carbon nanotube

PANI polyaniline

PDIPM primal-dual interior point method

PSS polysodium styrene-4-sulfonate

PU polyurethane

PVA polyvinyl alcohol

PVC polyvinyl chloride

PVDF polyvinylidene fluoride

SEM scanning electron microscope

SHM structural health monitoring

SWCNT single wall carbon nanotube

ABSTRACT

Conductivity-Based Nanocomposite Structural Health Monitoring via Electrical Impedance Tomography

by

Tyler N. Tallman

Chair: Kon-Well Wang

Nanocomposites have incredible potential when integrated as matrices in fiber-reinforced composites for transformative conductivity-based structural health monitoring (SHM). Key to this potential is the dependence of nanocomposite conductivity on well-connected nanofiller networks. Damage that severs the network or strain that affects the connectivity will manifest as a conductivity change. These damage or strain-induced conductivity changes can then be detected and spatially located by electrical impedance tomography (EIT). The nanofiller network therefore acts as an integrated sensor network giving unprecedented insight into the mechanical state of the structure.

Despite the potential of combining nanocomposite matrices with EIT, important limitations exist. EIT, for example, requires large electrode arrays that are too unwieldy to be practically implemented on in-service structures. EIT also tends to be insensitive to small, highly localized conductivity losses as is expected from common modes fiber-reinforced composite damage such as matrix cracking and delamination. Furthermore, there are gaps in the fundamental understanding of nanocomposite conductivity.

This thesis advances the state of the art by addressing the aforementioned limitations of EIT for conductivity-based SHM. This is done by insightfully leveraging the unique properties of nanocomposite conductivity to circumvent EIT's limitations. First, nanocomposite conductive properties are studied. This results in fundamental contributions to the understanding of nanocomposite piezoresistivity, the influence of nanofiller alignment on transverse percolation and conductivity, and conductivity evolution due to electrical loading. Next, the potential of EIT for conductivity-based health monitoring is studied and demonstrated for damage detection in carbon nanofiber (CNF)/epoxy and glass fiber/epoxy laminates manufactured with carbon black (CB) filler and for strain detection in CNF/polyurethane (PU). Lastly, the previously developed insights into nanocomposite conductive properties and damage detection via EIT are combined to greatly enhance EIT for SHM. This is done by first exploring how the sensitivity of EIT to delamination can be enhanced through nanofiller alignment and tailoring. A method of coupling the EIT image reconstruction process with known conductivity changes such as those induced by straining piezoresistive nanocomposites is developed and presented. This approach will tremendously bolster the image quality of EIT or, synonymously, significantly abate the number of electrodes required by EIT.

In achieving the aforementioned, important scholarly contributions are made to the fundamental understanding of nanocomposite conductivity and enhancing EIT. Important broader impacts are also made by not only demonstrating the potential of EIT for SHM but also by developing the framework through which EIT can be markedly enhanced to transform it into a powerful imaging technique.

CHAPTER 1

Literature Review

1.1 Introduction

Laminated fiber-reinforced polymer composites such as glass fiber reinforced polymer (GFRP) are becoming increasingly embraced as primary structural materials due to their high strength, low weight, and superior fatigue characteristics. Despite these advantages, laminated composites are susceptible to damage not normally found in traditional engineering alloys such as delaminations or the separation of fibrous layers induced by low-velocity impacts, high load cycles, or excessive loads. Delaminations considerably reduce structural stiffness and if left unaddressed can lead to failure [9]. These considerations are extremely important in aerospace applications employing structural composites because of the effects of highcycle fatigue-induced damage and the possibility of ballistic impacts with environmental debris. Aircraft structural failures can have devastatingly catastrophic consequences; therefore, accurate and reliable damage identification is crucial to ensuring operational safety. Accurate damage detection, however, is challenging in fiber-reinforced composites. Delaminations, for example, develop internally without outwardly visible warnings. Furthermore, damage accumulation in composites tends to be progressive in nature beginning with the formation of matrix cracks that propagate into delamination and eventually fiber fracture. In compression-dominated structures, matrix damage itself can cause sufficient stiffness reduction to effect an end-of-life situation. Matrix integrity is therefore critical to ensuring operational safety [10]. A robust detection scheme could significantly abate the potential consequences of damage in fiber-reinforced composites by ensuring damages are detected at their onset so that the structure can either be removed from service or repaired.

Traditional design approaches are based on damage tolerance and allow certain amounts of noncritical damage to accumulate in composites between inspection intervals. This approach requires a good understanding of damage growth rates, the effects of damage on stiffness, and the effects of damage on structural strength. As an alternative, SHM is gaining acceptance in structural maintenance. Quite generally defined, SHM is any process by which damage is detected, located, and characterized in engineering structures; it continuously monitors the condition of a structure thereby reducing the cost of unnecessary inspections while simultaneously providing real-time signals to prompt inspections only when necessary. SHM for fibrous composites needs to be sensitive to small defects such as matrix cracking and delamination initiation. To this end, a variety of SHM techniques have been researched including vibration testing, embedded sensing, guided wave sensing, and conductance monitoring. An important realization of SHM research is that no single approach is ideal for every structure, and the limitations of any method are important to identify. The methods summarized below are well-suited to a myriad of applications, but their limitations regarding the health monitoring of fiber-reinforced composites are tersely summarized.

Vibration testing monitors the response of a structure in either the time domain or the frequency domain through natural frequency, mode shape, dynamically measured flexibility, matrix update, or neural-network based methods. These approaches typically excite structures at low frequencies thereby engaging low-order modes and natural frequencies. Damage is expected to manifest as a local stiffness reduction that alters the mode shapes or natural frequencies. Because low-order modes typically have characteristic lengths greatly exceeding that of matrix cracking or delamination initiation, they are not sensitive to incipient damage in fiber-reinforced composites [11] [12].

Embedded sensing SHM encompasses any approach that requires the application of discrete sensors built into or onto the structure. Strain gauges, fiber optic sensors, and embedded carbon nanotube (CNT) threads are examples of embedded sensors [13] [14] [15]. These approaches have two important limitations. First, because of their discrete nature, they are insensitive to damage sufficiently removed from the sensor. And, second, embedding a sensor inevitably introduces stress concentrations where it is embedded. Stress concentrations are especially important to laminated composites because failure will most likely initiate at these points [10].

Guided wave sensing excites a structure by forcing stress waves to follow paths defined by the material properties of the structure. High-frequency guided wave techniques such as Lamb wave tomography interrogate structures with wavelengths that are small enough to discern matrix cracking [16] [17]. It is the author's opinion that guided wave methods have considerable potential for composite SHM, and interested readers are directed to the preceding citations for a much more detailed treatment. Guided wave methods, however, do require mechanically active (often piezoelectric) sensors/actuators be embedded into the structure. This can be difficult in fiber-reinforced composites [3].

Conductance-based monitoring schemes locate damage by identifying changes in diffusive properties. Electrical diffusion is most often employed, but thermal diffusion has also been studied [18]. Electrical conductivity-based SHM initially received attention in carbon fiber reinforced polymer (CFRP) composites in which the carbon fibers are the conducting phase, and fiber breakage will result in a loss of conductivity [19] [20] [21] [22] [23]. However, this approach is not sensitive to matrix damage, and delamination initiation may therefore go undetected.

A different approach to conductivity-based SHM is herein studied in which carbon nanofillers are utilized to impart conductivity to the matrix of fiber-reinforced composites. With the addition of a pervasive, well-connect nanofiller network, the matrix itself becomes self-sensing and the nanofillers act as an integrated sensor network giving unprecedented insight into the mechanical state of the matrix. To better envision this, consider the mechanism of conductivity in nanocomposites. That is, nanocomposites depend on well-connected nanofiller networks for electrical conductivity. Electrons traverse the network by traveling along the highly conductive nanofillers and tunneling between sufficiently proximate fillers. Damage that severs the nanofiller network will manifest as a loss of conductivity centralized in the area of the damage. This is depicted qualitatively in Figure 1.1.

This approach has considerable potential for composite SHM because it addresses the limitations of the previously described methods. First, because nanofillers are exceedingly diminutive, incipient damage will greatly exceed their characteristic dimensions thereby ensuring sensitivity to small damages. Second, a well-connected and pervasive nanofiller network will ensure sensitivity throughout the composite structure. Third, nanofillers are of negligible parasitic weight and result in no decrease in mechanical properties of the fiber-reinforced composite. The addition of nanofillers can actually enhance the mechanical properties of fiber-reinforced composites [24] [25] [26]. And, finally, the sensing elements in conductivity-based methods are not mechanically active.

State of the art conductivity-based damage identification is summarized in the following sections. These methods can be broadly categorized as either nanocomposite matrix/resistance change methods or sensing layer/tomographic methods. A brief introduction to nanocomposites and nanofillers, however, is presented first.

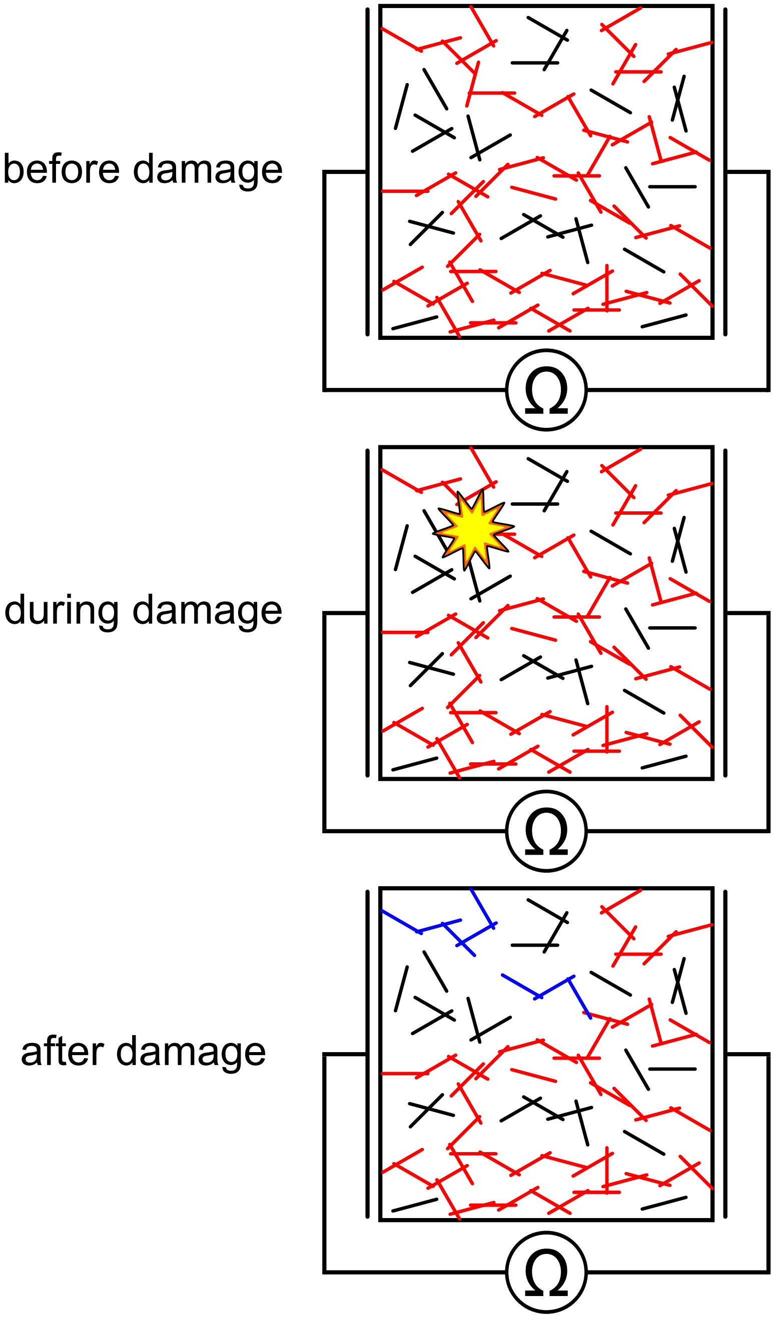

Figure 1.1: Qualitative depiction of damage-induced conductivity loss. Top: nanofillers are dispersed in a matrix. A well-connected network exists as shown in red such that resistance can be measured across the material. Middle: some damage event occurs. This could be, for example, an impact, delamination, or matrix cracking. Bottom: as a result of the damage event, the connection between nanofillers has been severed in the region of the blue fillers. There is now a measurable difference in material resistance because there are fewer connected paths of nanofillers spanning the domain.

1.2 Nanocomposites and Nanofillers

Because nanocomposites are so prevalent in this work, it is worth having some introduction to them. An exhaustive review regarding the properties of nanocomposites certainly exceeds the scope of this study; however, interested readers are directed to an excellent and thorough review written by Thostenson, Li, and Chou [27]. Nonetheless, quite generally, a nanocomposite is an encompassing term that refers to a multiphase material consisting of a matrix phase and a filler phase with characteristic filler dimensions expressible in nanometers. These fillers are typically CNTs, CNFs, or CB. Representative images of these fillers can be seen in Figure 1.2.

Since their discovery [28], CNTs have received tremendous attention due to their excellent mechanical (elastic modulus of 270 - 1500 GPa [29] [30], tensile strength of 10 - 500 GPa [29]), electrical (conductivity of 102 - 107 S/m [31]), and thermal properties (conductivity of 3000 - 6000 W/m-K [29]). Structurally, they are nearly one-dimensional with aspect ratios that can exceed 1000 and are formed from single or multiple concentric cylinders of rolled-up sheets of graphene [32] [33]. CNT nanocomposites have also been studied for their potential in damage detection [34] [35] [36], strain sensing [6] [37] [38] [7] [39], damping enhancement [40] [41] [42], electrical conductivity enhancement [43] [44] [45], and mechanical enhancement [46] [24].

CNFs are hollow fibers of stacked graphene frusta. Like CNTs, they have exceptionally high aspect ratios ranging from 250 - 2000 [29]. However, they are considerably less expensive than CNTs while retaining very good mechanical (elastic modulus of 240 GPa, tensile strength of 2.92 GPa [47]), electrical (conductivity of 105 S/m [48]), and thermal properties (conductivity of 1950 W/m-K [49]). CNFs also contribute considerable mechanical enhancement to composites [24] [25] [26].

CNT fillers and CNF fillers are attractive because their high aspect ratios enable percolation and low weight fractions [50] [51]. However, high aspect ratios also make them difficult to disperse among structural fibers without entanglement. Conversely, because CB fillers form as stacks of several hexagonal carbon rings, they have much lower aspect ratios and are more easily dispersed among structural fibers [52]. For this reason, CB is often preferred in the development of fiber-reinforced composites.

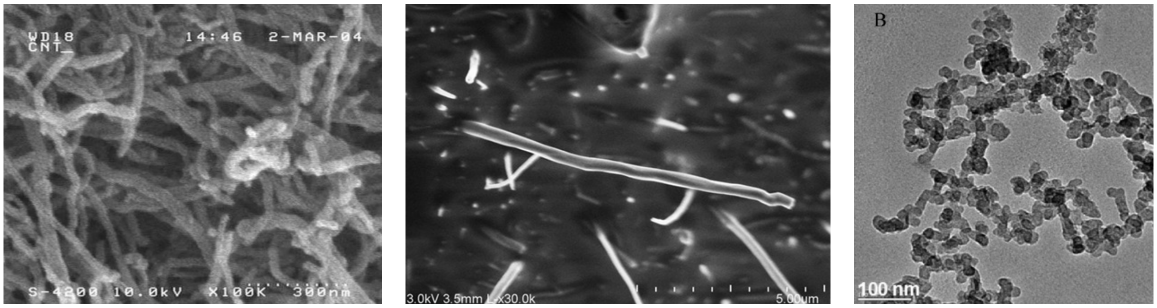

Figure 1.2: Representative examples of nanofillers Left: cluster of MWCNTs imaged via TEM [1]. Middle: single CNF imaged via SEM as part of this thesis work. Right: cluster of CB imaged via SEM [2].

1.3 Nanocomposite Matrix/Resistance Change Methods

1.3.1 Beam Structures

Employing nanocomposites as matrices in fiber-reinforced composites extends self-sensing capabilities to structural elements. This is a tremendous advantage over many types of SHM because the sensing network (i.e. the nanofillers) becomes an inherent part of the structure. Because of this, nanocomposite matrix methods have received considerable attention. The simplest structural elements are characterized by one dimension wherein resistance is measured before, after, or during loading scenarios at two points along the length of a beam by electrodes spanning the width of the beam. This approach provides valuable insight into the correlation between resistance and damage initiation, propagation, and accumulation. However, damage location cannot be discerned beyond the fact that it has occurred between the electrodes. Resistance generally increases linearly with load prior to failure and returns to an initial value for low load cycles. Resistance increases dramatically at failure initiation (typically micro-cracking of the matrix) and is irreversible. Resistance then continues to irreversibly accumulate as loading continues after failure initiation. These conclusions agree well with intuition. Tensile loads will increase or decrease the spacing between fillers. As a result, electrons have diminished or enhanced probability of tunneling thereby changing the conductivity of the composite. As long as the load is within the linear elastic regime, the inter-filler spacing should return to its original value. However, this may change with plastic deformation or fatigue loading after which the nanofillers may not return to their unloaded configurations. Additionally, failure such as micro-cracking induces a change in filler spacing that cannot be recovered. Continued damage accumulation will continue to eliminate conductive pathways effectively increasing composite resistivity.

Because the exact electrical response of a fiber-reinforced composite with a nanocomposite matrix varies greatly with the specific type of nanocomposite and loading, it is difficult to arrive at general conclusions beyond the aforementioned. However, there is valuable insight to be gained by studying specific works. To that end, specific contributions to nanocomposite matrix/resistance change methods are summarized in the following.

Thostenson and Chou [53] fabricated a five-ply, unidirectional, glass-fiber/epoxy laminate with 0.5 wt.% multi wall carbon nanotube (MWCNT)s dispersed in the epoxy. The center ply of the laminate was cut at the middle in order to promote delamination during tensile loading. Resistance was measured during tensile loading, and resistance increased linearly with load until delamination initiation. Upon delamination initiation, the resistance jumped dramatically and continued to increase at an increasing rate as the load increased. A $[0/90]_s$ cross-ply was similarly subjected to tensile loads where resistance was observed to increase linearly with load until the initiation of micro-cracking at which time the resistance jumped markedly and continued to increase at a substantial rate. It was noted that in both specimens that there was only a slight reduction in stiffness at damage initiation, but there was a substantial change in resistance.

Böger, Wichmann, Meyer, and Schulte [34] manufactured a glass fiber/epoxy laminate modified by the addition of MWCNTs and CB at 0.3 wt.%. The composite was subjected to interlaminar shear strength tests, incremental tensile tests, and fatigue tests while resistance was measured. The interlaminar shear strength was measured according to ASTM D-2344. Only a nominal increase in interlaminar shear strength due to nanofillers was recorded. A substantial increase in resistance was measured at failure. The incremental tensile tests subjected the composite to loading cycles that went from zero strain to an increasing maximum strain. Resistance measurements scaled linearly with strain and returned to the unstrained resistance for five cycles. After five cycles, resistance measurements returned to a larger unstrained resistance indicating the accumulation of irreversible damage. Lastly, dynamic tests were performed in order to induce fatigue loading. A decrease in stiffness of the composite was observed accompanied by an increase in resistance.

Nofar, Hoa, and Pugh [35] manufactured GFRP plates with 1 wt.% MWCNTs incorporated into the epoxy matrix. Upon curing, composite plates were cut into beams according to ASTM D-3039 and subjected to static tensile tests during which resistance was measured between two points along the length of the beam. Resistance increased linearly with strain until the beams' elastic limit was reached. Beyond the elastic limit the resistance increased dramatically implying the initiation of irreversible damage between the measurement points. The tensile test was then repeated with four measurement points along the length of the beam. Utilizing additional measurement points enabled rudimentary damage location by monitoring which measurement pair detected the largest increase in resistance at failure. Response to fatigue loading was also studied. It was found that resistance increases significantly less for cyclic loads below the elastic limit.

Gao, Thostenson, Zhang, and Chou [54] manufactured cross-ply E-glass/vinyl ester composite laminates with MWCNTs dispersed throughout the matrix. Quasi-static and cyclic tensile loading tests were performed during which specimen resistance was measured and acoustic emission counts were recorded. The length-normalized resistance change and acoustic emission counts trended similarly with strain for the initial quasi-static loading. However, length-normalized resistance change and acoustic emission counts trended significantly differently for subsequent quasi-static reloads. This implies that the resistance changes correspond to micro-damages or cracks that produce acoustic events. Reloading simply reopens cracks producing no acoustic events. Incremental cyclic loading resulted in increasing irreversible damage marked by increasing unloaded resistance. Acoustic emission counts increased with increasing increments again implying the formation of new micro-damages or cracks that were marked by increases in resistance.

Kim et al. [55] studied the damage mechanism of 3D braided composites manufactured with MWCNTs by resistance change methods. MWCNTs were dispersed by three-roll mill calendaring in a vinyl ester monomer, and vacuum-assisted resin transfer molding was used to produce the braided composites. 10 mm × 1.75 mm samples were prepared for tensile testing. Tensile testing was conducted at a cross-head speed of 1.27 mm/min while a constant voltage was applied across the specimens. Current was measured and the corresponding specimen resistance calculated. The observed resistance change was then categorized into five stages based on the slope of the resistance change curve. The different slopes of the resistance change curve were attributed to different damage mechanisms or the evolution of damage mechanisms as straining progressed. Damage initially took the form of transverse cracks and micro-delaminations, then matrix cracking at the interface between tow and matrix, accumulation of micro-delaminations or transverse cracks, saturation of micro-delaminations, and finally closing of micro-delaminations through Poisson effects. These mechanisms were then confirmed by X-ray computed tomography.

Gao et al. [56] investigated the influence of nanofiller dispersion uniformity on damage sensing characteristics in glass fiber/epoxy laminates with a stacking sequence of [0/90_2/0]. MWCNTs were uniformly dispersed by three-roll milling while non-uniform dispersions were achieved by using a nanotube-containing fiber sizing agent. The resulting panels were cut into 0.5 in wide strips and loaded in quasi-static and incremental cyclic tension at 1.27 mm/min. It was concluded that both uniform and non-uniform dispersions are capable of creating percolated nanofiller networks for conductivity-based damage detection. Furthermore, filler agglomeration is responsible for much lower resistance changes in non-uniformly dispersed networks. However, the use of a sizing agent was much more convenient during manufacturing.

Gao et al. [57] explored the influence of impacts on resistance change in six-layer epoxy/plain glass fiber manufactured with SC-15 epoxy resin containing CNTs (solid content of 6.2%). Upon curing, the composite panel was cut into 10.2 cm × 15.2 cm sections. 7.62 cm silver paint electrodes were then applied on the opposing 10.2 cm edges such that resistance could be measured along the 15.2 cm direction. 70 J impacts were then induced in the center of the plate, and the resistance change ratio was measured for repeated impacts. It was found that resistance increases with each new impact up to a 120% change after 11 loadings.

Pedrazzoli, Dorigato, and Pegoretti [58] modified the epoxy matrix of a glass fiber laminate with 2 wt.% CB and CNF. The CB/CNF ratio was 90/10. A two component epoxy resin was used with EC157 epoxy base constituted by a mixture of Bisphenol A/Bisphenol F/Hexanediol diglycidyl ether and W152 LR amminic hardener. The laminate measured 300 mm × 300 mm, was made from six layers of balanced E glass woven fabric, and was approximately 0.7 - 0.9 mm thick upon curing. Quasi-static tensile tests and creep tests were performed on 250 mm × 15 mm specimens cut from the original laminate by using a MTS 858-Mini Bionix servo-hydraulic testing machine, and resistance along the length of the beams was monitored during mechanical testing. Monotonic tensile tests were conducted at a constant cross head rate of 2 mm/s. The specimens were loaded until failure (approximately 2.25% strain), and resistance increased linearly for less than 1% strain. A rapid increase in resistance change rate was observed just before failure. This resistance trend is consistent with the formation of irreversible damage and cracking. Creep tests were performed by loading specimens at stress levels from 100 MPa to 350 MPa at temperatures ranging from 20 °C to 90 °C for 3600 seconds. Resistance initially spiked due to the creep load; however, as the experiment progressed, the resistance decayed exponentially to a constant value. The rate of decay was greater at lower temperatures, and the constant value to which the resistance decayed was greater at elevated temperatures. It was hypothesized that this behavior is a result of the nanofiller network initially responding to the high load. When deformational process kinetics are reduced at lower temperatures, nanoparticles are able to reform conductive networks thereby causing the measured resistance to decay. But, at elevated temperatures, higher strain rates may hinder reformation of conductive paths.

1.3.2 Plate Structures

Two-dimensional resistance change methods in plate structures are a natural extension of the previously described one-dimensional resistance change methods and endeavor to identify where damage occurs in fiber-reinforced plates with nanocomposite matrices. The simplest approach to locating damage in a plate structure is to instrument the plate with an array or a grid of electrodes. Resistance between neighboring electrode pairs is compared before and after damage, and damage is assumed to have occurred between electrode pairs that register the largest change in resistance. Applying an electrode grid to one side of a plate enables in-plane measurements while applying an electrode grid to both sides of a plate enables through-thickness measurements. Damage is often simulated by drilling holes through the plate or by impacting the plate. In-plane measurements are better suited for locating through-hole damage, but through-thickness measurements are better suited for locating sub-surface damage such as delaminations that are induced by impacts. A tightly packed grid will have better resolution but will require more electrodes. While able to coarsely locate damage, electrode grid methods require a surfeit of electrodes or measurement points making them unpalatable for integrated SHM as detailed below.

Zhang et al. [3] modified glass fiber/epoxy unidirectional $[0]_{10}$ and $[45/0/\text{-}45/90]_s$ laminates with 2 wt.% CB or 2 wt.% CB and copper chloride (CC). Unidirectional specimens were machined into beams measuring 150 mm × 20 mm × 4 mm for double cantilever beam and end notched flexure tests to determine the influence of nanofillers on Mode I and Mode II fracture toughness respectively. Mode I fracture toughness was measured according to ASTM D-5528, and Mode II fracture toughness was measured according to ESIS in a three-point bending configuration. Electrodes covering the width of the beams were applied to measure the through-thickness resistance. Nanofillers increased Mode I fracture toughness at the onset of delamination by 13.3% and the Mode I fracture toughness average plateau value by 8.6%. Mode II fracture toughness at the onset of delamination increased by 22.4% and the Mode II fracture toughness average plateau value increased by 18.7%. A departure from linear increase in resistance was observed in both tests as delamination initiated. The $[45/0/\text{-}45/90]_s$ laminate was trimmed to 150 mm × 100 mm, and a 9 × 9 grid of electrodes was attached to the top and bottom surfaces for through-thickness measurements. Nine electrodes were also attached along each edge for in-plane measurements so that the two methods could be compared. The plate was drop-weight impacted according to ASTM D-7136M/D-7136M-05 at 6.7 J/mm. Glass fiber/epoxy laminate samples were impacted multiple times at various fractions of the standard energy. Impact damage was imaged by weighting and interpolating resistance changes between electrodes before and after damage, and damage location and progression was captured. While the approach was successful at locating damage, it is a resistance change technique with discrete measurements interpolated for ease of visibility, not tomography. C-scans verified damage detection. A comparison of impact detection by in-plane electrodes and through-thickness electrodes can be seen in Figure 1.3 and Figure 1.4 respectively.

Viets, Kaysser, and Schulte [4] manufactured 16-layer, unidirectional, glass-fiber laminates modified with 1 wt.% MWCNTs and 12 wt.% CB using Epikote RIMR 135 epoxy resin with RIMH 137 amine hardener. Two plates were cut to final dimensions of 120 mm × 120 mm × 3 mm. Ten parallel lines of conductive silver ink were applied on the top and bottom of each laminate. Lines on top were perpendicular to the $0\,^{\circ}$-fiber direction and lines on bottom were parallel to the $0\,^{\circ}$-fiber direction. Resistance measurements were taken through the thickness where lines intersected. The plates were then impacted with an impact energy of 7.65 J. Comparing resistance before and after impact, a map of resistance changes was generated by interpolating resistance changes at each measurement point. These maps showed a pronounced change in conductivity centered about the impact. Ultrasonic C-scan verified sub-surface and barely visible damage. A schematic of the electrode placement used in this research and the resulting damage detection is shown in Figure 1.5.

Naghashpour and Van Hoa [59] fabricated three-layer textile composite plates with MWCNT loadings at 0.1, 0.2, 0.25, 0.3, 0.4, and 1 wt.%. A grid of 40 electrodes was attached on the plate surface. Resistances between electrode pairs were measured before and after damage, and damage was located by identifying the electrode pair that registers the largest resistance change. Two types of damage were studied – through-holes of various sizes and at various locations and impact caused by collision with high velocity projectiles and drop weights. Their results indicated that sensitivity to damage decreases as nanofiller loading increases; however, loadings just above the percolation threshold result in non-uniform distributions. Therefore, a tradeoff exists between optimal sensitivity and uniform distribution. Holes as small as 1/16" in diameter could be detected although sensitivity to small damages decreased dramatically in the presence of larger damages. Nonetheless, multiple holes could also be detected. Impact damages as small as 1 J and as large as 78 J could be detected. The accuracy of damage location for this method is limited by the coarseness of the electrode grid.

Naghashpour and Hoa [5] also manufactured carbon fiber/epoxy plates with 0.3 wt.% MWCNTs using three-mill rolling. Electrodes were then attached to a 13 in × 22 in plate such that 4-point measurement could be made at grid points. A novel strategy was proposed to circumvent limitations imposed by contact resistance wherein two measurement points are associated with each grid point. This measurement approach was then used to detect

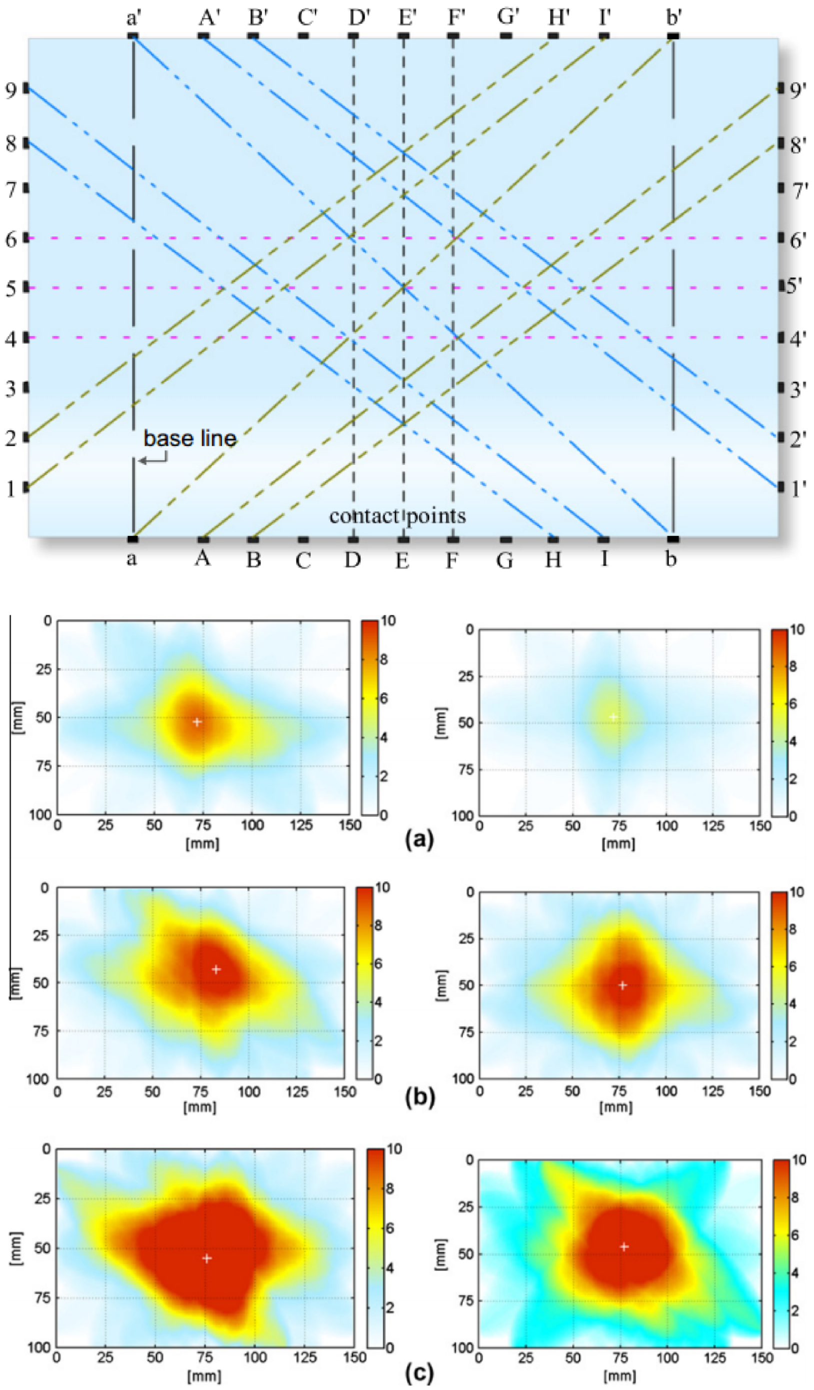

Figure 1.3: Schematic of in-plane measurement points by Zhang et al. [3] and detection of imacts at (from top to bottom) 50, 100, and 150% of 6.7 J/mm for 2.0 wt. % CB (left) and 2.0 wt. % CB and CC (right).

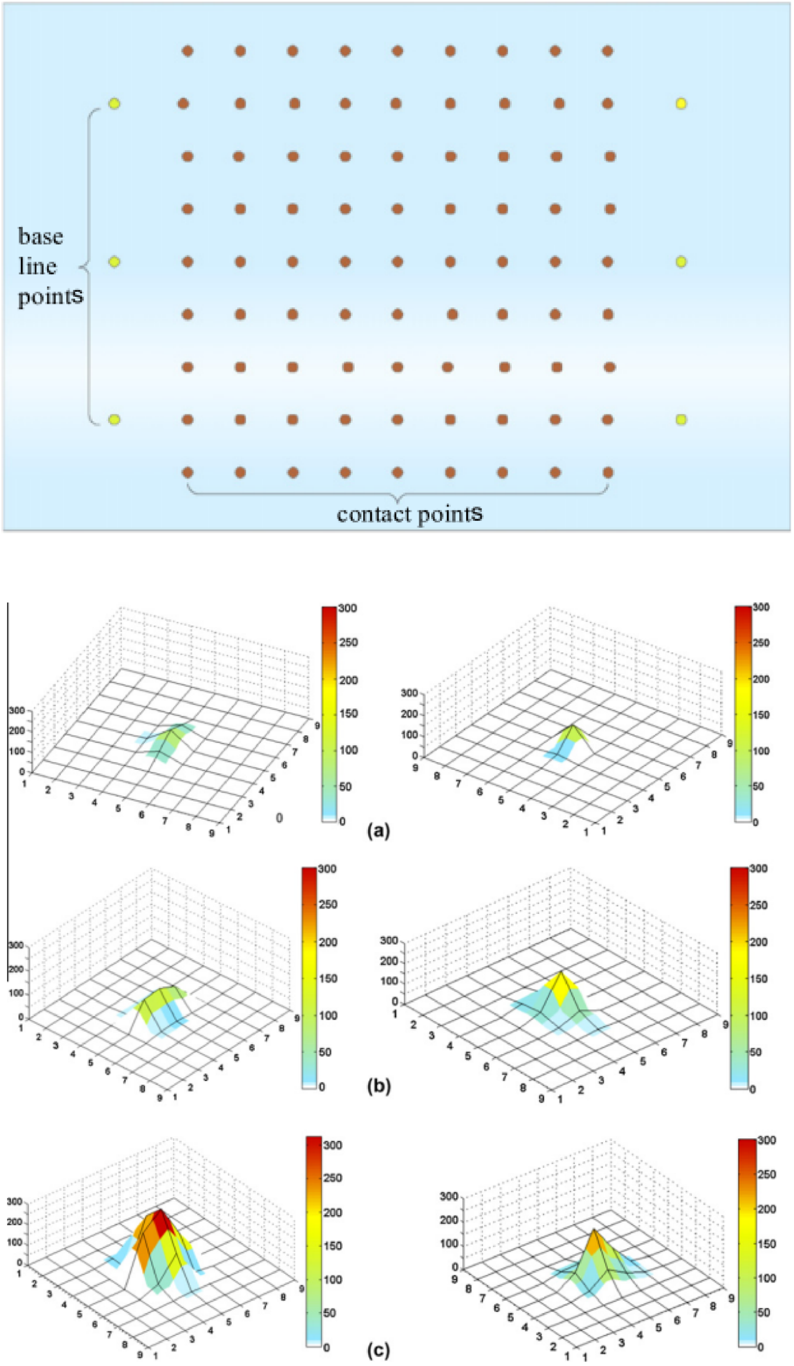

Figure 1.4: Schematic of through-thickness measurement points by Zhang et al. [3] and detection of imacts at (from top to bottom) 50, 100, and 150% of 6.7 J/mm for 2.0 wt. % CB (left) and 2.0 wt. % CB and CC (right).

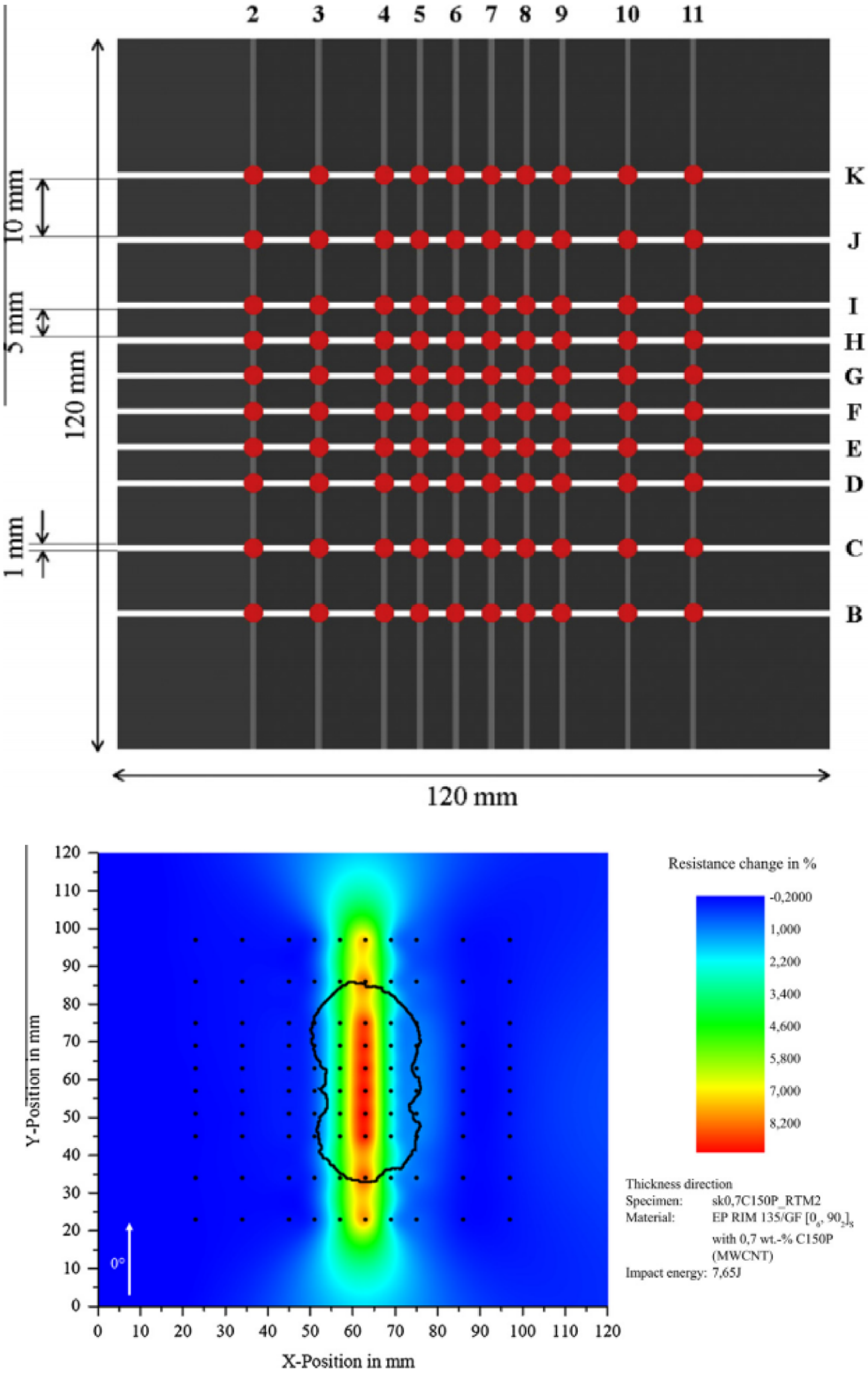

Figure 1.5: Schematic of measurement points by Viets et al. [4] and detection of 7.65 J impact. The black outline is the delamination outline as imaged by ultrasonic C-scan.

through-holes (1/16 in - 6/16 in), low energy (1 - 3 J) impact, and high energy (78 J) impact damage. All of these damages were successfully imaged by plotting the percent change in electric potential between grid points. A schematic of the electrode placement used in this research and the resulting damage detection is shown in Figure 1.6.

1.4 Sensing Layer/Tomographic Methods

EIT is a more sophisticated method of locating changes in conductivity due to damage by reconstructing an internal conductivity distribution based on boundary measurements. Considerable work has been done on nanocomposite thin films or sensing layers wherein the sensing film or layer is applied to the structure to be monitored and EIT is employed to detect exposure to stimuli such as pH, impact, and strain. Consequently, EIT has been shown to have considerable potential for nanocomposite SHM. However, these publications employ EIT routines that use at least 32 electrodes. This is still more than is practical for many SHM applications. A key difference between EIT and resistance change methods is that as a tomographic approach, there is potential to bolster EIT through multi-physics coupling or physics-based insight of the domain being imaged. Resistance change methods, conversely, can never provide any more information than what the resistance is between two points making them fundamentally limited from an image generation perspective.

Hou, Loh, and Lynch [6] first used EIT to image the conductivity distribution of CNT thin films. Using polyelectrolyte constituents polyaniline (PANI) emeraldine base, polyvinyl alcohol (PVA), and polysodium styrene-4-sulfonate (PSS), homogeneous nanostructured thin films were fabricated via a layer-by-layer self-assembly method with single wall carbon nanotube (SWCNT) fillers. $[\text{SWCNT-PSS/PANI}]_{50}$, $[\text{SWCNT-PSS/PANI}]_{100}$, and $[\text{SWCNT-PSS/PVA}]_{50}$ thin films were imaged by EIT to detect mechanical etching, regions of different conductivity, and exposure to pH buffer solutions. Straight, diagonal, and L-shapes were mechanically etched into four separate 25 mm × 25 mm $[\text{SWCNT-PSS/PVA}]_{50}$ specimens. A 32-electrode EIT system was able to accurately locate the etchings while reproducing their geometry. Next, the ability of EIT to detect variations in conductivity was tested. A 18 mm × 18 mm window was mechanically etched from the center of a $[\text{SWCNT-PSS/PVA}]_{50}$ film exposing the substrate. Next, the layer-by-layer process fabricated another $[\text{SWCNT-PSS/PVA}]_{25}$ film over the 50-layer and exposed substrate. A 9 mm × 18 mm window was again mechanically etched from the area that was originally etched, and another 25-bilayer film was deposited resulting in regions of the substrate having 25, 50, or 100-bilayers. Since previous research had established that films with different numbers of layers have different conductivities, a 32-electrode EIT system was used to image

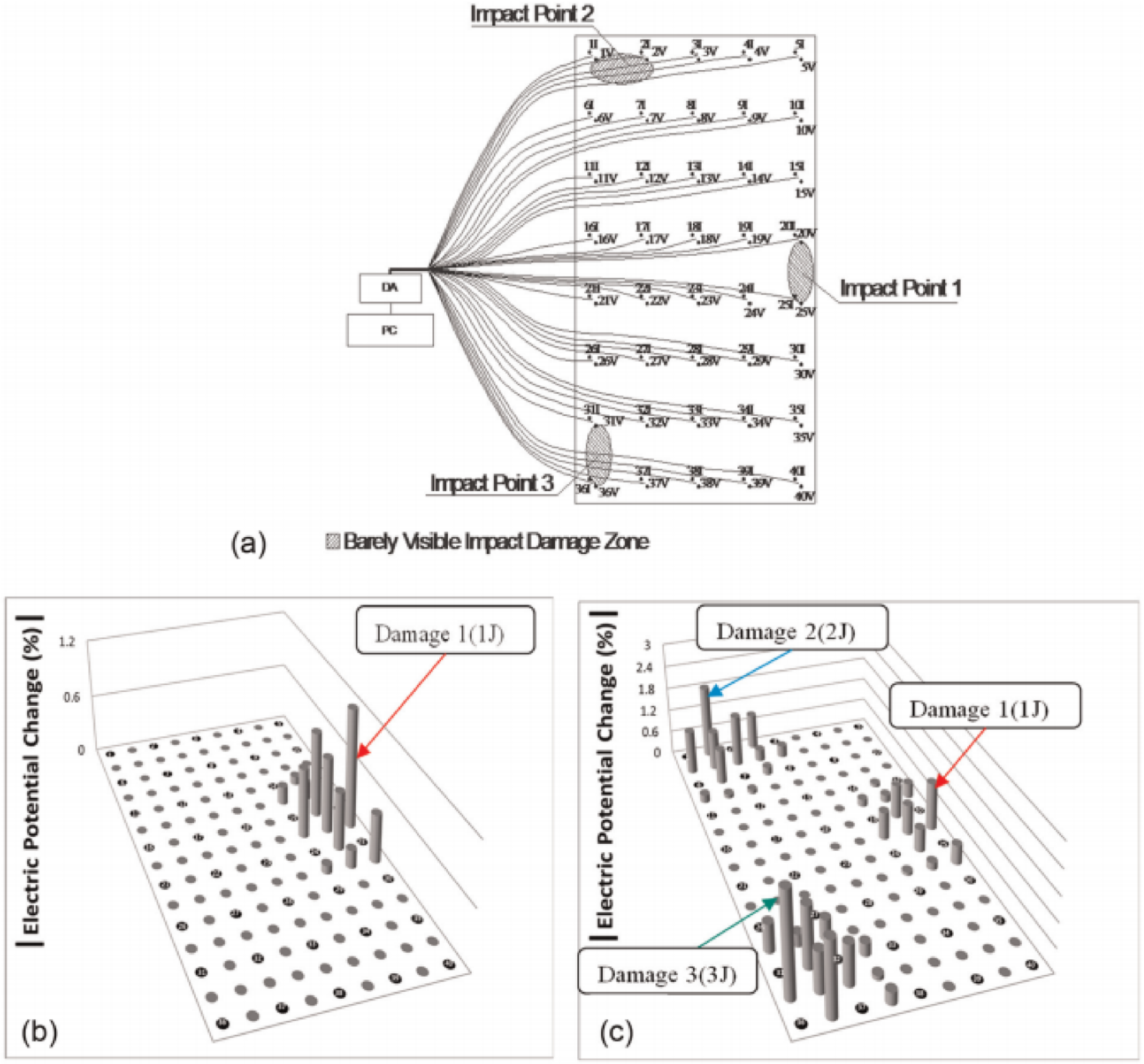

Figure 1.6: Schematic of electrode placement by Naghashpour and Van Hoa [5] and detection of 1, 2, and 3 J impacts.

the film system. EIT was able to accurately image the geometries of the conductivities while discerning conductivity. In order to test sensitivity to pH, five plastic wells were mounted to two 25 mm × 60 mm [SWCNT-PSS/PANI]$_{100}$ films and filled with pH buffer solutions. The first [SWCNT-PSS/PANI]$_{100}$ film had wells filled with pH buffer solutions of 7, 7.5, 8, 8.5, and 9. The second [SWCNT-PSS/PANI]$_{100}$ film had wells filled with pH buffer solutions of 7, 6.5, 6, 5.5, and 5. Because such films have been shown to drastically increase in film resistance with increasing pH buffer solutions, different regions of conductivity are expected. A 48-electrode EIT system was able to locate pH exposure and discern different levels of pH buffer solution. Lastly, the ability of EIT to reproduce absolute conductivities was investigated. To that end, a pristine 25 mm × 25 mm [SWCNT-PSS/PVA]$_{50}$ film was fabricated on a silicon substrate and imaged via EIT using 32 electrodes. The film was then cut into sixteen equally sized squares, and the resistance of each square was measured from which the conductivity of each square could be calculated. These conductivity values were compared to the average value calculate by EIT in the same region. The two methods of determining conductivity agreed within 2.1% indicating that EIT is a viable method to determine absolute conductivity.

Loh, Hou, Lynch, and Kotov [37] fabricated [SWCNT-PSS/PVA]$_n$ sensing skins on glass or aluminum 6061-TS substrates by the layer-by-layer process. EIT was then used to image changes in film conductivity due to mechanical etching, impacts, and strain. Three holes measuring 1 mm × 1 mm, 2.5 mm × 2.5 mm, and 8 mm × 6 mm were etched into a 25 mm × 25 mm [SWCNT-PSS/PVA]$_{50}$ film on a glass substrate. An EIT system with 32 electrodes was able to accurately identify the size and geometry of the etchings. [SWCNT-PSS/PVA]$_{50}$ films on glass substrates were affixed onto polyvinyl chloride Type I tensile coupons by epoxy. The coupon was then mounted in an MTS-810 load frame that performed tensile-compressive cyclic loading of ± 2000 $\mu\varepsilon$ or ± 5000 $\mu\varepsilon$ at 50 $\mu\varepsilon$/s. The films were imaged via EIT with 32 electrodes at 1000 $\mu\varepsilon$ increments. EIT produced nearly uniform conductivity images that scaled linearly with the applied strain. Slight non-uniformities were observed along the edges of each image, and these were believed to be the result of localized lack of strain transfer where the film's substrate was poorly bonded to the test coupons, misalignment of the testing coupon, or numerical artifacts of EIT. Lastly, [SWCNT-PSS/PVA]50 films were deposited onto both sides of 110 mm × 110 mm primer-coated aluminum 6061-T6 alloy plates. A pendulum striker was used to impact the coated plates. Two plates were prepared and each received four impacts of varying energy. The first plate was impacted and imaged shortly after fabrication. The second plate was first impacted twice and imaged. Then it was stored in ambient conditions for approximately 14 days and impacted twice more in order to assess potential of CNT sensing films to detect

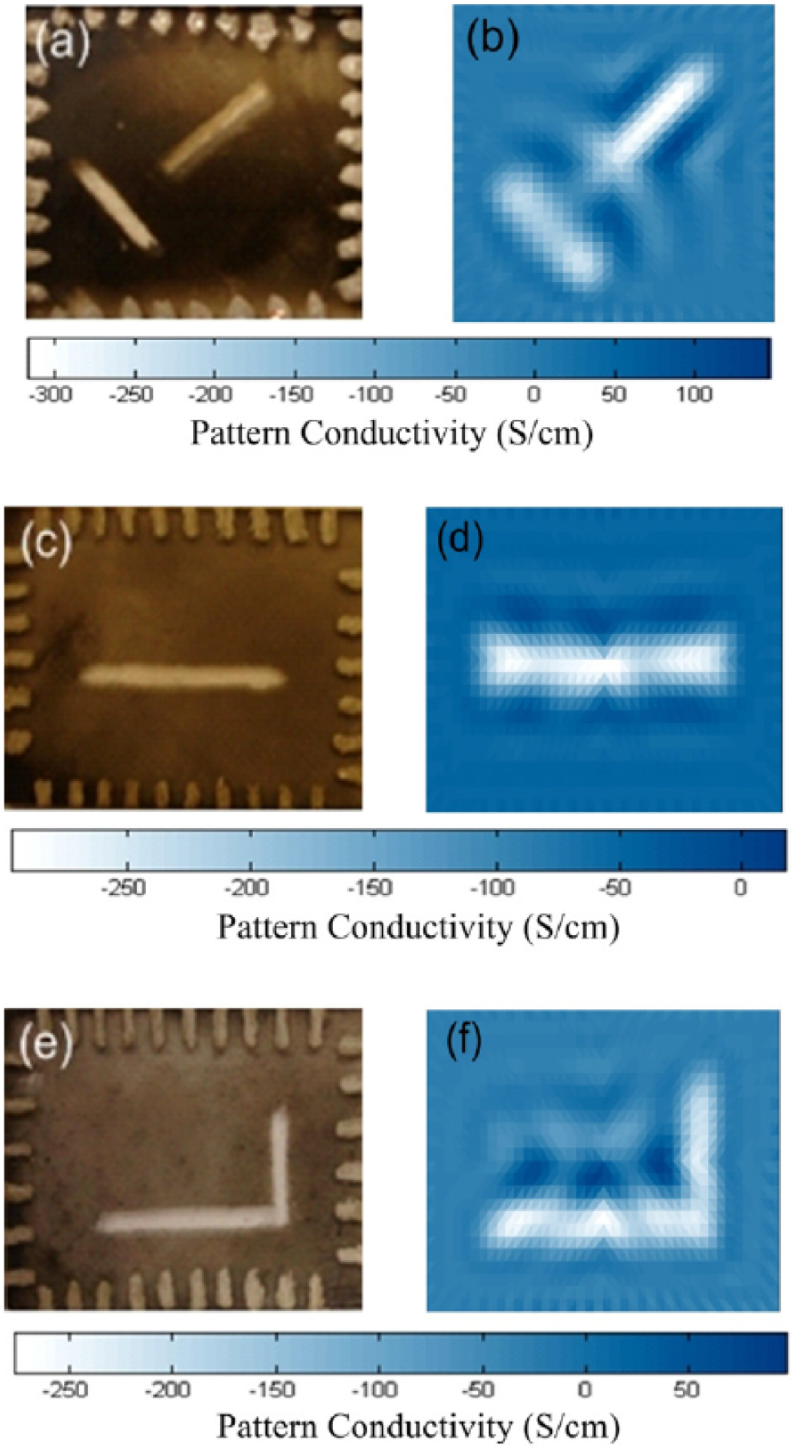

Figure 1.7: Example of EIT electrode requirements and image quality [6]. The conductivity loss is due to the CNF thin film being etched away.

damage throughout a structure's lifetime. Damage as small as 0.09 J was detectable in the first plate, and damage as small as 0.19 was detectable in the second plate. Storing the plate for 14 days seemed to have no effect on the results. This study demonstrates that strain and mechanical damage to nanocomposites can be capture via EIT.

Loyola et al. [60] combined MWCNT polyvinylidene fluoride (PVDF) film sensing layers with GFRPs by spray deposition. The sensing layer film consisted of two parts – MWCNT PSS/N-methyl-2-pyrrolidone solution and a latex of 150 nm diameter spherical particles of Kynar PVDF suspended in an Aquatec surfactant solution. The film formulation was spray deposited on 381 mm × 381 mm unidirectional E-LR 0908 fiber laminae that was masked to contain six equally spaced sensing areas measuring 78 mm × 78 mm. Laminates were constructed following a $[0/45/90/\text{-}45]_{2s}$ stacking sequence. The sensing films were placed only on the top and bottom plies in order to facilitate electrode access. Because of the inherent anisotropy of laminates, the sensing films were also electrically anisotropic with a preferred conductivity in the fiber direction. Consequently, an anisotropic EIT reconstruction algorithm was employed. A sensitivity study was conducted by drilling progressively larger through-holes at the center of the laminates. It was concluded that 3.18 mm diameter hole was the lower limit of EIT on this material. However, the image artifact due to the 3.18 mm hole was comparable to the image noise. Sensitivity to damage location was also characterized by dividing the specimen into a 3 × 3 grid of equally sized squares. A 6.35 mm diameter hole was drilled at the center of each partition and imaged by EIT with 32 electrodes. It was found that EIT is least sensitive to damage in the center and most sensitive to damage near electrodes, particularly at corners. Following ASTM D-7136, specimens were impacted at 20, 60, 100, and 140 J using an instrumented Instron Dynatup 9250G drop-weight tester. EIT was able to detect impacts that did not cause immediately visible damage.

CHAPTER 2

Problem Statement, Research Goal, and Thesis Organization

The literature surveyed in Chapter 1 establishes that conductivity-based methods have incredible potential for transformative SHM of fiber-reinforced composites with integrated nanocomposites. Furthermore, the literature cited in the tomographic methods section establishes that EIT can accurately be employed on nanocomposites. State of the art conductivity-based SHM techniques utilize either nanocomposite matrix/resistance change methods or sensing layer/EIT methods. Both of these approaches have advantages; however, they both also have important limitations.

By using nanocomposites as matrices, nanocomposite matrix/resistance change methods ensure sensitivity to matrix damage. This is important because fiber-reinforced composite failure is often initiated through matrix damage. A robust conductivity-based SHM technique must, therefore, retain sensitivity to matrix damage. Resistance change methods, however, also require large, unwieldy electrode arrays to crudely locate damage as exemplified in Figures 1.3, 1.4, 1.5, and 1.6. This dependence on large electrode arrays makes resistance change methods unpalatable if not impractical to implement on in-service structures.

Sensing layer/EIT methods are quite powerful in their adaptability because they can be applied to a myriad of structures and are not necessarily limited to fiber-reinforced composites. EIT, furthermore, has considerable potential for conductivity-based SHM because it can provide better spatial resolution than resistance change methods with fewer electrodes as exemplified in Figure 1.7. However, with regard to fiber-reinforced composite SHM, sensing layer approaches add weight to often weight-conscious composite structures such as airplanes, are not sensitive to damage sufficiently removed from the sensing layer such as internal damage initiated by cyclic loading, and are vulnerable to superficial damage induced by hail, sleet, or dust which poses no real threat to the structure. EIT also tends to be insensitive to abrupt, highly localized conductivity changes as is expected in matrix cracking and delamination initiation, suffers from poor resolution, and still requires more electrodes than is desirable from an implementation perspective.

An ideal fiber-reinforced composite SHM system should have all of the advantages of the state of the art methods and none of the disadvantages. That is, *an ideal fiber-reinforced composite SHM system should be sensitive to matrix damage, require a minimum number of sensors, and be able to spatially locate where damage has occurred.* In this light, a concise problem statement, novel idea to advance the state of the art, and research goal are formed as follows.

Problem statement: existing SHM methods are insufficient or not ideally suited for fiber-reinforced composites. Nanocomposite conductivity-based health monitoring via EIT has considerable potential but also important limitations.

Novel idea: advance the state of the art in fiber-reinforced composite SHM by combining the superior imaging capabilities of EIT with self-sensing nanocomposite matrices. Then leverage the unique properties of nanocomposites to overcome the limitations of EIT.

Research goal: develop EIT into a robust conductivity-based SHM technique for fibrous composites with nanocomposite matrices.

In order to achieve this goal the mathematical formulation of EIT will first be presented. The unique properties of nanocomposite conductivity are then investigated. Having developed an understanding of nanocomposite conductive properties, damage and strain identification via EIT will next be experimentally investigated and demonstrated. And, finally, the insights developed in the two preceding chapters will be combined to markedly enhance EIT for SHM. Following the technical contributions of this thesis, its scholarly contributions and broader impacts are summarized, and, lastly, recommendations for future work are made.

CHAPTER 3

Electrical Impedance Tomography Theory and Formulation

3.1 Introduction and History

EIT is a method of non-invasively imaging an internal conductivity distribution by inversely solving Laplace's equation given boundary voltage data [61]. Because the conductivity of a nanocomposite is inherently linked to its mechanical state, EIT can be used to locate strain or damage. EIT is attractive for SHM because it is minimally invasive, can be employed in nearly real time, and is low cost. Based on Calderón's inverse problem [62], EIT was originally developed for subterraneous prospecting [63] [64] and specialized medical imaging applications [65] [66]. Impedance imaging began with Henderson and Webster [67] in 1978, but the first tomographic impedance images were produced by Barber, Brown, and Freeston [68].

Procedurally, the domain to be imaged by EIT is lined with electrodes. Current is injected and grounded between the first electrode pair while voltages are measured between the remaining electrode pairs not involved in the current injection as depicted in Figure 3.1. The current injection is then moved to the next electrode pair, and the voltage is again measured between electrode pairs not involved in the current injection. Measurements are not taken from electrodes involved in the current injection because even slight errors in the estimated contact impedance can result in large electrode voltage prediction errors. This process repeats until every electrode pair has received a current injection. The same injection and measurement process is repeated analytically – this is known as the forward problem or the forward operator. The forward operator returns a vector of predicted boundary voltages for a prescribed conductivity distribution. Consequently, the goal of EIT is to find a conductivity distribution that minimizes the error between the forward operator and the experimentally measured voltages.

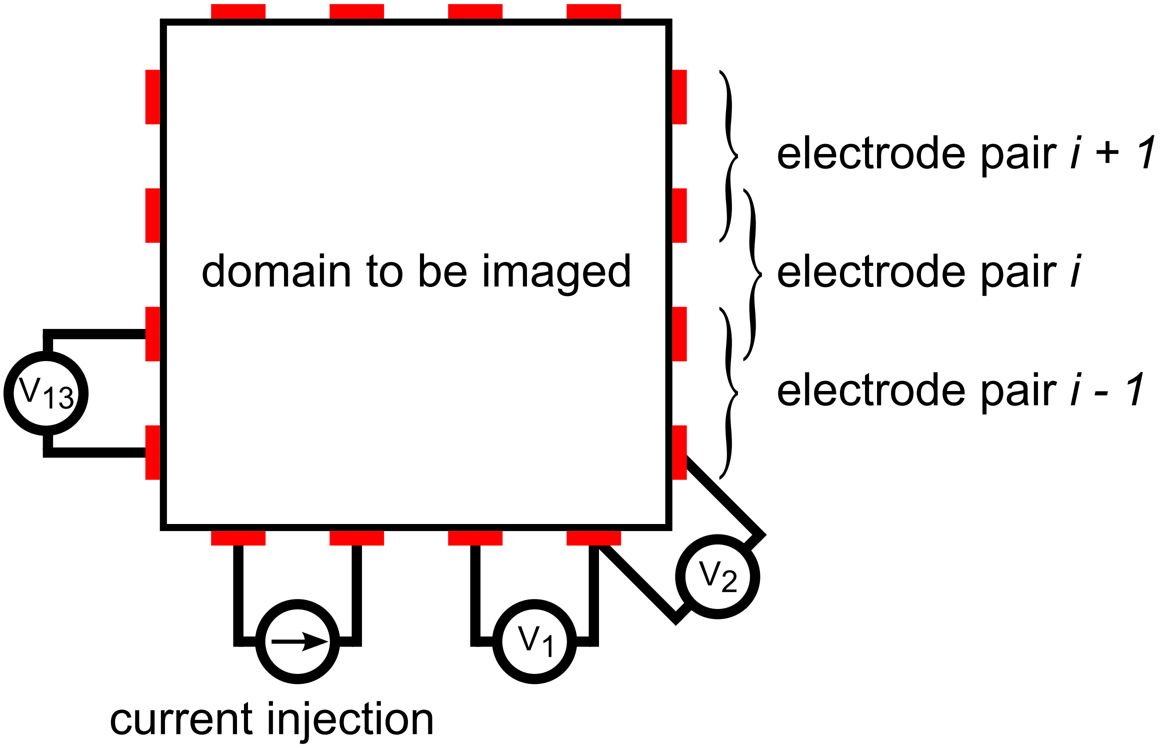

Figure 3.1: EIT injection schematic. Current is injected between the first electrode pair while the resulting voltage is measured between the remaining electrode pairs that are not involved in the injection process. All electrode pairs receive a current injection.

3.2 Forward Problem

Laplace's equation governs the relationship between currents and voltages for steady state diffusion as shown in equation 3.1.

$$\frac{\partial}{\partial x_i}\sigma_{ij}\frac{\partial u}{\partial x_j} = 0 \tag{3.1}$$

Summation notation is used here, and repeated indices imply summation over the dimension of the problem. Summation is not implied for indices referring to electrodes unless the summation operator is explicitly stated. The general anisotropic form of the forward problem will be derived here, but this of course simplifies to the isotropic case for $\sigma_{ij} = \sigma\delta_{ij}$ where δ_{ij} is the Kronecker delta. Regarding Equation 3.1, it is assumed in EIT that direct currents or sufficiently low frequency alternating currents are used such that magnetic fields can be neglected. The complete electrode model (CEM) boundary conditions are employed to simulate contact impedance between the assumed perfectly conducting electrodes and the domain as shown in equation 3.2. Equation 3.3 enforces the conservation of charge by requiring that the current through the electrodes sums to zero.

$$\sigma_{ij}\frac{\partial u}{\partial x_i}n_j = \frac{1}{z_l}\left(V_l - u\right) \tag{3.2}$$

$$\sum_{l=1}^{L}\int_{E_l}\sigma_{ij}\frac{\partial u}{\partial x_i}n_j\,\mathrm{d}S_l = 0 \tag{3.3}$$

In the preceding, u is the domain potential, n_i is the outward pointing normal, z_l is the contact impedance between the *l*th electrode and the domain, and V_l is the voltage on the *l*th electrode. These equations are most conveniently solved through finite element discretization in the following manner.

$$\begin{bmatrix}\mathbf{A}_M + \mathbf{A}_Z & \mathbf{A}_W \\ \mathbf{A}_W^T & \mathbf{A}_D\end{bmatrix}\begin{bmatrix}\mathbf{U} \\ \mathbf{V}\end{bmatrix} = \begin{bmatrix}\mathbf{0} \\ \mathbf{I}\end{bmatrix} \tag{3.4}$$

$$A^e_{M\,ij} = \int_{\Omega_e}\frac{\partial w_i}{\partial x_k}\sigma_{kl}\frac{\partial w_j}{\partial x_l}\,\mathrm{d}\Omega_e \tag{3.5}$$

$$A_{Z\,ij} = \sum_{l=1}^{L}\int_{E_l}\frac{1}{z_l}w_i w_j\,\mathrm{d}S_l \tag{3.6}$$

$$A_{W\,li} = -\int_{E_l}\frac{1}{z_l}\,w_i\,\mathrm{d}S_l \tag{3.7}$$

$$\mathbf{A}_D = \mathrm{diag}\left(\frac{E_l}{z_l}\right) \tag{3.8}$$

Explicit details of the forward problem formulation by the finite element method can be found in Appendix A. Equation 3.4 is the discretization of the CEM forward problem. $\mathbf{U}$ is a vector of domain potentials, $\mathbf{V}$ is a vector of electrode voltages, and $\mathbf{I}$ is a vector of current injections. The *i*th entry of the *j*th column of the local diffusion stiffness matrix for the *e*th element is formed as shown in equation 3.5 where w_i is the *i*th interpolation or weighting function. Linear interpolation functions are herein employed. Local diffusion stiffness matrices are assembled into the global diffusion stiffness matrix, $\mathbf{A}_M$. Equation 3.6, equation 3.7, and equation 3.8 account for additional degrees of freedom introduced by the electrodes and contact impedance between the electrodes and the domain. E_l is the electrode length in two dimensions or the electrode area in three dimensions, and summations run over the total number of electrodes, L. Equation 3.4 is only solved up to an arbitrary constant or electrical ground point, but this can be remedied by enforcing that grounded electrode of the injection pair is zero. However, because EIT makes use of the difference between electrodes, determining a ground point inconsequential.

3.3 Inverse Problem

Image recovery through EIT has received very thorough mathematical treatment. Numerous reconstruction algorithms have emerged the most popular of which are Gauss-Newton minimization, maximum a posteriori (MAP) estimates, and the primal-dual interior point method (PDIPM). Gauss-Newton minimization is used in this research because of its superior convergence and ability to satisfactorily image both discrete conductivity losses due to damage and smoothly varying conductivity distributions due to strain. It is therefore more diligently treated than MAP and PDIPM algorithms in the following sections. The general process of recovering the conductivity distribution is known as the EIT inverse problem.

3.3.1 Gauss-Newton Method

The Gauss-Newton method iteratively updates a conductivity estimate to minimize the difference between experimental measurements and an analytical model in the least-squares sense according to equation 3.9 [61].

$$\boldsymbol{\sigma}^* = \arg\min_{\boldsymbol{\sigma}} \left(\|\mathbf{V}_m - \mathbf{F}(\boldsymbol{\sigma})\|^2\right) \tag{3.9}$$

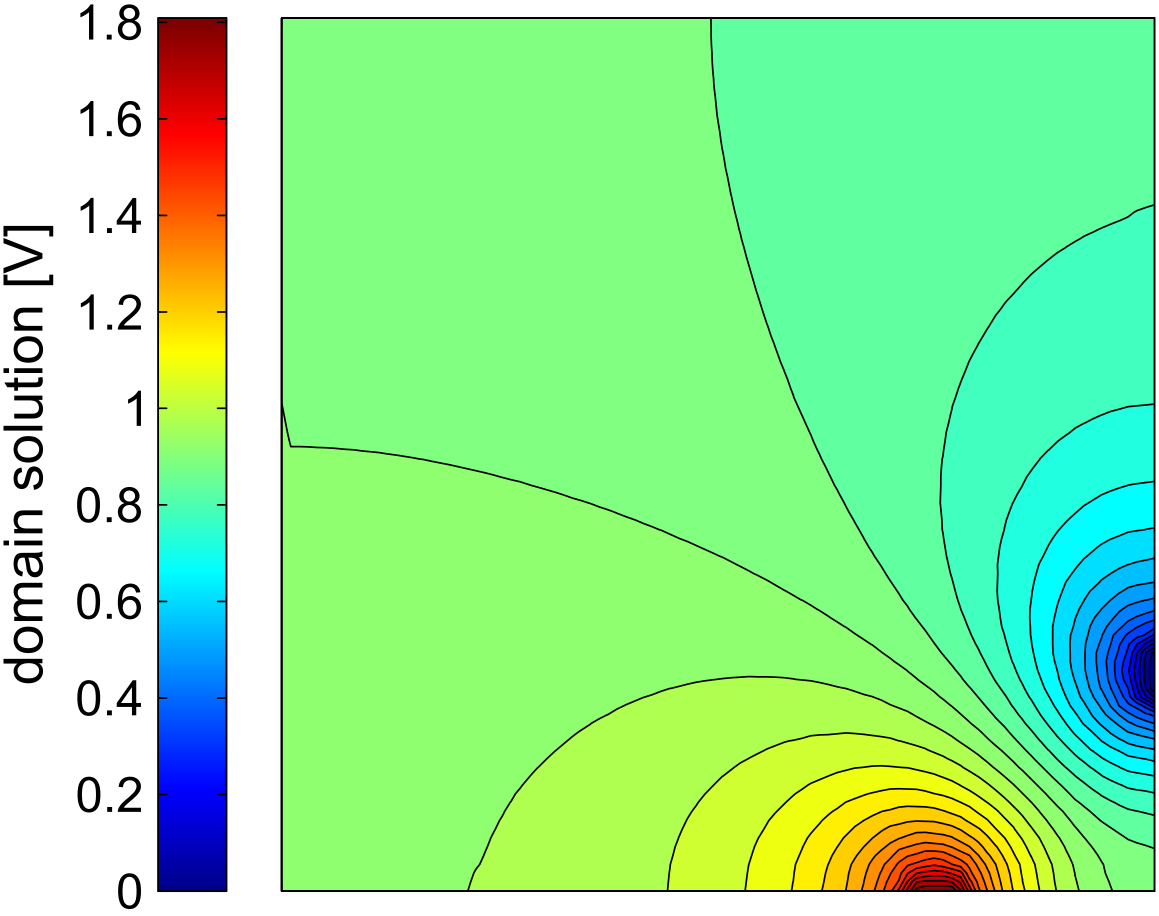

Figure 3.2: Representative solution to the forward problem with unit conductivity and current injection. Current is injected and grounded at the bottom right corner. Electrodes and electrode solutions are not shown.

$\mathbf{V}_m$ is the vector of experimentally measured voltages, $\mathbf{F}(\boldsymbol{\sigma})$ is a vector of analytically predicted boundary voltages supplied by the forward operator, $\boldsymbol{\sigma}$ is the conductivity distribution provided to the forward operator, and $\boldsymbol{\sigma}^*$ is the conductivity distribution that satisfies the minimization. Note that anisotropy has been abandoned here because recovering anisotropic conductivity typically requires special considerations. This will be treated later in Chapter 6. Also note that the conductivity distribution is now bold faced to indicate that it has been discretized by the preceding finite element formulation of the forward problem. To proceed, $\mathbf{F}(\boldsymbol{\sigma})$ is approximated by a Taylor series expansion centered about an initial conductivity estimate, $\boldsymbol{\sigma}_0$. Only the linear terms of the expansion are retained resulting in equation 3.10. This approximation of $\mathbf{F}(\boldsymbol{\sigma})$ is then substituted into equation 3.9 resulting in equation 3.11.

$$\mathbf{F}(\boldsymbol{\sigma}) \approx \mathbf{F}(\boldsymbol{\sigma_0}) + \frac{\partial \mathbf{F}(\boldsymbol{\sigma}_0)}{\partial \boldsymbol{\sigma}}(\boldsymbol{\sigma} - \boldsymbol{\sigma}_0) \tag{3.10}$$

$$\boldsymbol{\sigma}^* = \arg\min_{\boldsymbol{\sigma}} \left(\left\| \mathbf{V}_m - \mathbf{F}(\boldsymbol{\sigma_0}) - \frac{\partial \mathbf{F}(\boldsymbol{\sigma}_0)}{\partial \boldsymbol{\sigma}}(\boldsymbol{\sigma} - \boldsymbol{\sigma}_0) \right\|^2 \right) \tag{3.11}$$

By substituting $\mathbf{J} = \partial \mathbf{F}(\boldsymbol{\sigma}_0)/\partial \boldsymbol{\sigma}$, $\Delta\boldsymbol{\sigma} = \boldsymbol{\sigma} - \boldsymbol{\sigma}_0$, and $\mathbf{V}_e = \mathbf{V}_m - \mathbf{F}(\boldsymbol{\sigma}_0)$ into equation 3.11, equation 3.12 can be formed.

$$\boldsymbol{\sigma}^* = \arg\min_{\boldsymbol{\sigma}} \left(\|\mathbf{V}_e - \mathbf{J}\Delta\boldsymbol{\sigma}\|^2 \right) \tag{3.12}$$

Because $\mathbf{J}$ is severely rank-deficient, $\Delta\boldsymbol{\sigma}$ needs to be recovered by means of Tikhonov regularization the new minimization formulation and explicit solution to which are shown in equation 3.13 and equation 3.14 respectively.

$$\boldsymbol{\sigma}^* = \arg\min_{\boldsymbol{\sigma}} \left(\|\mathbf{V}_e - \mathbf{J}\Delta\boldsymbol{\sigma}\|^2 + \alpha \|\mathbf{L}\boldsymbol{\sigma}\|^2 \right) \tag{3.13}$$

$$\Delta\boldsymbol{\sigma} = \left(\mathbf{J}^T\mathbf{J} + \alpha^2 \mathbf{L}^T\mathbf{L} \right)^{-1} \mathbf{J}^T\mathbf{V}_e \tag{3.14}$$

The conductivity estimate is then updated as shown in equation 3.15 until the error is sufficiently minimized.

$$\boldsymbol{\sigma}^*_{n+1} = \boldsymbol{\sigma}^*_n + \Delta\boldsymbol{\sigma} \tag{3.15}$$

$\mathbf{L}$ is the regularization term, and its contribution is controlled by α. Herein, the unweighted discrete Laplace operator is employed for regularization, but the identity matrix is another common choice.

$$\mathbf{L} = L_{ij} = \begin{cases} \text{degree}(\Omega_i) & \text{if } i = j \\ -1 & \text{if } i \neq j \text{ and } \Omega_i \text{ is adjacent to } \Omega_j \\ 0 & \text{otherwise} \end{cases} \tag{3.16}$$

$\mathbf{L} = L_{ij}$ is a square matrix sized by the number of elements in the finite element mesh of the forward problem. The *i*th value of the diagonal is equal to the number of elements that share an edge in two dimensions or a side in three dimensions with the *i*th element. If the *i*th and *j*th elements share an edge in two dimensions or a surface in three dimensions, $L_{ij} = L_{ji} = -1$. All other entries are zero. Although subscript i and j previously ran over the dimension of the domain, they are merely employed as generic indices to elucidate the formation of **L** here.

Lastly, **J**, also known as the sensitivity matrix, is formed by enforcing the conservation of power through the electrodes and in the domain thereby relating electrode voltage perturbations to conductivity perturbations as shown in equation 3.17 [61].

$$J_{MN\,e} = -\int_{\Omega_e} \frac{\partial u^M}{\partial x_i} \frac{\partial \bar{u}^N}{\partial x_i} \, \mathrm{d}\Omega_e \tag{3.17}$$

Computationally, MN is a single index of **J** and refers to the integral of the contraction of the gradient of the voltage on the *e*th element due to current supplied by the *M*th electrode injection pair and the gradient of the voltage on the *e*th element due to the *N*th adjoint field. The adjoint field is the domain solution due to a unit current injection being supplied to the *N*th electrode measurement pair. This integral is evaluated over the *e*th element. This can also be thought of as the sensitivity of the *N*th electrode measurement pair due to a slight conductivity perturbation of the *e*th finite element when the current is injected in the *M*th electrode pair. Detailed sensitivity matrix calculations for linear triangular and tetrahedral elements can be found in Appendix B.

3.3.1.1 Convergence

Convergence is an important consideration for EIT. Given an appropriate initial estimate, Gauss-Newton minimization techniques enjoy quadratic convergence. However, in light of the underdetermined nature of the inverse problem, this is not seen in EIT. Nonetheless, it has been demonstrated that iterative Gauss-Newton methods converge to a smaller error in fewer iterations than other reconstruction methods [69] [70]. The convergence of Gauss-Newton methods in EIT has been proven for appropriately selected regularizations [71].

The regularization parameter α^2 is selected such that smooth convergence is obtained

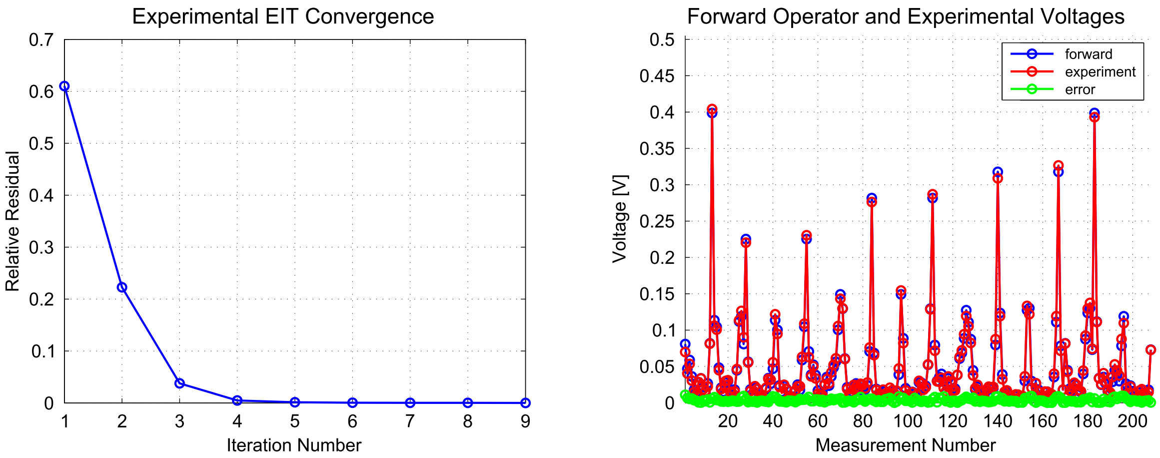

Figure 3.3: Left: representative convergence plot of experimental EIT. Right: voltage difference measurements by the forward operator after convergence and the experimentally measured voltages.

in the experimental EIT results throughout this document. Figure 3.3 shows a representative example of convergence obtained experimentally by plotting relative residual against iteration number. Also shown in Figure 3.3 is a representative comparison of the voltages predicted by the forward operator after convergence and the experimentally measured boundary voltages.

3.3.1.2 Baseline Subtraction

The previously described Gauss-Newton EIT formulation reconstructs the absolute conductivity distribution. This means the method tries to incrementally update the initial conductivity estimate to match the true conductivity as closely as possible. However, absolute conductivity reconstructions are typically not reported because even slight discrepancies in electrode placement between the experiment and the forward operator can result in large conductivity prediction errors. Consequently, the difference between images is typically reported. This means that the domain is imaged at two distinct instances in time, and the difference between these two reconstructions is presented. Because the errors due to electrode placement discrepancies are common to both images, they subtract out. For example, the domain could be imaged before damage and after damage. The undamaged case is often referred to as the baseline state, and damage becomes evident by subtracting the baseline from the damaged reconstruction. However, the baseline need not be the undamaged case.

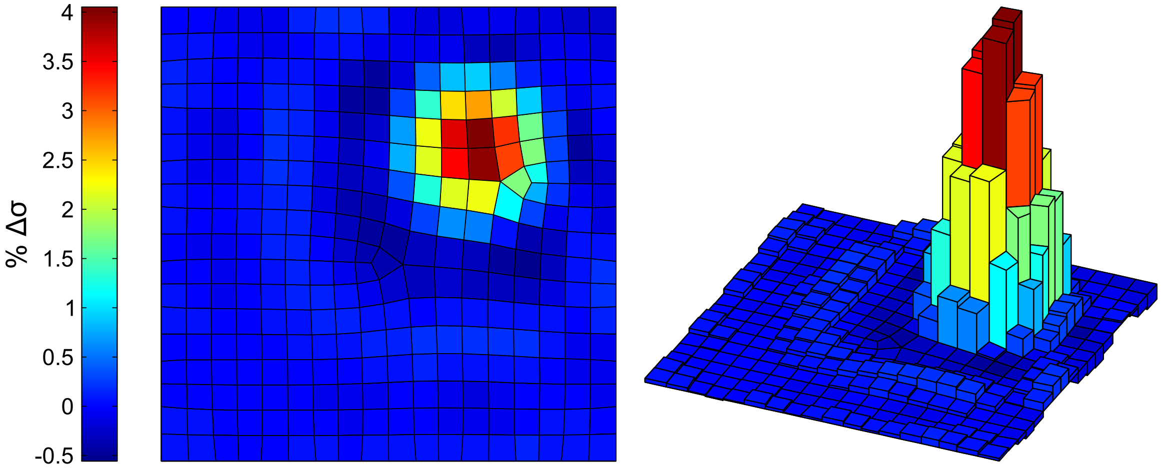

Figure 3.4: Representative EIT solution using the Gauss-Newton method on a quadrilateral mesh.

3.3.2 Maximum a Posteriori Method

MAP estimates use *a priori* knowledge of measurement noise variance and conductivity distribution covariance to linearize the difference between voltage measurements at two times with a single step. This approach has the advantage of being exceptionally fast because the sensitivity matrix can be calculated offline, and MAP methods have excellent noise rejection. However, they can fail if the difference between states cannot be well represented by a single-step linearization. Based on [72], voltage measurements are assumed to be expressible as shown in equation 3.18.

$$v_i = a_i u_i + b_i \tag{3.18}$$

v_i is the *i*th component of the vector of the measured voltages and u_i is the *i*th component of the vector of the true voltages. Random measurement noise is represented by a_i and b_i. MAP algorithms try to find the difference in conductivity between measurements at times t^1 and t^2. To that end, define z_i as

$$z_i = \frac{v_i^1 - v_i^2}{\frac{1}{2}\left(v_i^1 + v_i^2\right)}. \tag{3.19}$$

Expressing z_i in terms of u_i^1 and u_i^2 results in

$$z_i = \frac{u_i^1 - u_i^2}{\frac{1}{2}\left(u_i^1 + u_i^2\right)} \frac{1}{1 + \dfrac{2b_i}{1 + a_i\left(u_i^1 + u_i^2\right)}}. \tag{3.20}$$

Utilizing the voltage measurements in this form reduces the effect of additive noise by a factor of $1/2a_i\left(u_i^1 + u_i^2\right)$. The conductivity difference between the times is recovered as

$$\Delta\boldsymbol{\sigma} = \left(\mathbf{J}^T\mathbf{R}_n^{-1}\mathbf{J} + \mathbf{R}_x^{-1}\right)^{-1}\left(\mathbf{J}^T\mathbf{R}_n^{-1}\mathbf{z} + \mathbf{R}_x^{-1}\mathbf{x}_\infty\right). \tag{3.21}$$

$\mathbf{R}_n$ is a diagonal matrix of the noise power in each component of the signal, $\mathbf{R}_x^{-1}$ is a regularization parameter, and $\mathbf{x}_\infty$ is a conductivity difference estimate.

3.3.3 Total Variation Regularization and the Primal-Dual Interior Point Method

Total variation regularization adds a penalty term to the minimization problem shown in equation 3.9 such that discontinuous conductivity distributions are not penalized and can be recovered. Gauss-Newton minimization and MAP algorithms, conversely, favor smoothly varying conductivity distributions resulting in blurry or smeared images. This is a result of the quadratic nature of the minimization problem. Recovering discontinuous conductivity distributions is a desirable property in applications such as medical imaging because organs have clearly defined boundaries with distinct conductivities [73] [74] [75]. Damage to a nanocomposite will also result in a discontinuity at the damage location; however, total variation regularization methods are not as adept at recovering smoothly varying conductivities as produced by strain fields. The penalty term added to the minimization measures the total amplitude of the oscillations of a function and is called the total variation functional as shown in equation 3.22 [61].

$$\mathrm{TV}(\sigma) = \int_\Omega |\boldsymbol{\nabla}\sigma| \, \mathrm{d}\Omega \tag{3.22}$$

Adding equation 3.22 as a penalty term in equation 3.9 results in the following minimization problem.

$$\sigma^* = \arg\min_\sigma \left(\|\mathbf{V}_m - \mathbf{F}(\sigma)\|^2 + \mathrm{TV}(\sigma)\right) \tag{3.23}$$

Conductivity is recovered from equation 3.23 by a flavor of primal-dual linear programming. The PDIPM algorithm was developed for inverse problems with linear forward operators [76]. Quite succinctly, primal-dual methods endeavor to minimize some primary problem such as equation 3.23 subject to some dual problem constraints, and primal-dual methods proceed by iteratively improving a dual feasible point until a primal feasible point can be found satisfying the constraints. Much more thoroughly treated in [61] [73], the system of nonlinear equations that defines the PDIPM for EIT are shown below.

$$\|\mathbf{y}_i\| \leq 1 \tag{3.24}$$

$$\mathbf{J}^T\left(\mathbf{F}(\boldsymbol{\sigma}) - \mathbf{V}_m\right) + \alpha\mathbf{T}^T\boldsymbol{\sigma} = \mathbf{0} \tag{3.25}$$

$$\mathbf{T}\boldsymbol{\sigma} - \mathbf{E}\mathbf{y} = \mathbf{0} \tag{3.26}$$

Here, $\mathbf{E} = \mathrm{diag}\left(\sqrt{\|\mathbf{T}_i\boldsymbol{\sigma}\|^2 + \beta}\right)$, β is a centering parameter, and $\mathbf{T}$ is the discrete form of the total variation operator. That is, $\mathbf{T}\boldsymbol{\sigma} = TV(\sigma)$. Initial estimates of $\boldsymbol{\sigma}$ and $\mathbf{y}$ are updated iteratively as shown in equation 3.27 where $\mathbf{K} = \mathrm{diag}\left(1 - {}^{\mathbf{y}_i\mathbf{T}_i\boldsymbol{\sigma}}\!/_{\mathbf{E}_{ii}}\right)$.

$$\begin{bmatrix} \mathbf{J}^T\mathbf{J} & \alpha\mathbf{T}^T \\ \mathbf{K}\mathbf{T} & -\mathbf{E} \end{bmatrix} \begin{bmatrix} \Delta\boldsymbol{\sigma} \\ \Delta\mathbf{y} \end{bmatrix} = - \begin{bmatrix} \mathbf{J}^T\left(\mathbf{F}(\boldsymbol{\sigma}) - \mathbf{V}_m\right) + \alpha\mathbf{T}^T\mathbf{y} \\ \mathbf{T}\boldsymbol{\sigma} - \mathbf{E}\mathbf{y} \end{bmatrix} \tag{3.27}$$

Subscripts in the preceding denote the *i*th entry of a vector, the *i*th row of a matrix, or in the case of a repeated subscript, the *i*th term of the main diagonal of a matrix. Summation is not implied by repeated subscripts.

Despite the potential of total variation regularization and the PDIPM to recover discontinuous conductivities as induced by damage, they are not employed herein because they are not nearly as robust as Gauss-Newton methods. Recovering $\Delta\mathbf{y}$ from equation 3.27 also requires carefully implemented line search algorithms. Such tediousness makes the PDIPM less palatable from a computational point of view for integrated SHM. Hallaji et al. [77] did, however, use total variation regularization for the detection of damage to copper skins on cementitious structures.

CHAPTER 4

Nanocomposite Conductive Properties

4.1 Introduction

Because nanocomposites depend on nanofiller networks for electrical conductivity, they exhibit unique conductive properties. Mechanical and electrical/thermal loading, for example, can result in appreciable if not substantial conductivity changes. Similarly, the directionality of the nanofiller network or lack thereof can markedly influence electrical diffusivity. Understanding these phenomena is therefore not only critical to successfully employing conductivity-based SHM but also to later enhancing EIT.

Nanocomposite piezoresistivity has received considerable attention from a modeling and prediction perspective for the development of high sensitivity strain sensors [7] [38] [50] [78]. These modeling efforts, however, have been exclusively concerned with piezoresistive response to tensile or compressive strain and often limited to microscale analyses whereas, ideally, a robust piezoresistivity model should be more general and amenable to structural-scale analyses. Certainly a structural-scale piezoresistivity model is required if nanocomposites are ever to be implemented at large scales for conductivity-based SHM. A gap therefore exists in state of the art piezoresistivity modeling between what is needed and what currently exists.

Another interesting property of nanocomposite conductivity is electrical anisotropy induced by nanofiller alignment. Advances in nanomanufacturing have enabled microscale alignment in nanocomposites by means of mechanical forces, electric or magnetic fields, shear flow, or electro-spinning [32]. For example, Sharma, Bakis, and Wang studied how carbon nanofibers could be aligned and chained in epoxide [79]. Thostenson and Chou extruded polymer melts through rectangular die prior to cooling to produce highly aligned nanocomposite films [80]. With respect to structural composites, Gungor and Bakis applied strong electric fields through the thickness direction of glass fiber/epoxy composite plates with carbon black filler prior to curing in order to induce networking through the thickness direction. They found this increased the through-thickness conductivity by a factor of 10^4 [81]. Domingues, Logakis, and Skordos applied electric fields to align CNTs in glass fiber reinforced thermosetting composites. They found that alignment increased through-thickness conductivity by an order of magnitude but the in-plane conductivity was unaffected [82]. Studies such as the preceding are of keen interest from a SHM and damage identification perspective because the influence of microscale nanofiller alignment on structural-scale damage identification is relatively unexplored. However, the prospect of microscale alignment also poses important challenges. For example, many conductivity-based SHM techniques depend on in-plane measurements; that is, nanofillers may be aligned through the thickness direction of composite plates, but SHM measurements are not made through the thickness direction. This is certainly the case for tomographic approaches. Percolation probability, critical volume fraction, and conductivity transverse to the alignment direction are therefore pressing considerations. Without percolation, conductivity-based SHM will not be possible because conductivity-based SHM depends on the existence of a well-connected nanofiller network. And with excessive resistivity in the measurement direction, conductivity-based SHM will require the application of prohibitively large voltages thereby effectively nullifying its practicality. In light of the preceding discussion, another important gap in the state of the art is identified: properties transverse to the alignment direction have not yet been dutifully investigated.

The response of nanocomposites to electrical loading is varied. Loh et al. [83] reported a drift in voltage taken while using a CNT thin film strain sensor. In this case, the conductivity of the composite increased, and this was speculated to be due to Joule heating of nanotubes activating electrons to tunnel between filler junctions. Cardoso et al. [84] also found the conductivity of CNF/epoxy to increase with temperature. However, Kumar et al. [85] and Qilin et al. [86] both reported a decrease in conductivity of a CNF nanocomposite under electrical loading due to thermal expansion of the matrix increasing the distance between filler junctions. Because of the disparities in nanocomposite response to electrical loading, it is important to characterize how conductivity evolves for a particular nanocomposite prior to employing it.

This chapter addresses the preceding limitations. First, an analytical piezoresistivity model is developed for arbitrarily strained MWCNT nanocomposites with low filler aggregation. Because of its analytical formulation, this model is amenable to the finite element formulation and therefore enables structural-scale piezoresistive analysis. Next, the influence of nanofiller alignment on transverse conductivity, percolation, and rate of transition from non-percolating to percolating is studied through the development of an equivalent resistor network model. And, lastly, the mechanism of electric loading-induced conductivity evolution in CNF/epoxy is studied experimentally.

4.2 Nanocomposite Piezoresistivity

4.2.1 Mechanisms of Piezoresistivity

Nanocomposite piezoresistivity is rooted in the dependence of nanocomposite conductivity on the formation of electrically percolated nanofiller networks. Electrical percolation refers to a nanofiller network being sufficiently well distributed and connected that electrons can travel from filler-to-filler and throughout the nanocomposite. However, even in well-connected nanofiller networks, the fillers are not in direct physical contact but separated by a thin layer of matrix material. Electrons are able to tunnel through this matrix layer and between sufficiently proximate fillers thereby enabling composite conductivity. Electron tunneling is the origin of piezoresistivity in nanocomposites because the equivalent resistance between neighboring fillers is a function of their separation [38] [87].

$$R_{\text{tunnel}} = \frac{h^2 t}{Ae^2\sqrt{2m\varphi}} \exp\left(\frac{4\pi t}{h}\sqrt{2m\varphi}\right) \tag{4.1}$$

In equation 4.1 h is Planck's constant, t is the distance between fillers, A is the overlapping area between fillers, m is the mass of an electron, e is the charge of an electron, and φ is the potential barrier height between fillers. Because nanofillers are themselves extremely conductive, the equivalent resistance between fillers dominates the resistivity of the nanocomposite. This means that electrical connectedness between fillers and therefore nanocomposite conductivity is not binary but depends on filler-to-filler proximity.

In the simplest interpretation, strain will alter the spacing between fillers thereby altering the equivalent resistance between fillers. However, upon closer scrutiny, piezoresistivity is more nuanced; strain will also influence the filler volume fraction and degree of filler randomness [88]. Filler volume fraction and randomness in turn influence the percolation probability and critical volume fraction respectively, and these factors influence the composite conductivity.

4.2.2 State of the Art Conductivity and Piezoresistivity Models

Existing models of CNT composite conductivity and piezoresistivity can be categorized as either equivalent resistor network based, percolation theory based, or analytical. Treated more diligently later, resistor network methods employ statistical methods of placing sticks within two or three-dimensional domains until a desired volume or weight fraction is reached [7] [38] [50] [89]. An equivalent resistor network is formed from the intrinsic CNT resistance and the tunneling resistance between neighboring CNTs that are less than the tunneling cutoff distance apart. Such models are well-suited to incorporate piezoresistivity with the addition of fiber reorientation. Strain reorients CNTs increasing inter-filler spacing and degrading percolated networks into non-conductive networks [88]. Comparison of resistance before and after strain determines the piezoresistivity of the composite for the volume fraction and filler parameters being investigated. Resistor network models provide exceptional physical insight into piezoresistive trends; however, due to the extreme number of sticks needed to form a percolated network, they are computationally burdensome and limited to extremely small scales not suitable to macroscale structural analysis. Additionally, fiber reorientation considers only uniaxial strain whereas an ideal piezoresistivity model should be more general.

Percolation based piezoresistivity models such as the one developed by Cattin et al. [78] modify percolation power laws with parameters extractable from experiments. This method has had considerable success in modeling negative piezoresistivity and has successfully been fit to a lot of independently collected experimental data. Again, however, these models consider only uniaxial tension or compression.

Analytical conductivity models derive explicit functions of filler parameters and assume an average inter-filler spacing [90] [91]. Takeda, Shindo, Kuronuma, and Narita developed an analytical expression for CNT composite conductivity as a function of σ_m matrix conductivity, σ_f filler conductivity, v volume fraction, v_c critical volume fraction, d_f filler diameter, l_f filler length, λ filler waviness ratio, and ξ percent network percolation [91].

$$\sigma_c = \sigma_m + \frac{4\xi v l_f}{3\pi\lambda^2 d_f^2 \left(\frac{4l_f}{\pi d_f^2 \sigma_f} + \frac{h^2 t}{Ae^2\sqrt{2m\varphi}} \exp\left(\frac{4\pi t}{h}\sqrt{2m\varphi}\right)\right)} \tag{4.2}$$

The percent network percolation ξ is an approximation independent of filler aspect ratio.

$$\xi = \frac{v^{1/3} - v_c^{1/3}}{1 - v_c^{1/3}} \tag{4.3}$$

Analytical conductivity models have had success in predicting CNT composite conductivity, but no work has been done to incorporate piezoresistivity.

4.2.3 Development of an Analytical Piezoresistivity Model

The insights of Takeda, Shindo, Kuronuma, and Narita [91] are leveraged by incorporating the influence of strain into their analytical conductivity model. To begin, the network percolation approximation ξ is replaced by the power-law developed in percolation theory.

$$P = K(v - v_c)^{\psi} \tag{4.4}$$

According to percolation theory, $\psi = \psi\left({}^{l_f}/_{d_f}\right) = 0.4$ in three-dimensional systems when the filler satisfies ${}^{l_f}/_{d_f} = 1$, and K is a constant of proportionality selected to ensure the percolation probability is one when the volume fraction equals one [92] [93]. According to Takeda, Shindo, Kuronuma, and Narita [91], the average inter-filler spacing is related to the volume fraction through a power-law in which the fillers become closer together as the volume fraction increases, $t = \alpha v^{\beta}$ [89] [91]. This is modified as

$$t = \alpha\left(v - v_c\right)^{\beta} \text{ [nm]} \tag{4.5}$$

ensuring that fillers transition abruptly from distant to proximate as the volume fraction exceeds the critical volume fraction. This modification also allows factors that influence critical volume fraction such as filler alignment and length to affect the inter-filler spacing.

The model herein developed assumes that filler parameters and composite conductivity versus weight fraction are known. Additionally, only filler volume fractions exceeding the critical volume fraction are considered. Piezoresistivity is incorporated into equation 4.2 by updating the volume fraction and critical volume fraction to reflect the strain state. Knowing the strained volume fraction and strained critical volume fraction, the percolation probability and average inter-filler spacing are recalculated. First, consider the volume fraction

$$v = \frac{\dfrac{w}{\rho_f}}{\dfrac{w}{\rho_f} + \dfrac{1-w}{\rho_m}} \tag{4.6}$$

as a function of the filler weight fraction w, filler mass density ρ_f, and the matrix mass density ρ_m [50] [91]. Because CNTs have a much higher modulus of elasticity than polymers, it can be assumed that they are rigid rendering the filler density constant while the matrix density changes due to strain. Let $U_{ij} = \delta_{ij} + \varepsilon_{ij}$ where δ_{ij} is the Kronecker delta and ε_{ij} is the infinitesimal strain tensor formed from the symmetric part of the gradient of the displacement.

$$\varepsilon_{ij} = \frac{1}{2}\left(\frac{\partial u_i}{\partial x_j} + \frac{\partial u_j}{\partial x_i}\right) \tag{4.7}$$

Volumetric strain is defined as ${}^{(V - V_0)}/_{V} = \det|U_{ij}| - 1$. Geometric considerations are then employed to relate deformed matrix density to volumetric strain as follows.

$$\rho_{m\,\text{deformed}} = \frac{(1-v)\rho_m}{\det|U_{ij}| - v} \tag{4.8}$$

Strain also degrades electrically connected networks through filler translation and reorientation decreasing percolation probability. In uniaxial tension, fillers reorient in a manner favoring the direction of the load [88]. Networks of CNTs with a preferred orientation have higher critical volume fractions due to the decreased likelihood of aligned fillers being in contact to form a connected network [94] [95] [96]. The excluded volume approach has had success in predicting critical volume fractions [50] [97], but here it is utilized to track the degradation of CNT networks due to strain. Excluded volume is the volume around a CNT through which the centerline of another CNT cannot enter to avoid penetration. The theory asserts that critical volume fraction is linked to the excluded volume of the filler rather than the true volume of the filler. The average excluded volume for a spherocylinder is

$$\langle V_e \rangle = \frac{4\pi}{3} d_f^3 + 2\pi d_f^2 l_f + 2 d_f l_f^2 \left\langle \sin(\gamma) \right\rangle_\mu \tag{4.9}$$

and the total average excluded volume for high-aspect ratio stick fillers is known to be in the range $1.4 \leq \langle V_{ex} \rangle \leq 2.8$ [97] [98]. The lower limit corresponds to randomly oriented sticks of infinite aspect ratio and the upper limit corresponds to perfectly aligned sticks or spheres. The volume of a spherocylinder CNT is denoted as V. The predicted critical volume fraction takes the following form.

$$v_c = 1 - \exp\left(-\frac{\langle V_{ex} \rangle V}{\langle V_e \rangle}\right) \tag{4.10}$$

Filler orientation is accounted for by $\left\langle \sin(\gamma) \right\rangle_\mu$. Let (θ_i, ϕ_i) orient the axis of the *i*th CNT in spherical coordinates. The CNT is allowed to take any value of ϕ_i while θ_i is limited to $-\theta_\mu \leq \theta \leq \theta_\mu$ and is considered to be randomly oriented if $\theta_\mu = {}^{\pi}/_{2}$ and perfectly aligned if $\theta_\mu = 0$. Let γ be the angle between the *i*th and *j*th fillers. The average of $\sin(\gamma)$ over all (θ_i, ϕ_i) and (θ_j, ϕ_j) is $\left\langle \sin(\gamma) \right\rangle_\mu$. Calculating $\left\langle \sin(\gamma) \right\rangle_\mu$ explicitly is quite tedious, but it can be well approximated by Monte Carlo integration techniques for random values of $[\cos(\theta_i),\ \cos(\theta_j),\ \phi_i,\ \phi_j]$ in $\sin(\gamma) = \|\mathbf{u}_i \times \mathbf{u}_j\| = [1 - \mathbf{u}_i \cdot \mathbf{u}_j]^{1/2}$ where $\mathbf{u}_i = [\sin(\theta_i)\cos(\phi_i),\ \sin(\theta_i)\sin(\phi_i),\ \cos(\theta_i)]^T$. Exact values of $\left\langle \sin(\gamma) \right\rangle_\mu$ are known to be 0

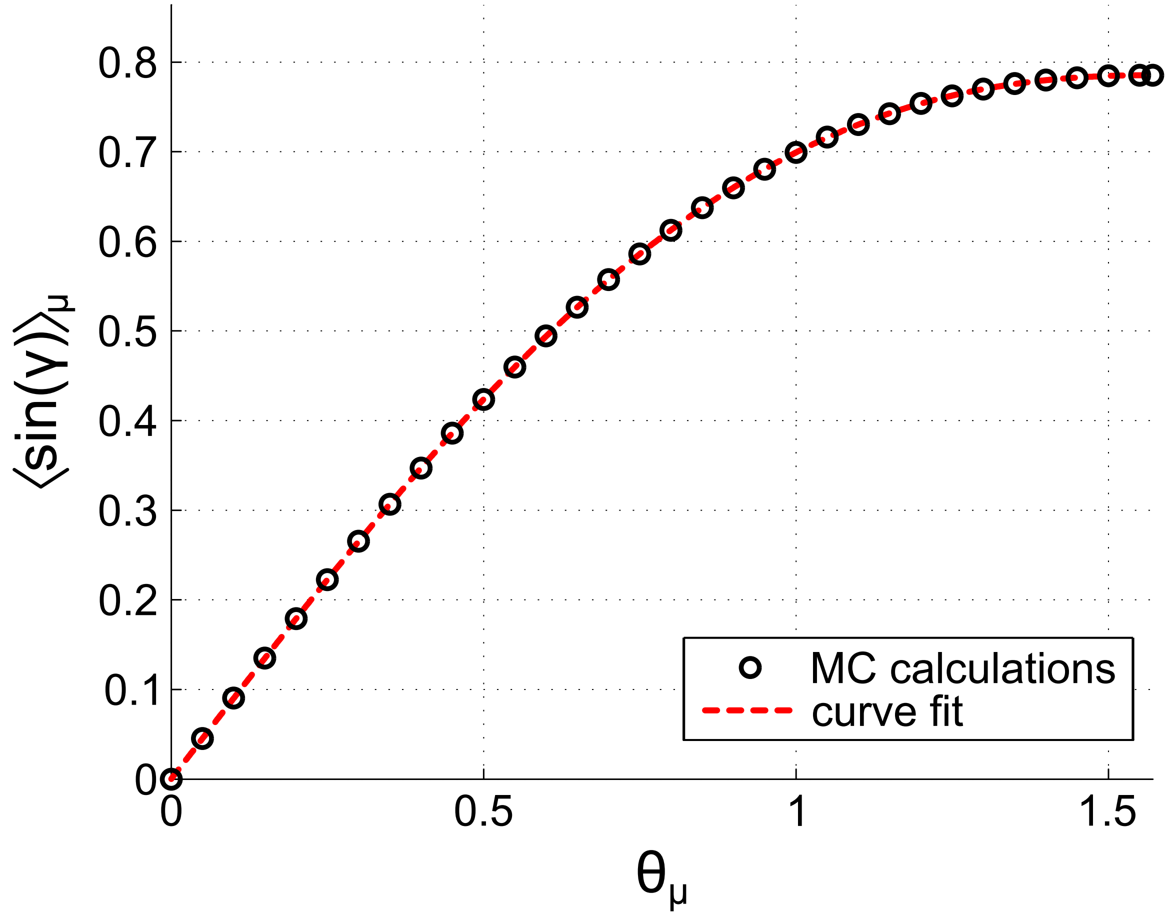

Figure 4.1: Fitting of Monte Carlo calculated $\langle \sin(\gamma) \rangle_\mu$ as a function of θ_μ.

and $\pi/4$ for $\theta_\mu = 0$ and $\theta_\mu = \pi/2$ respectively [98]. Fitting the Monte Carlo integration technique to a polynomial results in equation 4.11 and is shown in Figure 4.1.

$$\langle \sin(\gamma) \rangle_\mu = 0.018\theta_\mu^5 + 0.021\theta_\mu^4 - 0.234\theta_\mu^2 - 0.015\theta_\mu^2 + 0.909\theta_\mu. \tag{4.11}$$

Deformation is incorporated into critical volume fraction through the use of principal strains. Principal strains are the eigenvalues of the infinitesimal strain tensor ε_{ij} and represent the transformation from an arbitrary strain state to a shear free state of pure tension or compression. Recalling that fillers reorient in a manner that favors the direction of uniaxial tension, filler randomness should decrease as the largest principal strain increases. This relation is expressed as follows.

$$\sin\left(\theta_\mu\right) = \frac{1 + \varepsilon_3}{1 + \varepsilon_1} \tag{4.12}$$

Here, ε_1 and ε_3 are the first and third principal strains obeying $\varepsilon_1 \geq \varepsilon_2 \geq \varepsilon_3$. The fillers are initially randomly oriented implying $\theta_\mu = {}^{\pi}\!/_2$ and $\langle V_{ex} \rangle = 1.4$. To retain an easily implementable model, a simple linear relation between the deformed $\langle V_{ex} \rangle$ and the deformed $\langle \sin(\gamma) \rangle_\mu$ is assumed.

$$\langle V_{ex} \rangle = 2.8 - \frac{5.6}{\pi} \langle \sin(\gamma) \rangle_\mu \tag{4.13}$$

This form ensures the upper and lower limits on $\langle V_{ex} \rangle$ are satisfied for random and aligned networks, and the assumed linear dependence of $\langle V_{ex} \rangle$ on $\langle \sin(\gamma) \rangle_\mu$ is justified as follows. According to excluded volume theory [98], the total excluded volume of a system is given as $\langle V_{ex} \rangle = \langle V_e \rangle N_c$ where N_c is the critical concentration of fillers and $N_c \propto {}^{1}\!/_{l_f^2 d_f}$ for high aspect-ratio fillers such as CNTs. From equation 4.9, the product of $\langle V_e \rangle$ and N_c is a function of l_f, d_f, and linear in $\langle \sin(\gamma) \rangle_\mu$. Since CNTs have been assumed to be rigid, their dimensions do not change and $\langle V_{ex} \rangle$ only depends linearly on $\langle \sin(\gamma) \rangle_\mu$.

Variations in tunneling resistance contribute significantly to CNT composite piezoresistivity due to exponential dependence on inter-filler spacing [7] [87] [99]. The dependence of inter-filler spacing on strain is modeled by first recalculating equation 4.5 with the previously discussed strained volume fraction and strained critical volume fraction. This represents the average inter-filler spacing of an unstrained nanocomposite manufactured with the same volume fraction and critical volume fraction as is induced by straining. Next, let the average inter-filler spacing increase by the first principal strain when the volume fraction decreases. Conversely, the average inter-filler spacing decreases by the third principal strain when the volume fraction increases. This can be expressed by the following conditionals where v_s is the strained volume fraction.

$$t = \begin{cases} (1+\varepsilon_1)\alpha(v - v_c)^\beta \text{ [nm]} & \text{if } {}^{v}\!/_{v_s} > 1 \\ (1+\varepsilon_3)\alpha(v - v_c)^\beta \text{ [nm]} & \text{if } {}^{v}\!/_{v_s} < 1 \\ \alpha(v - v_c)^\beta \text{ [nm]} & \text{if } {}^{v}\!/_{v_s} = 1 \end{cases} \tag{4.14}$$

For a prescribed strain state, the strain-dependent parameters can be recalculated and equation 4.2 resolved for the new conductivity.

4.2.4 Comparison of Analytical Predictions to Experimental Literature

The analytical model is tested by comparison to the experimental results of Hu et al. [7] that provides manufacturing data consistent with the assumptions such as filler length ($l_f = 5$

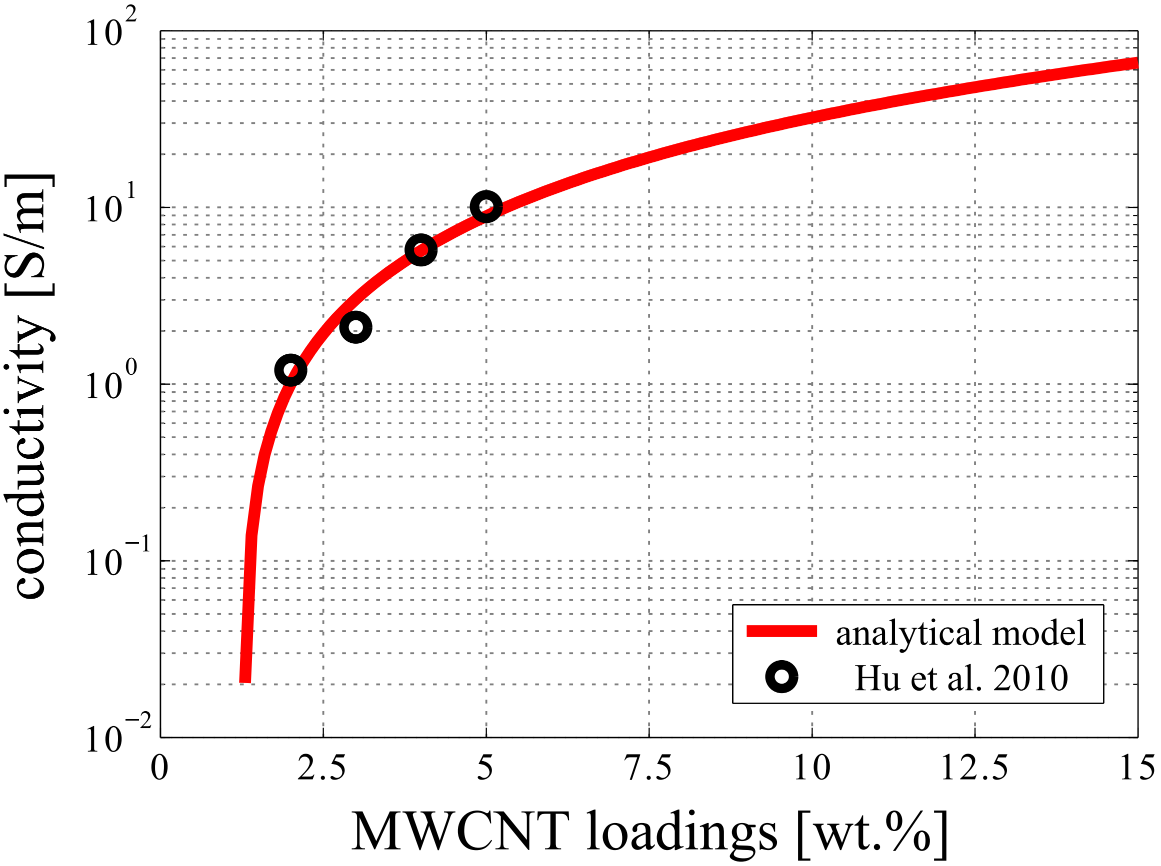

Figure 4.2: Fitting of piezoresistivity model to experimental data of Hu et al. [7] to determine unstrained parameters α and β.

µm), diameter ($d_f = 50$ nm), conductivity ($\sigma_f = 10^4$ S/m), and composite conductivity versus weight fraction. Additionally, the same numerical parameters are used as in their simulations such as straight CNTs ($\lambda = 1.0$) and potential barrier height ($\varphi = 1.5$ eV). The parameters α and β are selected to fit equation 4.5 to the experimental data. Figure 4.2 shows the results of this curve-fitting where $\alpha = 0.702$ and $\beta = -0.039$.

Consider a prismatic member in uniaxial tension with modulus of elasticity $E = 2.4$ GPa, Poisson's ratio $\nu = 0.35$, $\rho_m = 1100$ kg/m^3, and $\rho_f = 2100$ kg/m [38] [50] [100]. Elementary mechanics dictates that the infinitesimal strain tensor will have non-zero components only along the diagonal with $\varepsilon_{11} = {}^{\sigma_{11}}/_{E}$ and $\varepsilon_{22} = \varepsilon_{33} = -\nu\varepsilon_{11}$. The stress σ_{11} is selected to generate the desired strain and the predicted resistance change ratio ${}^{\Delta R}/_{R_0}$ is plotted against strain in Figure 4.3.

Examination of Figure 4.3 shows that the model predicts piezoresistive response very well for the entire tensile strain range and for compressive strain up to approximately -4000

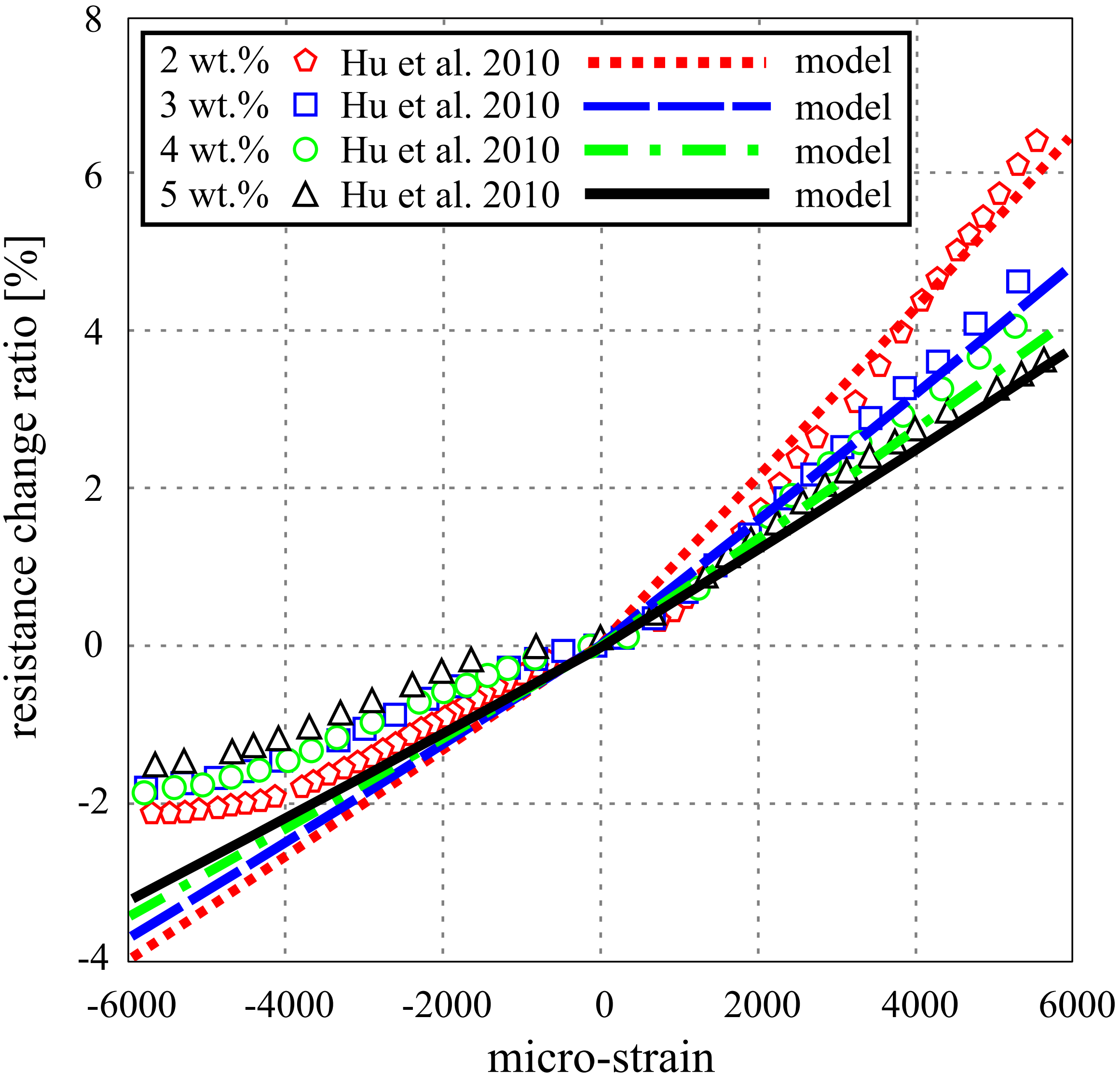

Figure 4.3: Comparison of analytical piezoresistivity model to experimental results of Hu et al. [7].

micro-strain. It shows a weakly nonlinear resistance change ratio that is corroborated experimentally by other researchers [37] [101]. The experimental results of Hu et al. [7] for weight fractions exceeding 2% are also predominantly linear in the range of -4000 to 6000 micro-strain, and the accuracy of the model developed in this chapter over this range exceeds the accuracy of existing resistor network/fiber reorientation models. However, piezoresistive saturation is not captured. Piezoresistive saturation occurs when the CNTs cannot move closer together, and the conductivity does not change with increasing compression. For the experiment cited in Figure 4.3, this occurs from -4000 to -6000 micro-strain. Additionally, for lower weight fractions, the experimental piezoresistive responses are more non-linear than predicted. Both of these artifacts are limitations of an average inter-filler spacing model. Some CNTs are much closer together than the average spacing predicts and consequently saturate with little applied strain whereas the average inter-filler spacing will not saturate within the limits of elastic deformation. Alternatively, some CNTs are much further apart than the average spacing predicts. Since the tunneling resistance depends exponentially on the inter-filler spacing, CNTs with inter-filler spacing much larger than the average will experience markedly greater changes in tunneling resistance for the same strain. Because better agreement is achieved at higher weight fractions, it can be deduced that the spacing between any two neighboring CNTs more closely matches the predicted average inter-filler spacing as weight fraction increases.

4.2.5 Finite Element Integration

Using CNT nanocomposites for self-sensing structures requires a piezoresistivity model that can be applied through existing tools of structural engineering. The model developed is readily adapted to finite element analysis by treating each element as a distinct domain whose change in conductivity can be determined by its nodal displacements. The gradient of the displacement field takes the following form in finite element analysis with linear tetrahedral elements.

$$\frac{\partial u_{ie}}{\partial x_j} = \sum_{A=1}^{4} d_{ie}^{A} \frac{\partial w_A}{\partial \zeta_k} \frac{\partial \zeta_k}{\partial x_j} \tag{4.15}$$

Here, d_{ie}^{A} is the finite element displacement solution of the *A*th node belonging to the *e*th element and repeated indices imply summation. The finite element interpolation functions are linear and denoted as w_A. Lastly, recognize ${}^{\partial \zeta_k}\!/\!{}_{\partial x_j}$ as the inverse of the Jacobian matrix the *jk*th element of which is expressed as follows.

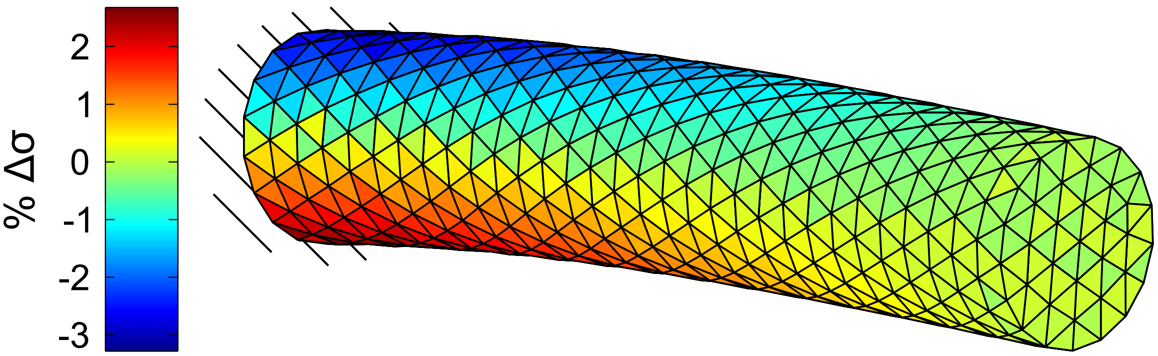

Figure 4.4: A 1 m beam with a 0.2 m diameter circular cross-section clamped at the left end and displaced downward by 0.01 m at the right end. Displacement is magnified by a factor of ten for visibility. The beam has the same material properties as used to generate Figure 4.3 at 2 wt.%. Note that the conductivity decreases where the beam is in tension and increases where the beam is in compression. The conductivity change is not symmetric (i.e. of equal change in magnitude in tension and compression) because of the exponential nature of the equivalent resistance between fillers.

$$\frac{\partial x_j}{\partial \zeta_k} = \sum_{A=1}^{4} x_{je}^{A} \frac{\partial w_A}{\partial \zeta_k} \tag{4.16}$$

The conductivity change due to a prescribed strain state can now be calculated on an elemental level. An example of the piezoresistivity model integrated with a finite simulation is shown in Figure 4.4.

4.3 Nanofiller Alignment

4.3.1 State of the Art Alignment Modeling

Rather than relying on experiments to study the influence of manufacturing parameters on nanocomposite conduction properties, considerable effort has been dedicated to electrically modeling nanocomposites. A popular approach involves placing individual fillers within a micro-domain until a desired volume fraction is reached [38] [7] [50] [95] [102] [103] [104] [105] [106] [107] [108] [89] [109] [110] [99]. The fillers are then treated as resistor elements with filler-to-filler junctions bridged by additional resistor elements the resistances of which are determined by, among other factors, the length of the filler-to-filler junction. This approach, while conceptually simple, has proven powerful in both its predictive capabilities and amenability to filler alignment [95] [103] [104] [106] [107] [89], filler clustering and aggregation [104] [108], and piezoresistivity [38] [7] [110]. With regard to systems of aligned fillers, studies have been conducted in two-dimensional [95] [106] [107] [89] and three-dimensional systems [7] [103] [104] [109]. Du et al. [95] examined the influence of nanofiller alignment on conductivity and percolation in two-dimensional systems and stacked sequences of two-dimensional systems. This research was motivated by thin, stacked nanocomposite films for transistors and flexible electronics. They found that conductivity exhibits a power-law dependence on alignment as well as loading. Furthermore, maximum conductivity is achieved for neither completely random nor highly aligned fillers. But, rather, it occurs for a certain degree of alignment between extremes. This study also included measurements at an angle with respect to the alignment direction. Thostenson et al. [106] studied the influence of filler alignment on conductivity in two-dimensional systems motivated by anisotropy induced by the presence of structural fibers. Li and Chou [107] examined the influence of nanofiller alignment on conductivity for both straight and wavy fillers in two-dimensional systems. Bao et al. [103] and Bao et al. [104] conducted studies in three-dimensional systems. They also found that the maximum conductivity in the alignment direction occurs for partially aligned fillers. Hu et al. [7] studied the influence of alignment on strain sensor sensitivity. Rahman and Servati [89] used two-dimensional simulations to study the influence of filler alignment on minimum inter-tube distance, inter-tube tunneling resistances, and sensitivity to mechanical strain. Of the previously cited studies, only Du et al. [95] examined percolation transverse to the alignment direction and this was limited to a two-dimensional case.

4.3.2 Development of an Equivalent Resistor Network Nanocomposite Model

For comparison to experimental literature [50] [111] [112], MWCNTs with length $l_f = 5$ µm and diameter $d_f = 50$ nm are herein simulated. The CNTs are assumed to be straight and modeled by their centerlines. The first endpoint of a CNT is randomly placed within a 10 µm × 10 µm × 10 µm cube. Using spherical coordinates, the second endpoint of a CNT is placed in the ($\tilde{x}$, $\tilde{y}$, $\tilde{z}$) domain according to equation 4.17.

$$\begin{aligned}
\tilde{x}_2 &= \tilde{x}_1 + l_f \cos(\theta)\sin(\phi) \\
\tilde{y}_2 &= \tilde{y}_1 + l_f \sin(\theta)\sin(\phi) \\
\tilde{z}_2 &= \tilde{z}_1 \pm \cos(\phi)
\end{aligned} \tag{4.17}$$

θ is randomly selected such that $0 \leq \theta \leq 2\pi$, $\cos(\phi)$ is randomly selected such that $\cos(\phi_m) \leq \cos(\phi) \leq 1$, and ± indicates that $l_f \cos(\phi)$ is randomly added or subtracted from z_1. The degree of alignment is controlled by ϕ_m. As depicted in Figure 4.5, CNTs must exist in one of two spherical cones the center of which is located at $(\tilde{x}_1, \tilde{y}_1, \tilde{z}_1)$. As ϕ_m goes to zero, the fillers become perfectly aligned in the $\tilde{z}$-direction. Alternatively, as ϕ_m goes to 90°, the spherical cones coalesce into a sphere and the CNTs are completely random. Examples of random and aligned nanofiller networks are shown in Figure 4.6.

Soft-core CNTs that are allowed to penetrate each other continue to be generated until the desired volume fraction is reached. Soft-core CNTs are used in this simulation because of the considerable reduction in computational time compared to hard-core fillers. While allowing fillers to penetrate each other is seemingly a physical impossibility, as noted by Yu, Song, and Sun [99], a hard-core model leads to high rejection rates during nanofiller generation whereas physical nanofillers can easily bend at apparently overlapping junctions due to their high aspect ratios thereby avoiding penetration.

Furthermore, some CNTs will inevitably extend beyond the boundaries of the 10 µm × 10 µm × 10 µm cube, and following the generation sufficiently many fillers to reach the prescribed volume fraction, these fillers are trimmed such that they end on the cube faces. As opposed to enforcing symmetric boundaries [104], this ensures that even for the same prescribed filler volume fraction, different simulations will have very slight differences in volume fractions remaining in the cube. This approach is favored over the symmetric boundary approach because real, physical nanocomposites have the same microscale variation in filler volume fraction. Representative examples of filler networks for different degrees of alignment are shown in Figure 4.6.

After the CNTs are generated and trimmed, standard geometric principles for calculating the shortest distance between two arbitrary line segments are employed in order to calculate the shortest distance between every pair of fillers. Consider two arbitrary fillers and let t be the minimum distance between them. Once t is calculated, three possibilities exist. First, if $t > d_f + d_t$ where d_t is the tunneling cutoff distance (d_t =1 nm [7]), the two fillers in consideration are not electrically connected. If a CNT is not electrically connected to any other CNTs, it is considered to be electrically isolated and eliminated from the simulation because it does not contribute to the nanocomposite conductivity. Second, if $d_f + d_m \leq t \leq d_f + d_t$ where d_m is an approximate value of the equilibrium distance between CNTs in a polymeric matrix under Lennard-Jones or van der Waals forces ($d_m = 0.5$ nm [7] [113]), there is a junction for electron tunneling between the two fillers in consideration. The tunneling resistance is calculated as shown in equation 4.1. It is herein assumed that the filler overlap area is approximately equal to the CNT cross-sectional area. And,

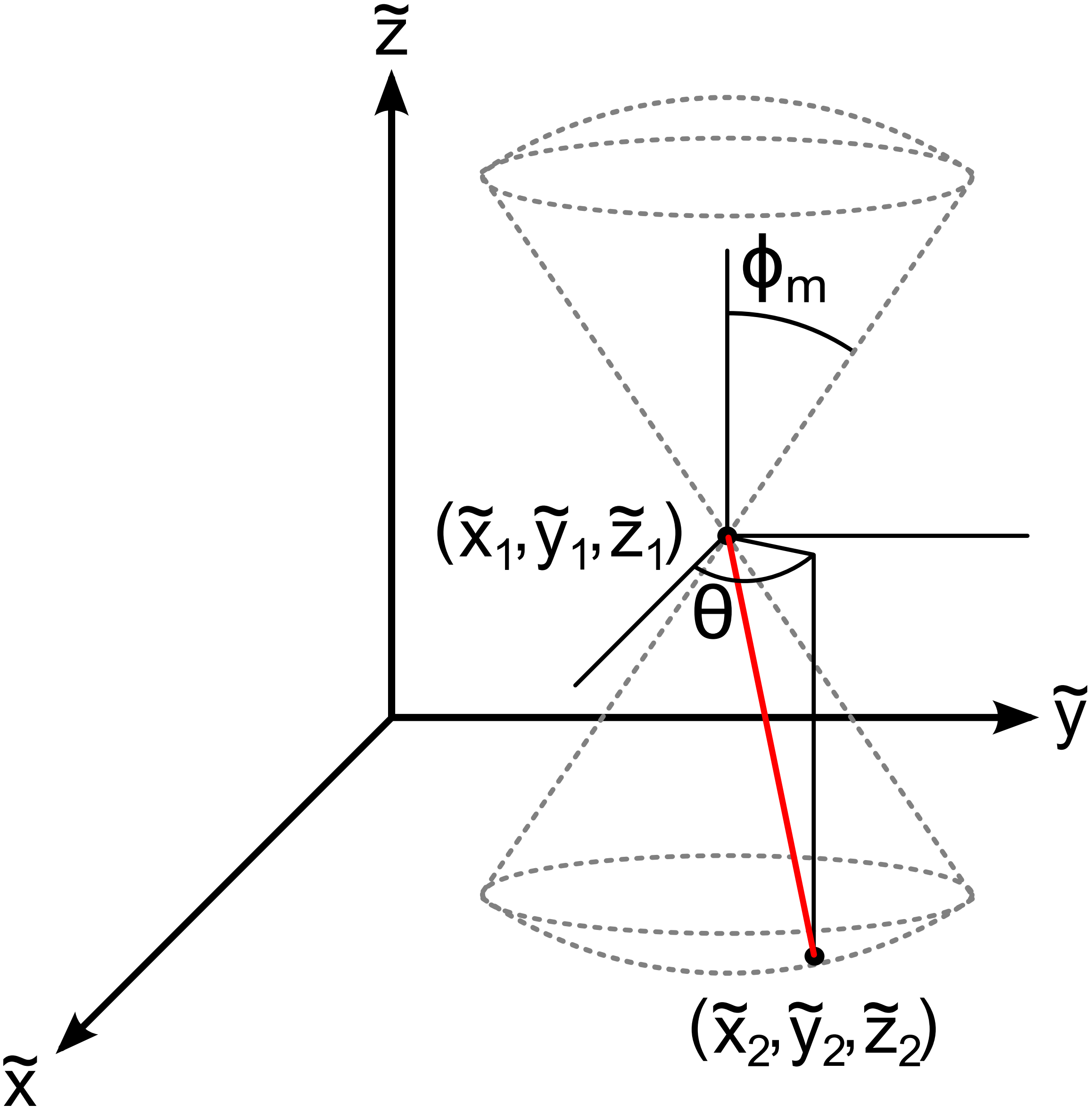

Figure 4.5: Depiction of filler placement within spherical cones. CNT shown in red.

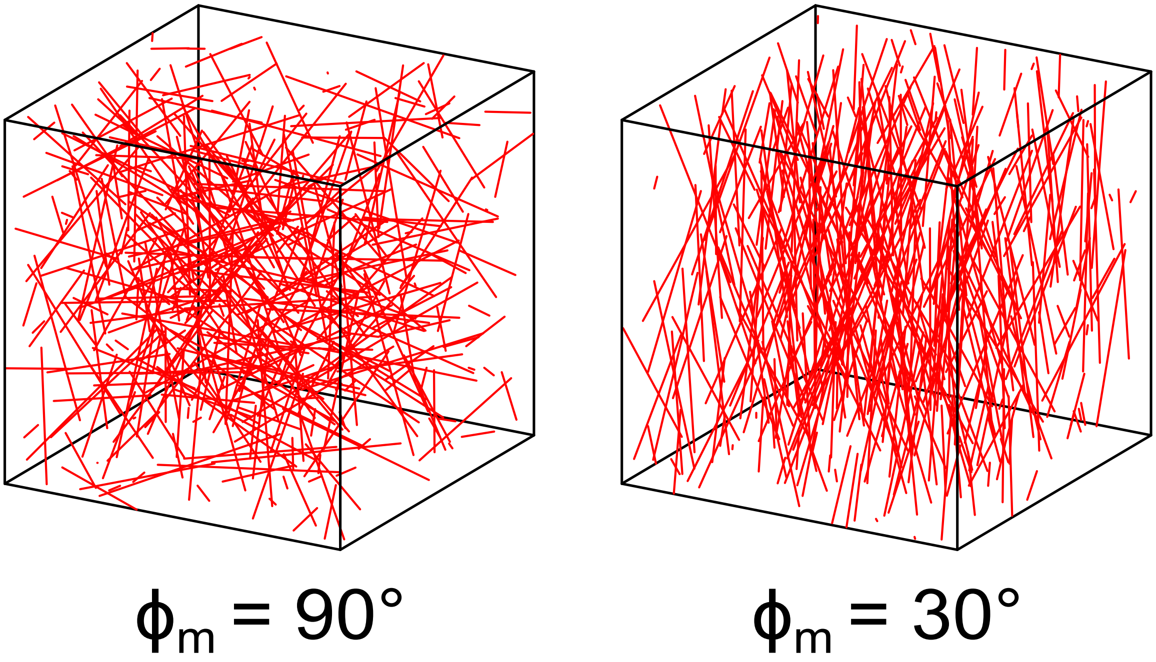
$\phi_m = 90°$

$\phi_m = 30°$

Figure 4.6: Representative random and aligned CNT networks. CNTs shown in red.

third, if $t < d_f + d_m$, the fillers are either penetrating, in contact, or closer than allowable by equilibrium conditions. In this case it is still assumed that a tunneling junction exists, but now equation 4.1 is calculated with $t = d_m$.

CNTs not eliminated due to isolation are discretized into finite elements by nodes at their endpoints and nodes generated at the tunneling junctions. Elements belonging to fillers have resistances due to the intrinsic resistivity of CNTs. This is calculated as follows.

$$R_e = \frac{4l_e}{\pi d_f^2 \sigma_{\text{CNT}}} \tag{4.18}$$

In the preceding equation, l_e is the element length and σ_{CNT} is the CNT conductivity. It is also possible, however, for fillers to not contribute to the nanocomposite conductivity and not be electrically isolated. This occurs when a group of fillers either form a chain or a closed loop without connection to a CNT network spanning the domain. Such groups can be eliminated by first identifying all of the elements that have a node on opposing faces of the cube. Next, all of the elements that share a node with elements that have a node on opposing faces of the domain are identified and grouped with the previously identified elements. This process of identifying elements that share a node with the previously identified elements continues until there is no change in the group of stored elements. Elements not stored are eliminated, and even for dense filler networks, this approach to eliminating isolated filler groups is quite expeditious. For visual elucidation, a schematic depicting the discretization of two fillers within the tunneling distance is provided in Figure 4.7.

After calculating elemental resistances of nanofillers and tunneling junctions, the finite element method is employed to determine the total resistance of the nanofiller network. The finite element stiffness matrices for resistor elements can be formed by considering a single resistor element in isolation as shown in Figure 4.7. By Ohm's law and following the direction of current flow indicated by the arrow, the current in node 1 is $I_1 = \frac{1}{R_e}(V_1 - V_2)$ and the current in node 2 is $I_2 = \frac{1}{R_e}(V_2 - V_1)$. These two relations can be expressed in matrix form as follows.

$$\begin{bmatrix} I_1 \\ I_2 \end{bmatrix} = \frac{1}{R_e} \begin{bmatrix} 1 & -1 \\ -1 & 1 \end{bmatrix} \begin{bmatrix} V_1 \\ V_2 \end{bmatrix} \tag{4.19}$$

Therefore, the elemental stiffness matrix of the *e*th resistor element takes the following form.

$$\mathbf{K}_e = \frac{1}{R_e} \begin{bmatrix} 1 & -1 \\ -1 & 1 \end{bmatrix} \tag{4.20}$$

Elemental contributions are then assembled into the global problem, $\mathbf{KV} = \mathbf{I}$, via standard finite element assembly procedures wherein Kirchhoff's current law at each node is satisfied through additive contributions of resistor element matrices. Dirichlet boundary conditions of 1 V and 0 V are applied on opposing faces of the cube and the global stiffness matrix is inverted by applying standard finite element procedures for boundary conditions to recover the voltage at every node in the domain. The magnitude of the resulting current in the *e*th resistor element can be found from equation 4.21.

$$I_e = \frac{1}{R_e} |V_1 - V_2| \tag{4.21}$$

V_1 and V_2 are the voltages of the two nodes belonging to the *e*th element. The total current entering the domain can be calculated by summing the current in elements touching the face on which 1 V was applied. The total resistance of the nanocomposite is then calculated via Ohm's law, and the conductivity is found by knowing the domain dimensions.

4.3.3 Influence of Alignment on Conductivity and Percolation

The model is tested for random, unaligned MWCNT networks by comparing its predictions to experimental literature [50] [111] [112] using $\varphi = 1.5$ eV and $\sigma_{\text{CNT}} = 10^4$ S/m [38] [7]. The values of simulation parameters are representative of MWCNTs and are selected from

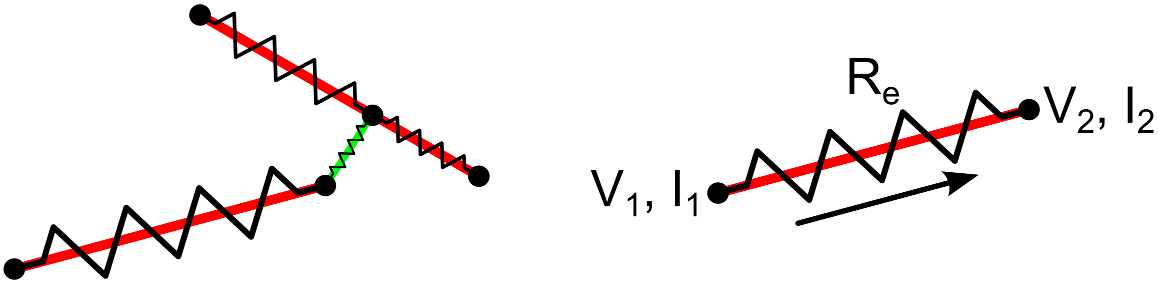

Figure 4.7: Left: schematic representation of two fillers (shown in red) discretized into resistor elements with a tunneling junction (shown in green). Right: depiction of current and voltages at nodes for derivation of finite element matrices.

Hu et al. [7] for comparison to experimental predictions. This comparison is shown in Figure 4.8. Because of the excellent agreement between the model and experimental data, there is confidence in its predictive capabilities and next the influence of alignment on conductivity in both the aligned and transverse directions is examined for $\phi_m = 15°$, 30°, 45°, 60°, and 75° as also shown in Figure 4.8. Consistent with observations by other researchers [95] [103] [104] [107], these results indicate that the greatest conductivity in the alignment direction is not achieved for the most highly aligned fillers. Also note that Figure 4.8 only shows conductivities for volume fractions exceeding the critical volume fraction.

Next, the influence of alignment on percolation probability in the transverse direction is examined. The simulation is considered to have percolated if a path of electrically connected CNTs exists which spans opposite sides of the domain transverse to the alignment direction. For each volume fraction considered, the simulation is run one hundred times. The percolation probability is then plotted against the volume fraction for $\phi_m = 15°$, 30°, 45°, 60°, 75°, and 90°, and the simulation results are fit to a sigmoid curve the equation for which is shown in equation 4.22.

$$P(v) = \frac{1}{1 + \mathrm{e}^{-\beta(v - v_c)}} \tag{4.22}$$

Here, v is the filler volume fraction and v_c is the critical filler volume fraction. The exponent β and the critical filler volume fraction are determined by the curve-fitting process, and the results of this analysis can be seen in Figure 4.9. Because the most interesting aspect of this analysis is the volume fraction at which each curve transitions from non-percolating to percolating, the volume fraction step size is refined near the critical volume fraction. Furthermore, although percolation probability is traditionally expressed as $P(v) \propto (v -$

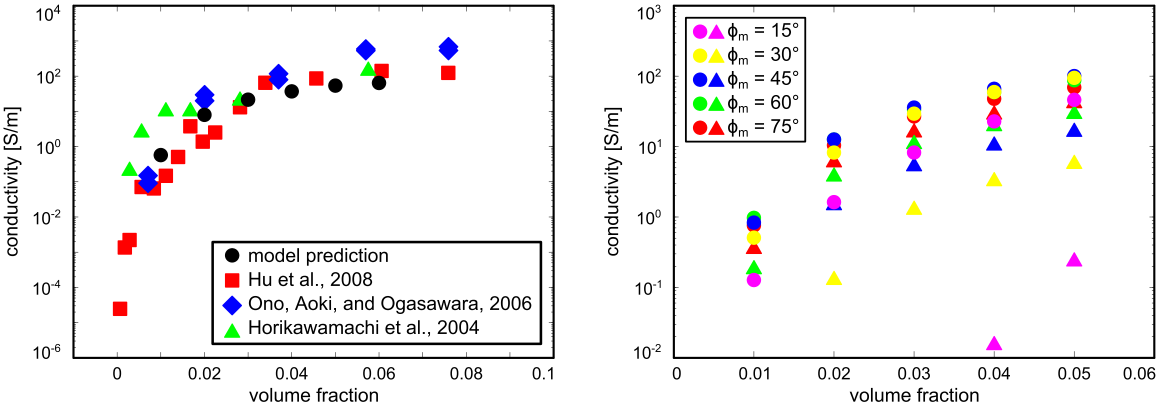

Figure 4.8: Left: comparison of model predictions for random, unaligned CNT networks and experimental literature. Right: model predictions of conductivity in the transverse (triangles) and aligned (circles) directions.

$v_c)^\beta$ [92] [93], these simulation results are instead fit to the sigmoid function because it can accommodate the entirety of the data (i.e. the non-percolating region) and therefore objectively select the critical volume fraction as a fitting parameter.

Valuable new insights regarding percolation transverse to the alignment direction can be obtained by plotting the curve-fitting parameters of equation 4.22 as shown in Figure 4.10. First, an exponential dependence of v_c on $\cos(\phi_m)$ is observed as $v_c \propto (\cos(\phi_m))^\alpha$ Second, an additional exponential dependence of β on $\cos(\phi_m)$ is observed as $\beta/\beta_{90^\circ} \propto 1-(\cos(\phi_m))^\alpha$. Note, however, that the exponent α in the preceding should not be interpreted as being equal in both instances. Rather, α is used as a generic term. The exponential dependence of v_c on $\cos(\phi_m)$ implies that much higher filler volume fractions are needed to ensure percolation in the transverse direction for even moderate alignment increases especially beyond $\phi_m = 30^\circ$. From a conductivity-based SHM material design perspective, this insight is particularly valuable. It implies that over-aligning fillers not only decreases the conductivity in the alignment direction but also markedly hinders the formation of percolating networks transverse to the alignment direction. Even increasing alignment from $\phi_m = 30^\circ$ to $\phi_m = 15^\circ$ approximately doubles the critical volume fraction thereby adding tremendous monetary cost to the material manufacturing process.

The second insight from these simulations regards the pronounced decay of the exponent β with increasing alignment; namely, $\beta/\beta_{90^\circ} \propto 1-(\cos(\phi_m))^\alpha$. Physically, larger values of β correspond to more rapid transitions from non-percolating to percolating. By normalizing the results in Figure 4.10 by β_{90°, it can be seen that there is a progressively slower transition from non-percolating to percolating as alignment increases. A similar

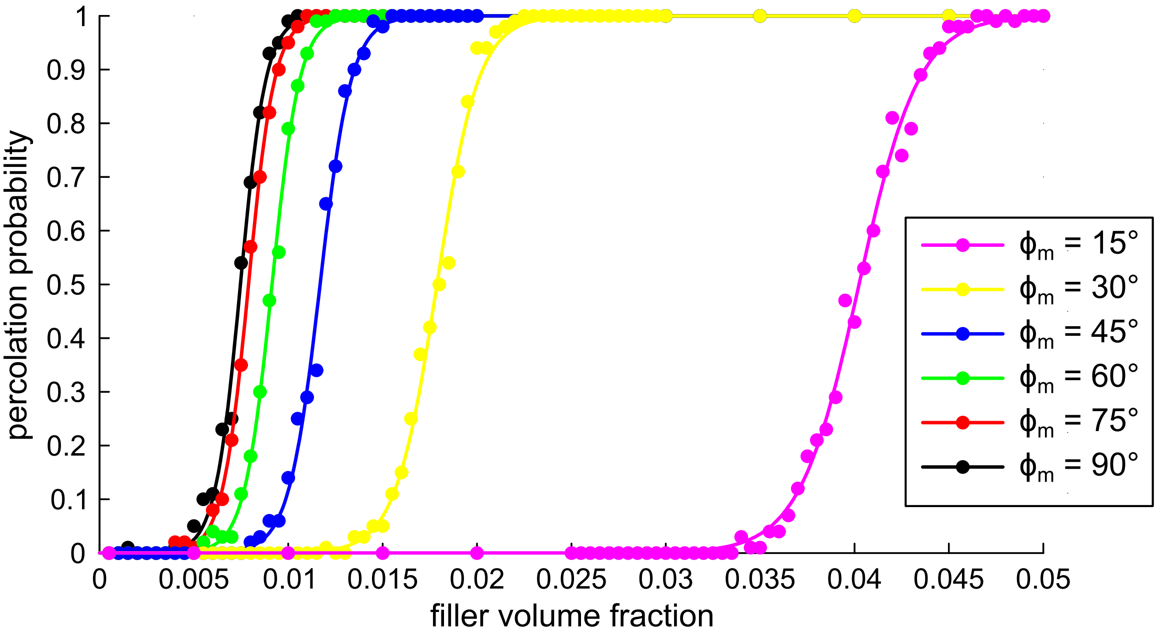

Figure 4.9: Transverse percolation probability simulation results (circles) and curve-fitting to sigmoid functions (lines).

trend is observed in the two-dimensional simulations of Du et al. [95]. Further insight can be gained by recognizing that the form of the proportionality for β/β_{90° is reminiscent of a result in percolation theory by Balberg et al. [114], $P_\perp \propto \sum_{i=1}^{N} \left[1 - (\cos(\theta_i))^2\right]^{1/2}$. Here, $P_\perp$ is the sum of the projections of the fillers in the transverse direction for N fillers and $-\theta_\mu \leq \theta_i \leq \theta_\mu$ where θ_μ is an angle governing the filler alignment not unlike ϕ_m as used in the simulations in this section. Employing the identity $\sin^2(\theta_i) + \cos^2(\theta_i) = 1$, $P_\perp$ can be rewritten as $P_\perp \propto \sum_{i=1}^{N} \sin(\theta_i)$. This result implies some relationship exists between the rate of transition from non-percolating to percolating transverse to the alignment direction and the projection of the nanofillers in the transverse direction which can be elucidated by plotting β/β_{90° against $\sin(\phi_m)$. This is shown in Figure 4.10 where β/β_{90° displays a decidedly linear dependence on $\sin(\phi_m)$ as evidenced by the curve-fitting process ($R^2 = 0.9945$). This linear dependence suggests that the rate of transition from non-percolating to percolating depends directly on the projection of the length of the filler in the transverse direction.

Next, the influence of alignment on conductivity in both the transverse and alignment directions as a function of ϕ_m is considered as shown in Figure 4.11. Again, consistent with the observations of other researchers [95] [103] [104] [107], the maximum conductivity in the alignment direction does not occur when the fillers are most highly aligned. And, as

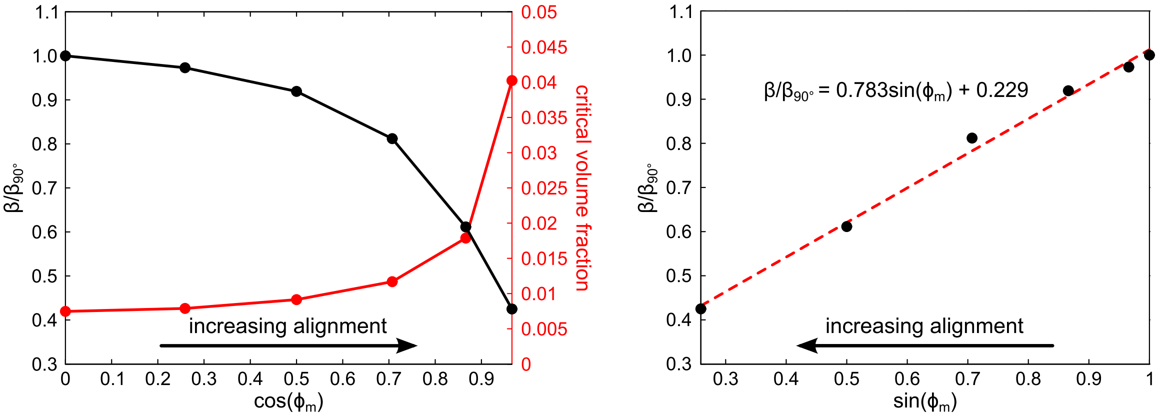

Figure 4.10: Left: curve-fitting transverse parameters β and v_c as a function of $\cos(\phi_m)$. The exponent values are normalized by β_{90°. Right: β/β_{90° as a linear function of $\sin(\phi_m)$.

also observed by Bao et al. [103], the angle of alignment at which maximum conductivity in the alignment direction is achieved is not the same for each volume fraction. Rather, higher volume fractions require higher degrees of alignment to achieve maximum conductivity in the alignment direction. Examining the left-most plot of Figure 4.11, it can be seen that there is a sharp drop in transverse conductivity as the alignment exceeds $\phi_m = 30°$. This implies that seeking maximum conductivity in the alignment direction can markedly reduce transverse conductivity; rather, a slightly lower alignment value will still enhance alignment conductivity but without great detriment to the transverse conductivity. Please note that filler volume fractions of $v_f = 0.01$, 0.02, and 0.03 do not have transverse conductivities plotted for alignments that did not percolate.

As depicted in Figures 4.10 and Figure 4.11, the simulations indicate that alignment results in a general degradation of percolation and conductivity transverse to the alignment direction, and this trend is only exacerbated as nanofillers become even more aligned. The physical mechanism for this degradation is speculated to be decreased nanofiller projection in the transverse direction or, synonymously, increased dependence on electron tunneling junctions. To better envision this, consider an electron traveling along a highly-aligned nanofiller network in the alignment direction. Because the nanofillers are much more disposed to run in the alignment direction, the electron can travel almost the entire length of the nanofiller before needing to tunnel to another nanofiller in order to progress along the network. Conversely, to travel transverse to the alignment direction, the electron will need to tunnel much more frequently to progress along the network because a much smaller projection of the nanofiller exists in the transverse direction. Therefore, as alignment increases, an increasing number of tunneling junctions are required for an electron to travel

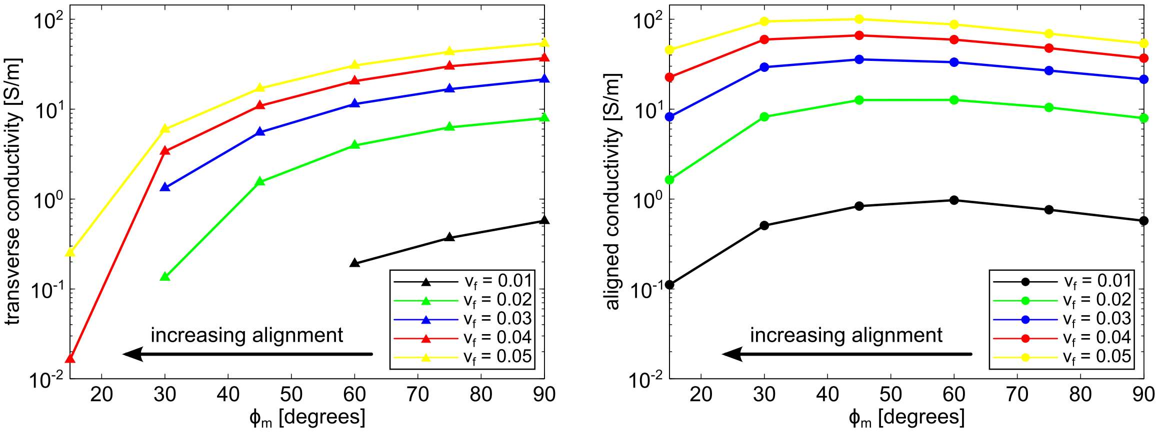

Figure 4.11: Left: transverse conductivity as a function of ϕ_m for each filler volume fraction. Right: aligned conductivity as a function of ϕ_m for each filler volume fraction.

transverse to the alignment direction. However, increasing alignment also diminishes the total number of tunneling junctions forming due to the decreased likelihood of nearly parallel sticks intersecting. These compounding factors very quickly destroy percolating networks transverse to the alignment direction. Just as aligning fillers destroys percolating paths transverse to the alignment direction, it similarly reduces transverse conductivity by decreasing the number of parallel tunneling junctions through the network.

4.4 Nanocomposite Conductivity Evolution

4.4.1 Mechanisms of Conductivity Evolution

Temperature increases due to electrical loading can cause nanocomposite conductivity to change or evolve over time. A possible explanation for this is that heating will cause thermal expansion in the matrix and fillers will consequently drift apart. This will result in decreased composite conductivity as observed in [85] [86]. Although the thermal expansion is initiated by electrical loading, this type of conductivity evolution is a result of piezoresistivity. In light of the previously developed piezoresistivity model, thermal expansion will cause an increase in inter-filler spacing, a decrease in filler volume fraction, and no change to filler randomness. Alternatively, localized Joule heating of the nanofillers can slowly activate electrons to tunnel thereby increasing tunneling probability and nanocomposite conductivity [83]. These competing effects are the reason some researchers have observed an increase in conductivity while others have observed a decrease in conductivity due to electrical loading. It is likely that the dominant mechanism depends on the matrix's thermal expansion properties. If there fillers experience a non-negligible drift apart due to thermal expansion, nanocomposite conductivity will drop. Conversely, if the thermal expansion is sufficiently diminutive, an increase in tunneling probability will dominate and nanocomposite conductivity will increase. Herein, the influence of electrical loading and elevated temperature on CNF/epoxy conductivity is studied.

4.4.2 Electrical Impedance Spectroscopy

Frequency-dependent properties can often be elucidated by examining the real and imaginary parts of the impedance through electrical impedance spectroscopy (EIS). Numerous researchers have leveraged EIS to develop equivalent circuit models that describe the behavior of nanocomposites [83] [101] [115] [116]. Nanocomposite equivalent circuits are parallel resistor-capacitor configurations of varying sophistication. To conduct EIS testing, a 6.35 mm $\times$ 6.35 mm square of CNF/epoxy is cut from the CNF/epoxy plate described in Chapter 5. Electrodes are attached by applying a colloidal silver paste (TedPella 16032) on opposing ends. Upon drying, copper tape is applied over the paste and a Wayne Kerr 6500B impedance analyzer measures the magnitude of the impedance and phase lag due to interrogation signals ranging from $f = 32.2$ kHz to $f = 1.9$ MHz at 40 °C, 50 °C, and 60 °C. The experimental real and imaginary parts of the impedance are formed by the first equality in equation 4.23 and equation 4.24 while the second equality represents the circuit equivalent.

$$\text{Re}(Z) = |Z|\cos(\theta) = R_s + \frac{R_p}{1+\omega^2 R_p^2 C_p^2} \tag{4.23}$$

$$\text{Im}(Z) = |Z|\sin(\theta) = \frac{\omega R_p^2 C_p}{1+\omega^2 R_p^2 C_p^2} \tag{4.24}$$

$|Z|$ is the measured impedance magnitude, θ is the measured phase lag, and ω is the interrogation angular frequency. R_s is the series resistor, R_p is the parallel resistor, and C_p is the parallel capacitor of the equivalent circuit shown in Figure 4.12. Plotting $-\text{Im}(Z)$ against $\text{Re}(Z)$ results in arcs as shown in Figure 4.12. By examining the shifts of these arcs due to elevated temperatures and leveraging the insights of previous researchers, the mechanisms of conductivity evolution in the CNF/epoxy composite can be deduced. For example, it has been noted that variations to R_s will shift the arc along the abscissa, variations to R_p will change the radius of the arc, and variations to C_p will rotate the arc about its center. R_p is the strain sensitive component [83]. As the temperature increases, the arcs expand outward consistent with an increase in R_p demonstrating the influence of temperature

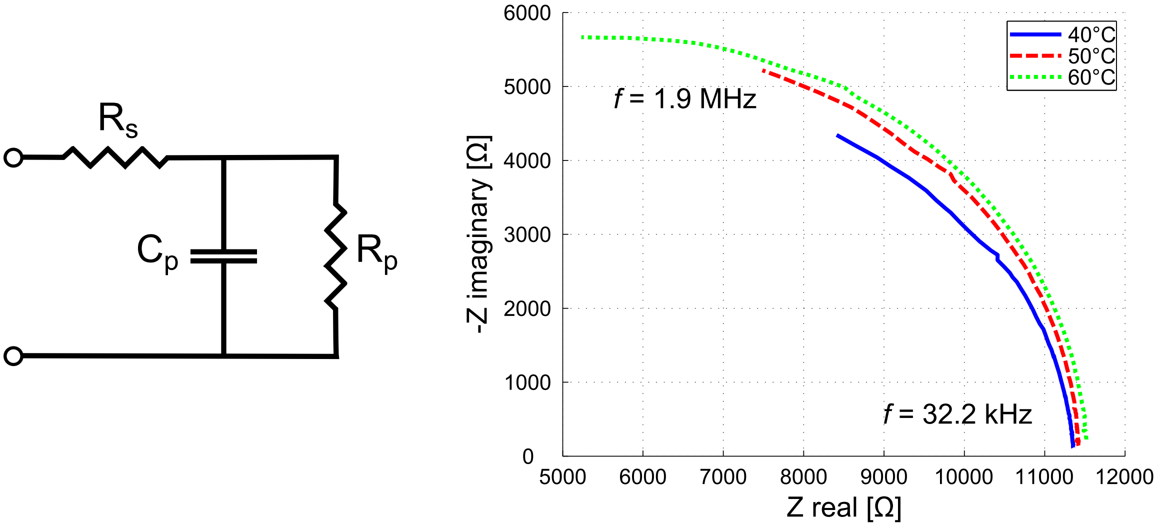

Figure 4.12: Left: equivalent circuit model for nanocomposites. Right: EIS plots of CNF/epoxy at increasing temperatures. Each plot is a parametric function of frequency beginning at the bottom right and increasing counter clock-wise to the maximum frequency at the top left.

on CNF/epoxy. However, the arcs also shift leftward along the abscissa with increasing temperature consistent with a decrease in R_s. The nature of this change is undetermined.

4.4.3 Conductivity Evolution Imaging

Based on the exponential trend of the EIT voltage measurements for CNF/epoxy shown in Figure 5.3, it is speculated that the conductivity also evolved exponentially under DC loading. In light of the reconstruction errors evident in Figure 5.4, let the conductivity of the *e*th element in the EIT reconstruction evolve as

$$\sigma_e\left(t\right) = \left(\sigma_i - \sigma_f\right) \mathrm{e}^{-\kappa t} + \sigma_f + \epsilon. \tag{4.25}$$

Here, σ_i is the initial conductivity, σ_f is the steady-state conductivity, ϵ is an error term resulting from electrode misplacements, and the exponent is a function of current magnitude $\kappa = \kappa\left(\left|-\sigma\boldsymbol{\nabla}\phi\right|\right)$ [117]. Now consider differentiating equation 3.11 with respect to time. Because the true conductivity is a function of time as shown in equation 4.25 but the initial conductivity estimate is not, ${}^{\partial \boldsymbol{\sigma}_0}\!/_{\partial t} = \mathbf{0}$ and ${}^{\partial \mathbf{F}(\boldsymbol{\sigma}_0)}\!/_{\partial t} = \mathbf{0}$. This implies

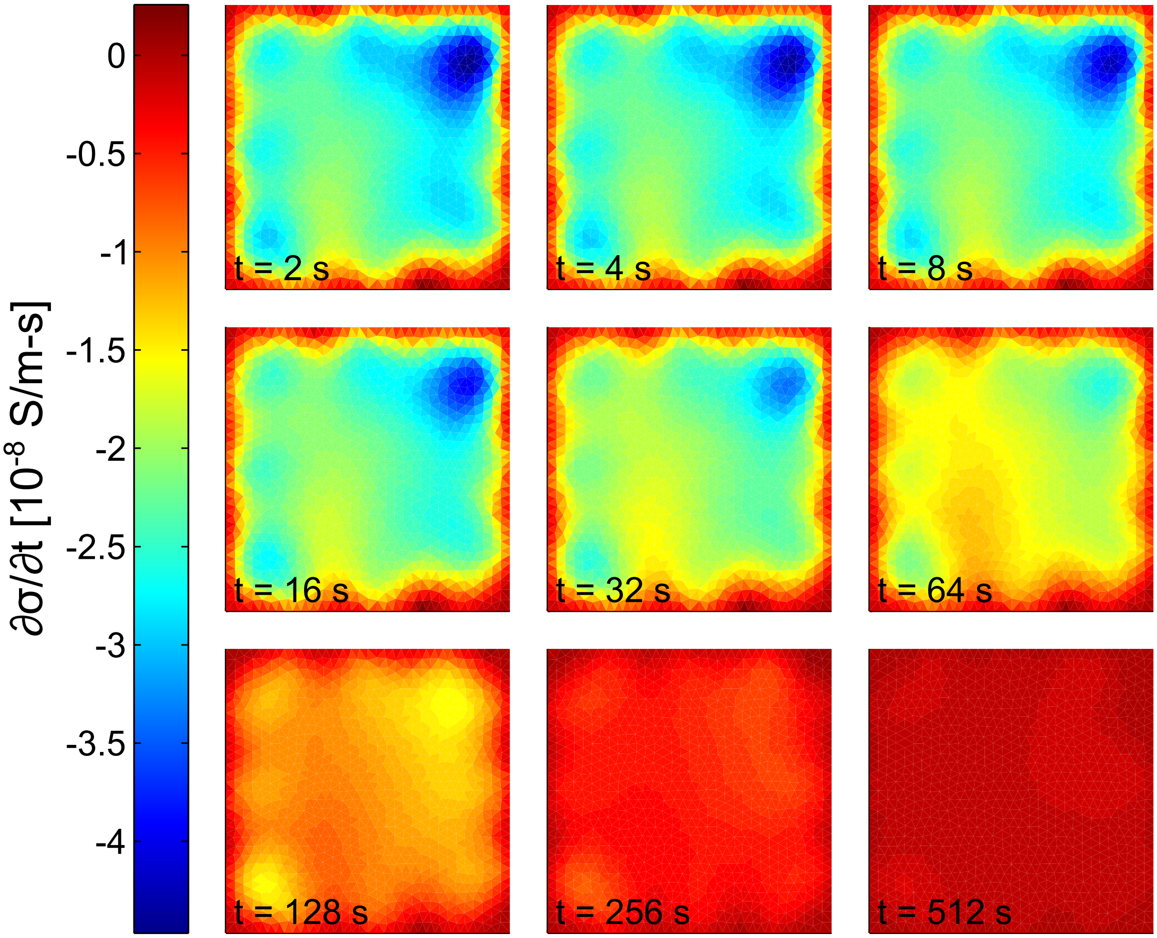

Figure 4.13: Conductivity evolution of undamaged CNF/epoxy at different times. Consistent with the voltage trends observed in Figure 5.3, ${}^{\partial\boldsymbol{\sigma}}/_{\partial t}$ goes to zero with increasing time.

$$\frac{\partial\left(\mathbf{V}_m - \mathbf{F}(\boldsymbol{\sigma}_0) - \dfrac{\partial\mathbf{F}(\boldsymbol{\sigma}_0)}{\partial\boldsymbol{\sigma}}(\boldsymbol{\sigma} - \boldsymbol{\sigma}_0)\right)}{\partial t} = \mathbf{J}\frac{\partial\boldsymbol{\sigma}}{\partial t} - \frac{\partial\mathbf{V}_m}{\partial t} = \mathbf{0}. \tag{4.26}$$

Equation 4.26 can now be rearranged as follows.

$$\mathbf{J}\frac{\partial\boldsymbol{\sigma}}{\partial t} = \frac{\partial\mathbf{V}_m}{\partial t} \tag{4.27}$$

${}^{\partial\boldsymbol{\sigma}}/_{\partial t}$ can be recovered from equation 4.27 through Tikhonov regularization to image the conductivity evolution in CNF/epoxy as shown in Figure 4.13.

Several speculations about the distribution of nanofillers can be postulated from conductivity evolution imaging shown in Figure 4.13. CNF distribution influences the rate of conductivity change and accounts for the variability seen in Figure 4.13. In regions of low filler concentration, the material is more sensitive to thermal expansion because there are fewer nanofiller junctions and the loss of even a few tunneling paths due to expansion will have a large influence to reduce conductivity. Conversely, regions of higher filler concentration can afford to lose more tunneling paths and remain conductive. Therefore, the conductivity evolves less rapidly. Other researchers have observed a similar increase in sensitivity to strain for nanocomposites with lower weight fractions [38] [7] [101]. Research has also established that nanocomposites with high weight fractions have a closer average inter-filler spacing [89] [91]. Since resistance between fillers depends exponentially on spacing, regions of high filler concentration should be more closely packed making them less sensitive to evolution via thermal expansion whereas regions of sparse filler density will be further apart on average and therefore much more sensitive to thermal expansion. In other words, thermal expansion will have a greater influence on a region of sparsely packed nanofillers because they are initially more distant than a region of the composite with densely packed fillers.

4.5 Summary and Conclusions

This chapter has explored unique features of nanocomposite conductivity through modeling and experimentation. First, an analytical model for CNT composite piezoresistivity was developed. This model accounts for the influence of strain on volume fraction, critical volume fraction, percolation probability, and inter-filler spacing. The model predictions agree well with experimental results in existing literature, and it has the ability to analyze the piezoresistive response of CNT composites under arbitrary straining whereas prevailing models examine only uniaxial strain. This adaptability lends itself to integration with the finite element method thereby enabling piezoresistive analysis of arbitrary strains at structural scales for the first time.

Next, the development of a nanocomposite equivalent resistor network model was presented in order to study the influence of nanofiller alignment on transverse network properties. Model predictions compare very favorably to experimental data for random CNT networks. Data from transverse percolation simulations were fit to sigmoid functions in order to determine the critical volume fraction and exponent β. These simulations indicate that both the transverse critical volume fraction and the rate of transition from non-percolating to percolating depend exponentially on the cosine of the alignment angle ϕ_m, but the rate of transition from non-percolating to percolating can also be expressed linearly in $\sin(\phi_m)$. The degradation of percolation and conductivity transverse to the alignment direction is believed to be due to decreasing filler projection or increasing dependence on electron tunneling in the transverse direction with increasing alignment. Consistent with existing literature, the maximum conductivity in the alignment direction does not occur for the highest degree of alignment and varies with filler volume fraction. Insights obtained from these simulations are indispensable to the development of nanocomposites employed for conductivity-based SHM wherein measurements transverse to the filler alignment direction are essential.

Lastly, the mechanism for the conductivity evolution of CNF/epoxy nanocomposites was studied. Conductivity evolution is speculated to be due to thermal expansion of the epoxy which causes fillers to drift apart thereby lowering the composite conductivity. EIS testing was performed at elevated temperatures in order to verify this. Consistent with existing equivalent circuit models, the EIS plots shifted in a manner which is attributable to piezoresistive effects. This implies that thermal expansion is responsible for conductivity evolution.

CHAPTER 5

Experimental Damage and Strain Detection in Nanocomposites via Electrical Impedance Tomography

5.1 Introduction

While EIT has received excellent treatment tracking damage to CNT thin films [6] [37], cementitious structures [77] [118] [119] [120], and sensing layers in GFRPs [60], no work has been done to utilize EIT on composites with a self-sensing nanocomposite matrix. Sensing skins, though powerful in their adaptability, have important limitations specifically concerning composite SHM. For example, damage sufficiently removed from the sensing layer or skin such as internal damage initiated by cyclic loading may go undetected. Superficial damage to the coating induced by hail, sleet, or dust in aerospace applications may also register as damage when there is no real threat to the structure. And, lastly, the additional weight of a coating may be unpalatable to weight-conscious aerospace structures. The self-sensing nanocomposite matrix approach herein studied circumvents these limitations. Because the matrix permeates every layer, the composite is sensitive to both internal and external damage and immune to false positives from superficial damage. Nanofillers are also of negligible parasitic weight.

Damage detection via resistance change methods applied to GFRP plates with nanofiller-rich matrices have been studied [4] [3] [59] [5]. These studies employ resistance change methods wherein, as the name suggests, resistance is measured between electrodes located along the edges of the structure or over the surface of the structure before and after a damage event occurs. Resistance values are then interpolated and large changes correspond to damage. This method, though computationally inexpensive, is limited by the density of the electrode array employed. That is, sparse arrays can only coarsely locate damage, but large arrays are prohibitively burdensome to implement. A gap in the literature therefore exists –

leveraging the superior imaging capabilities of EIT for damage detection in nanocomposite matrices has yet to receive diligent treatment. This chapter addresses that gap. EIT is used to experimentally locate damage in two materials, a CNF/epoxy plate and glass fiber/epoxy laminates with CB filler. The former is a simpler composite with only two phases. Simple through-hole damage is induced and detected as a proof of concept. The latter is a real structural laminate on which EIT sensitivity, ability to detect multiple damages, and ability to detect impact damage is studied.

Lastly, strain-induced conductivity changes are imaged via EIT in highly compliant CNF/PU composites. Highly flexible skins capable of tactile imaging and distributed strain sensing are of keen interest to robotic and biomedical applications wherein it is necessary to spatially resolve points of contact [121]. Locating contact within flexible planar skins has been approached by incorporating a sensing medium into a compliant matrix such that a grid is formed either by the sensing medium [122] or by line electrodes sandwiching the sensing medium [123]. Pressure-induced capacitance changes are then measured at the grid points so that pressure fields can be imaged by interpolating capacitance changes between measurement points. Despite the success of this approach, an important limitation is the dependence on a grid of sensors. That is, sensitivity to stimuli may be lost away from grid points particularly in a sparse grid. This can be circumvented by increasing the density of the grid, but this will necessarily add to both the manufacturing complexity and cost while simultaneously increasing the number of measurements necessary to form an image. Sparse grids, furthermore, are not particularly adept at discerning the geometry of pressure-induced strain fields. Nanocomposites such as CNF/PU have tremendous potential as an alternative to embedded grid systems for flexible skins capable of tactile imaging and distributed strain sensing when combined with EIT.

5.2 Carbon Nanofiber/Epoxy

5.2.1 Carbon Nanofiber/Epoxy Manufacturing

Pyrograf-III PR-24-XT-HHT (Applied Sciences Inc., Cedarville, OH) brand unfunctionalized CNFs with diameters ranging from 60 nm to 150 nm and lengths from 30 µm to 100 µm are dispersed in epoxy via horn sonication. Bisphenol F/aromatic diamine epoxy resin consisting of Epon 862 epoxide and Curative W curing agent (both from Momentive Specialty Chemicals, Columbus, OH) is used. CNFs are added at a concentration of 1 wt.%. This is a threshold value providing the maximum conductivity to the cured composite with the least increase in mix viscosity.

Acetone and Triton X-100 (Bioworld, Dublin, OH) surfactant are used to facilitate the dispersion of CNFs in epoxide. Acetone lowers the viscosity of the epoxide, and Triton X-100 modifies the surface of CNFs to enhance dispersion. Epoxide to acetone is used at a volume ratio of 2:1 while Triton X-100 to CNF is used at a weight ratio of 0.76:1. The CNF/epoxide/acetone/Triton X-100 mixture is sonicated for 5 minutes with a horn sonicator operating at 900 W and 20 kHz. The mixture is then stirred at 60 °C for 24 hours by a magnetic stirrer in order to facilitate the evaporation of acetone after sonication. Next, curing agent and BYK A-501 (BYK-Chemie USA Inc., Wallington, CT) air-release agent are added into the mixture. An Epoxide to curing agent weight ratio of 100:26.4 is used, and an air-release agent to epoxy weight ratio of 0.5:1 is used. The final mixture is stirred by hand for 5 minutes and degassed at room temperature for 30 minutes. Figure 5.1 is an optical microscope image showing the structure of CNF in the epoxide/acetone/Triton X-100 mixture after sonication. The degassed mixture is poured into a silicone mold and cured in an oven for 1 hour at 121 °C and 2.5 hours at 177 °C. The cured composite is cut by using a water-cooled diamond saw to 54 mm × 52 mm × 5 mm.

The CNF/epoxy plate was manufactured by Dr. Sila Gungor at the Pennsylvania State University as part of a collaborative project. The manufacturing methods described represent her work but are included for completeness [32].

5.2.2 Experimental Setup

EIT experiments are conducted using a Keithley 6221 high-precision AC/DC current source and a National Instruments PXIe-6368 16-channel analog input data acquisition (DAQ) card. The PXIe-6368 card is limited to voltage inputs of fewer than 10 volts with respect to the system ground while the boundary voltages are expected to exceed this. Therefore, inverting amplifier circuits are constructed from OPA227 op-amps with the gain shown in equation 5.1. Resistors are chosen so that the voltage output is within the DAQ range.

$$V_{out} = -\frac{R_2}{R_1} V_{in} \tag{5.1}$$

Electrodes are prepared in the following manner. First, the CNF/epoxy specimen is lightly sanded along its edges. Next, colloidal silver paste is applied on the specimen edges at evenly spaced, quarter-inch patches. Upon drying, copper tape is applied over the silver paint with tabs extended onto a wooden base. Lastly, a nail is driven through the copper tape tabs and to the wooden base. This ensures that alligator clips can be attached for current injections and voltage measurements without mechanically stressing the tape-to-paste electrode junctions. Contact impedances are estimated by comparing two and

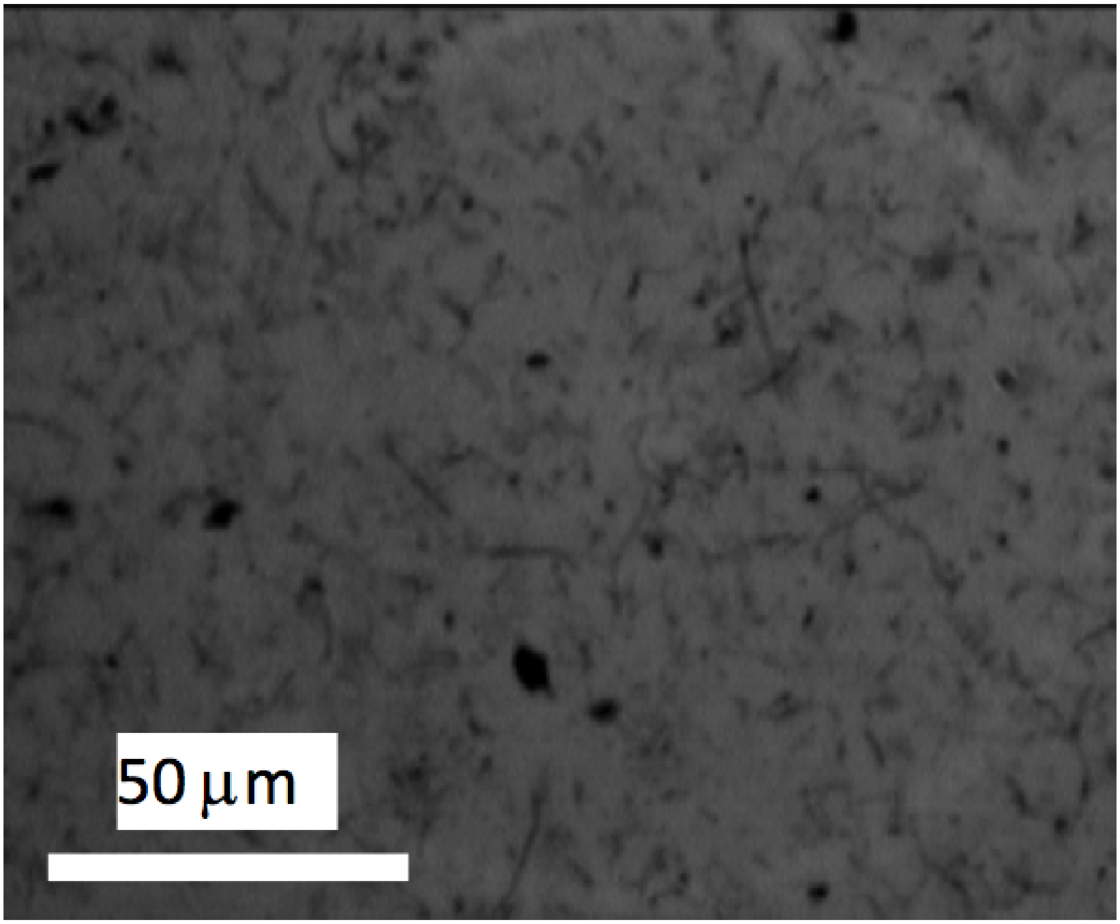

Figure 5.1: Optical microscope image of dispersion of CNF in epoxide/acetone/Triton X-100 mixture after 5 minutes of horn sonication conducted at 900 W and 20 kHz.

four-probe measurements. The amplifier schematic and experimental setup can be seen in Figure 5.2.

A 10 mA DC current is injected between electrode pairs for 20 minutes while the resulting voltage is measured at 128 Hz. Voltages are measured with respect to ground, and the data is smoothed with a moving average of half-width 256. Based on the observed voltage trend, measurements are fit to an exponential equation of the following form.

$$v = a\mathrm{e}^{bt} + c \tag{5.2}$$

An example of the electrode voltage fitting can be seen in Figure 5.3. The electrode pair differences necessary for EIT are formed offline as the difference of the voltage fits. The material is allowed to cool for at least three hours between current injections, and the voltage responses over time are tested for repeatability. This ensures the voltage drift is due to the conductivity evolution of CNF/epoxy and not electrode degradation. The voltage measurements increased as the experiment progressed implying that CNF/epoxy becomes less conductive under DC current injections.

5.2.3 Through-Hole Detection

A 6.35 mm diameter hole is drilled through the CNF/epoxy as indicated in Figure 5.4 and Figure 5.5. Figure 5.4 also shows the absolute conductivity image before and after damage. Consistent with the need for baseline subtraction as described in Chapter 3, an abundance of reconstruction errors are visible. However, damage is clearly recovered after baseline subtraction as shown in Figure 5.5.

5.3 Glass Fiber/Epoxy with Carbon Black Filler

5.3.1 Glass Fiber/Epoxy Manufacturing

Two glass fiber/epoxy laminated plates are identically manufactured with hand lay-up followed by vacuum bagging and reinforced by stitched unidirectional E-glass with 225 g/m^2 areal weight. Epon 8132 epoxy resin consisting of a bisphenol-A based epoxide diluted with alkyl glycidyl ether and Jeffamine T-403 polyetheramine curing agent is used as the matrix material. The mix ratio of epoxide to curing agent is 100:40 by weight. Cabot Black Pearls 2000 CB are used as nanofillers on account of their high structure. High structure CB is comprised of elongated clusters of individual CB particles that facilitate the formation percolated electrical networks at much lower filler volume fractions. Conversely,

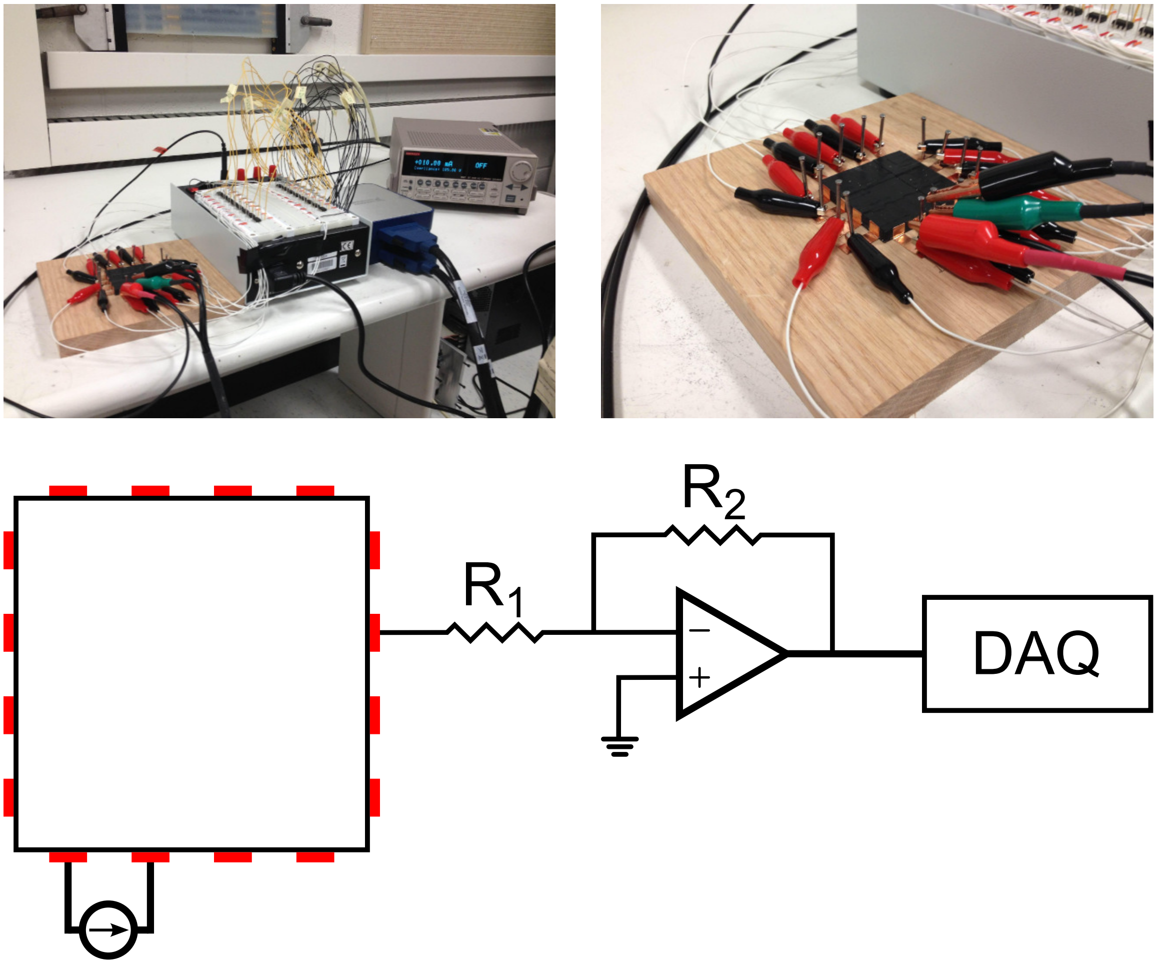

Figure 5.2: Top left: image of lab setup showing specimen, amplifier circuits, DAQ, and current source. Top right: close up of electrode connections. Bottom: schematic of electrodes, amplifier, and DAQ. Electrode voltage is measured with respect to ground and scaled by an inverting amplifier. The data is rescaled and electrode voltage differences are computed offline.

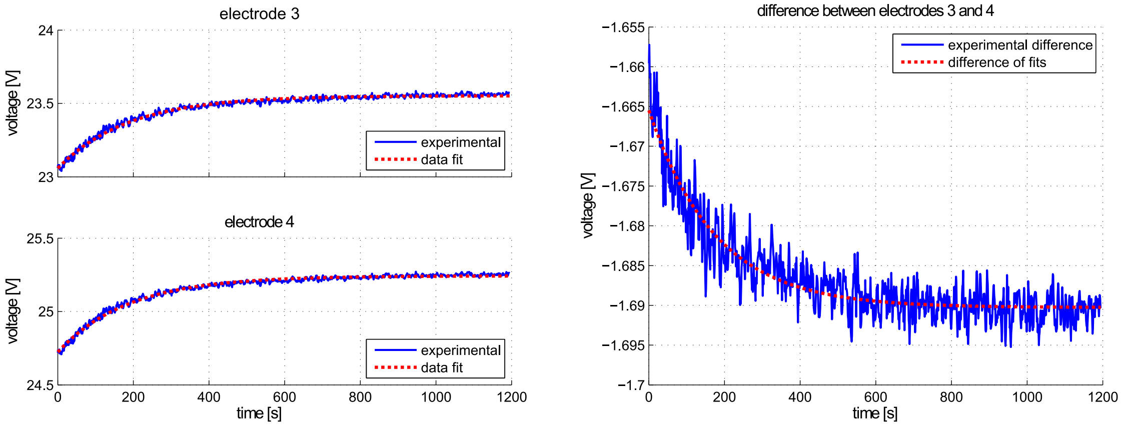

Figure 5.3: Left: representative DC voltages measured on electrodes three and four due to the first current injection. The data follows a decidedly exponential trend. Right: difference in voltage between electrodes three and four due to the first current injection. The voltage differences are not curve-fit. Rather, the dashed red line represents the difference of the voltage fits shown to the left.

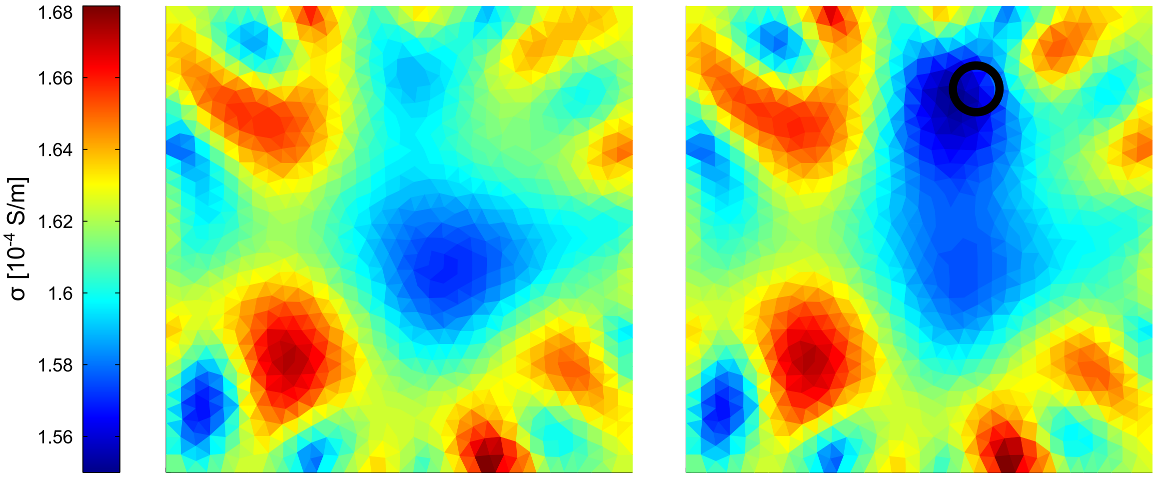

undamaged absolute reconstruction

damaged absolute reconstruction

Figure 5.4: Undamaged and damaged conductivity reconstructions of CNF/epoxy. Left: undamaged absolute EIT reconstruction. Note the abundance of conductivity reconstruction errors that may be falsely identified as damage. Right: damaged absolute EIT reconstruction. There is a new conductivity artifact that is actually due to damage. However, the same errors as in the undamaged case exist. The black circle indicates the true damage location and size.

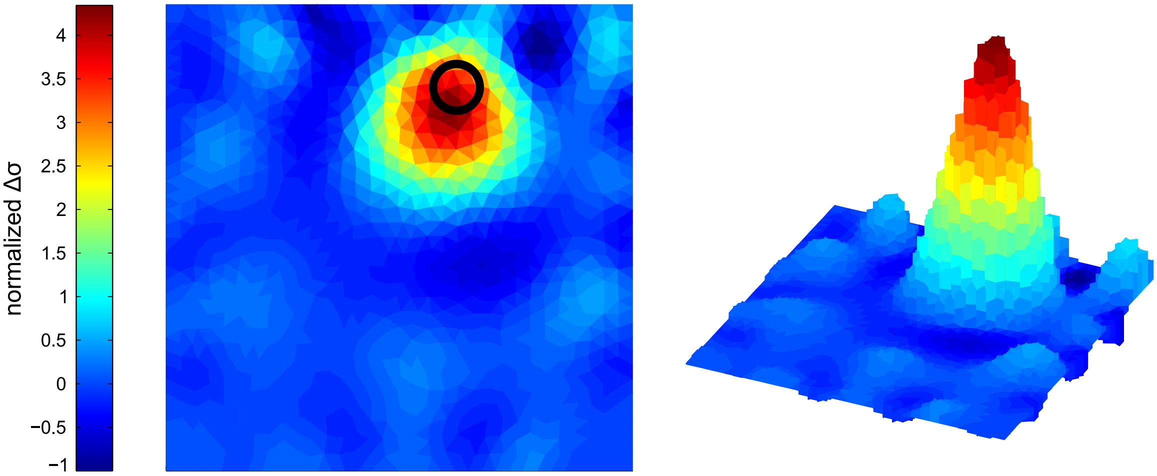

Figure 5.5: Damage detection results with undamaged baseline subtraction in CNF/epoxy. The black circle indicates the true damage location and size.

low structure CB is more spherical in shape and requires higher volume fractions to reach percolation.

CB particles are dispersed in epoxide by a magnetic stirrer and a sonication bath. CB is initially magnetically stirred in epoxide for 15 minutes at a rate of 250 rpm. The mixture is then mixed for 4 hours in an ultrasonic bath operating at 45 kHz and 55 W average power. Following sonication, the mixture is magnetically stirred for an additional 15 minutes at 250 rpm. Proper amounts of curing agent and BYK A-501 air release agent are then mixed into the CB epoxide, stirred by hand for 5 minutes, and degassed for 30 minutes.

Each glass fiber layer is impregnated with CB-filled epoxy using a hand roller. A total of 26 layers are used to produce a 4 mm thick plate with a stacking sequence of $[0/[0/90]_{6s}/0]$. A schematic illustration of the vacuum bag arrangement is shown in Figure 5.6. Aluminum foils are placed on the top and bottom of the impregnated laminate as electrodes in order to apply an AC field to the laminate while the matrix is still a dielectric liquid. This polarizes and chains the highly conductive CB particles through the thickness direction via dielectrophoresis. Without chaining the CB particles, the laminate would be several orders of magnitude more conductive in-plane than through the thickness direction. However, the chaining process makes the laminates nearly electrically isotropic. Based on [81], field parameters of 1000 V/cm and 1 kHz are selected to tailor the conductivity of the material. While the AC electric field is applied, the laminate is cured in an oven according to the following schedule: 30 minutes at 65 °C, 2 hours at 80 °C, and 3 hours at 125 °C. The cured composites have a calculated fiber volume fraction of approximately 0.60. Cured laminates are trimmed around the edges with a water-cooled diamond saw to final dimensions of 150

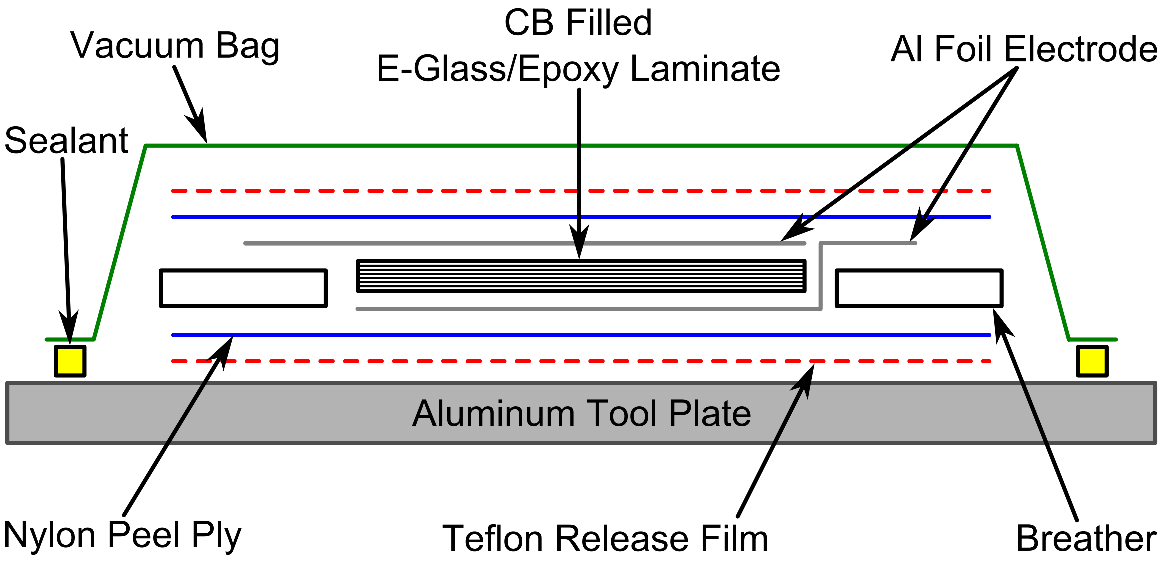

Figure 5.6: Cross-sectional schematic of the vacuum bag arrangement used to manufacture the laminated glass/epoxy plates.

mm × 150 mm × 4 mm. The 4 mm thickness dimension is as-molded.

The glass fiber/epoxy laminates with CB filler were manufactured by Dr. Sila Gungor at the Pennsylvania State University as part of a collaborative project. The manufacturing methods described represent her work but are included for completeness [32] [81].

5.3.2 Experimental Setup

DC currents are injected via a Keithley 6221 high-precision AC/DC current source at 0.025 µA, and voltages are measured with a National Instruments PXIe-6368 16-channel analog input DAQ card. Because of the high resistivity of the material, voltage buffer circuits are constructed from OPA227 op-amps thereby ensuring minimal current was leaked from electrodes that are not actively supplying current. Electrodes are prepared by first lightly sanding the GFRP plates along their edges. Next, colloidal silver paint patches are applied at even intervals and copper tape is applied over the silver paint with tabs extended onto a wooden base. A nail is then driven through the copper tape tabs and into the wooden base so that alligator clips could be attached without mechanically stressing the electrodes. Measurements are taken for 10 seconds at 128 Hz. Data is smoothed using a moving average of half-width 256. The experimental setup is shown in Figure 5.7.

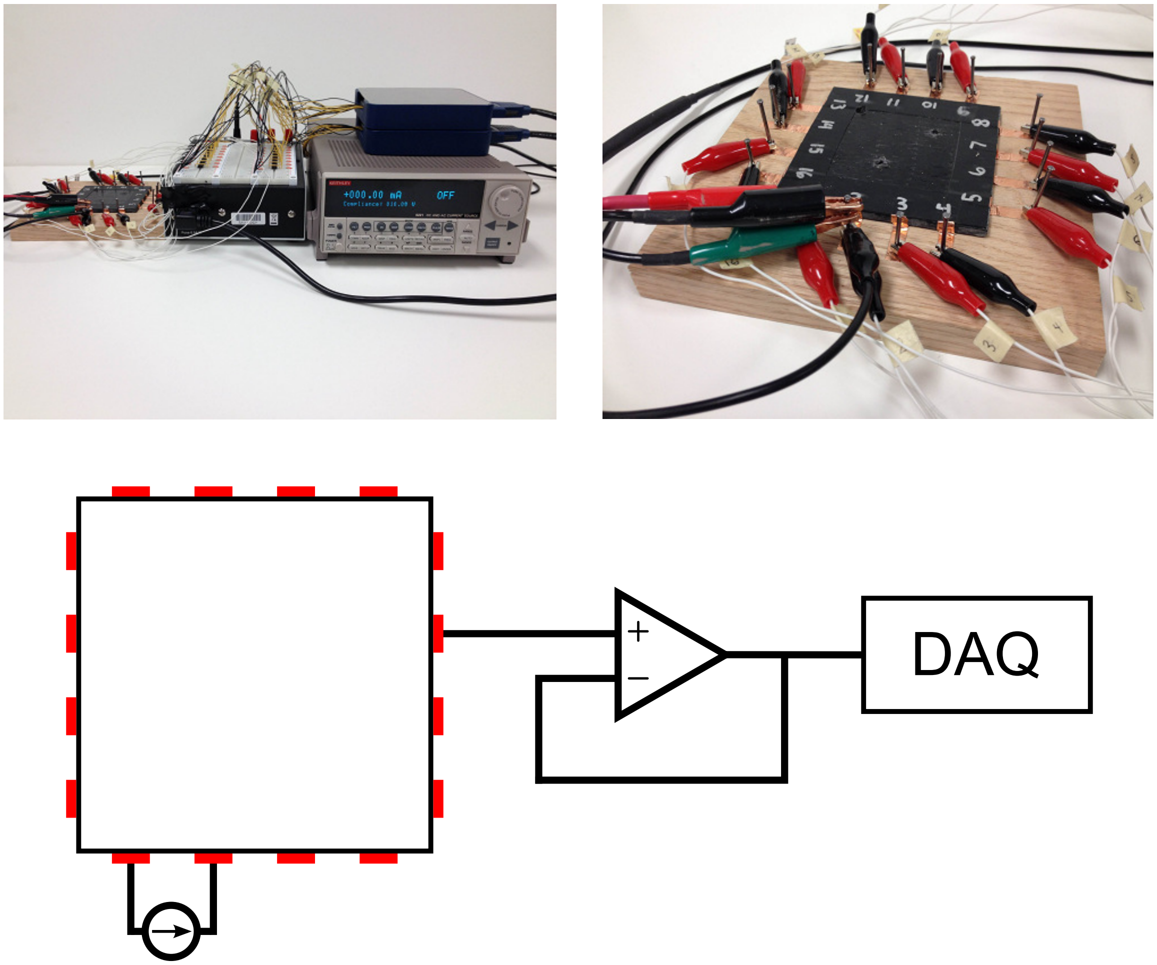

Figure 5.7: Top left: image of lab setup showing specimen, buffer circuits, DAQ, and current source. Top right: close up of electrode connections. Bottom: schematic of electrodes, buffer, and DAQ.

5.3.3 Through-Hole Detection

Sensitivity to damage, or the lower threshold of detectability, is an important aspect of SHM. In order to address this, through-hole damage with increasing size is induced, and EIT is employed to detect the damage. Prior to inducing through-hole damage, the first glass fiber/epoxy plate is cut to approximately 95 mm × 95 mm. Next, a 1.59 mm diameter hole is drilled through the specimen, and EIT measurements are collected. The hole is subsequently bored out to diameters of 3.18 mm, 4.76 mm, and 6.35 mm. EIT measurements are collected after each new diameter. Figure 5.8 shows the results of this analysis with the undamaged baseline subtracted.

The capability to detect multiple damages is another important SHM consideration. To examine this capability, a second hole is drilled through the same glass fiber/epoxy plate. The second hole is initially 1.59 mm in diameter. It is then bored out to 3.18 mm, 4.76 mm, and 6.35 mm in diameter. EIT measurements are again collected after each new diameter to assess whether the second through-hole could be detected. After the second hole is bored out to 6.35 mm, a third 6.35 mm diameter hole is drilled through the same glass fiber/epoxy plate. Figure 5.8 also shows the ability of EIT to detect multiple through-holes.

Each image shown in Figure 5.8 is normalized by the same value – the maximum error of the entire set of images. Normalizing the results in this manner enables them to be plotted on the same scale, and the influence of increasing through-hole diameter on the EIT reconstructions becomes obvious. However, this also causes smaller through-holes to appear much less prominently. Figure 5.9 shows the EIT images for a single 1.59 mm hole and a single 3.18 mm hole each plotted individually and normalized by their respective maximum values. The 3.18 mm hole is now immediately visible, but the 1.59 mm hole is arguably not discernible from the image noise. For the parameters employed, it can therefore be concluded that EIT is sensitive to through-holes in glass fiber/epoxy laminates with CB filler at least as small as 3.18 mm in diameter but larger than 1.59 mm in diameter.

Next, consider the EIT image of a small through-hole in the presence of a larger through-hole as shown in Figure 5.8 F). Because the larger through-hole dominates the image, the smaller through-hole may go undetected. However, this can be circumvented by using a different baseline. As shown in Figure 5.10, using the single 6.35 mm diameter through-hole reconstruction shown in Figure 5.8 D) as the baseline, the second 3.18 mm diameter through-hole becomes immediately visible.

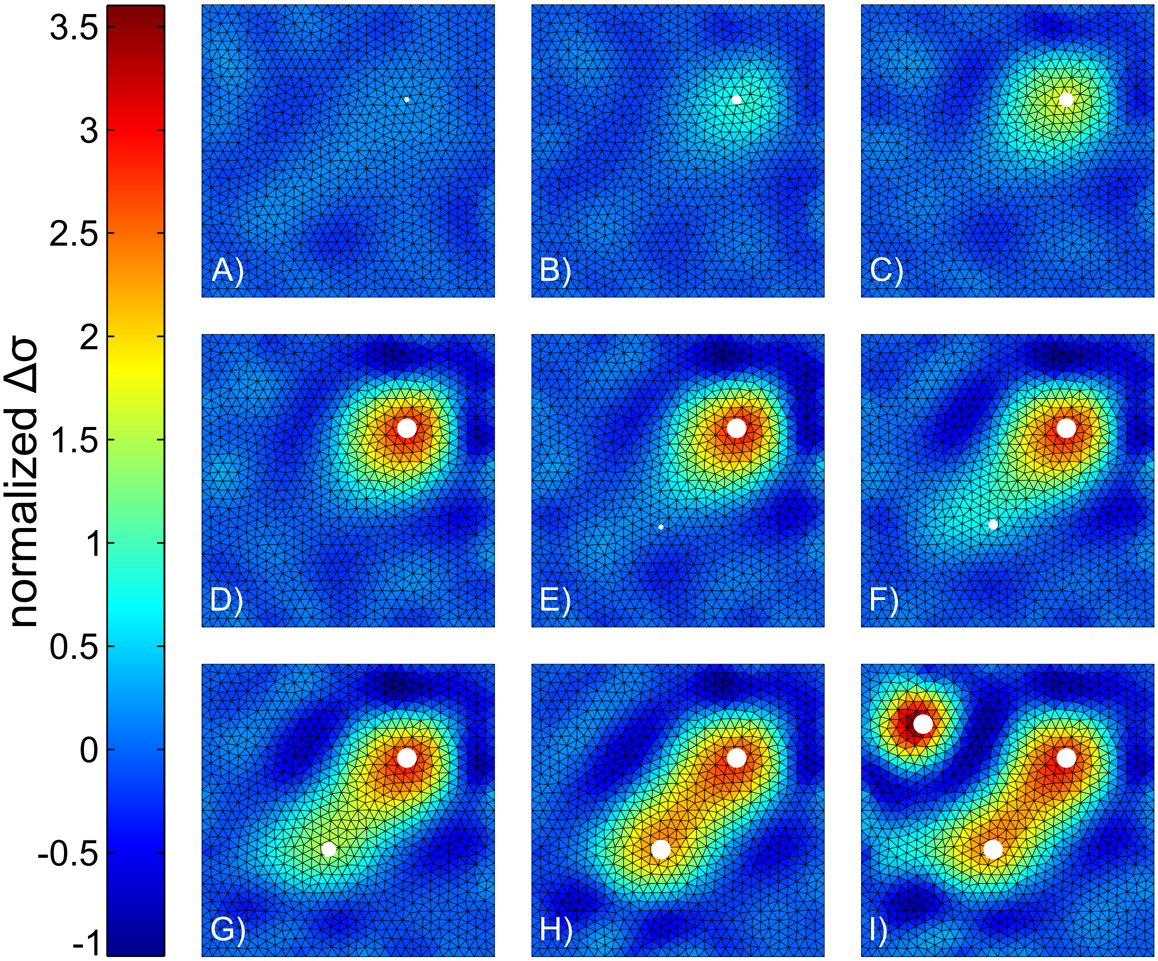

Figure 5.8: Sensitivity and multiple damage detection. Each image is normalized by the same value – the maximum error of the entire set of images. The undamaged baseline is subtracted. Through-hole size and location indicated by white circles. Diameters of each through-hole are as follows. A) 1.59 mm. B) 3.18 mm. C) 4.76 mm. D) 6.35 mm. E) 6.35 mm and 1.59 mm. F) 6.35 mm and 3.18 mm. G) 6.35 mm and 4.76 mm. H) 6.35 mm and 6.35 mm. I) 6.35 mm, 6.35 mm, and 6.35 mm.

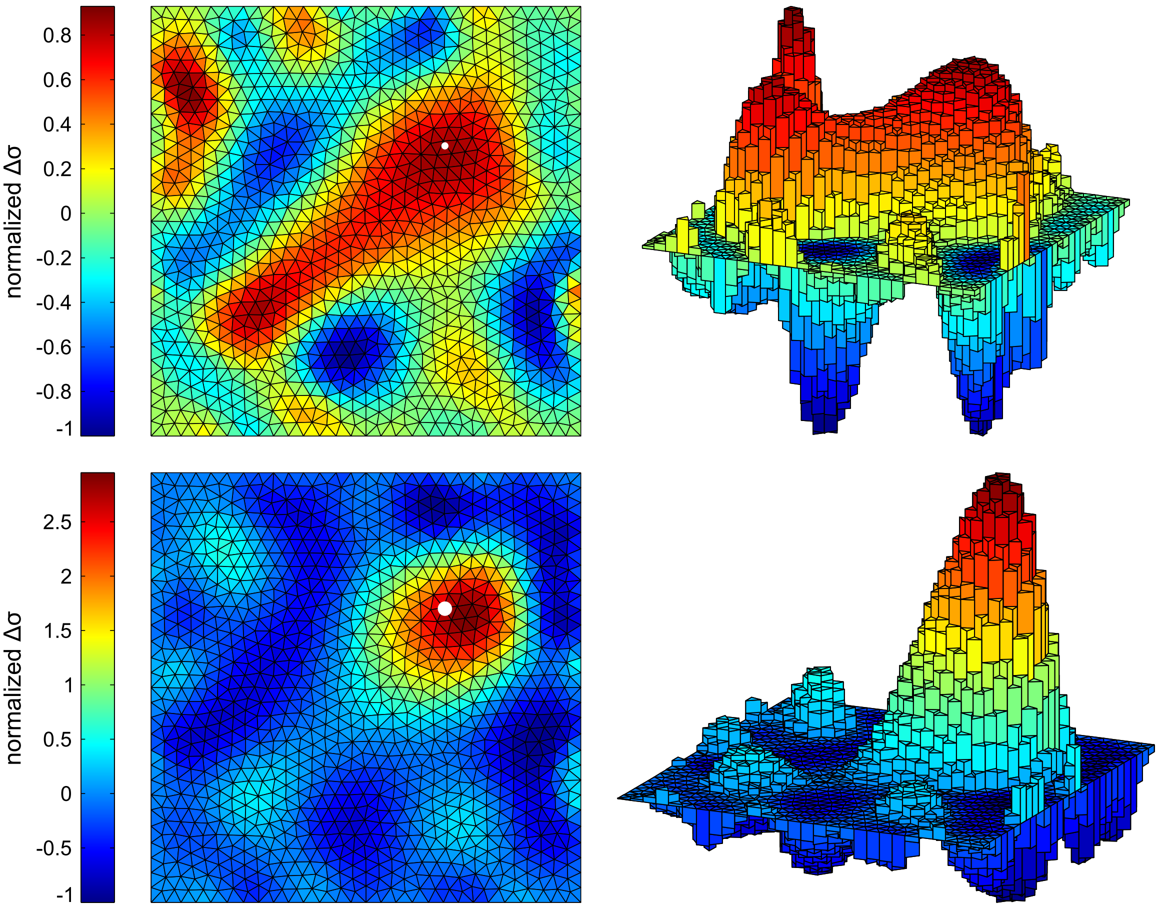

Figure 5.9: Sensitivity to small through-holes. Images are each individually normalized by their respective maximum errors. The undamaged baseline is subtracted. Through-hole size and location indicated by white circles. Top: EIT reconstruction with a single 1.59 mm diameter hole. Bottom: EIT reconstruction with a single 3.18 mm diameter hole.

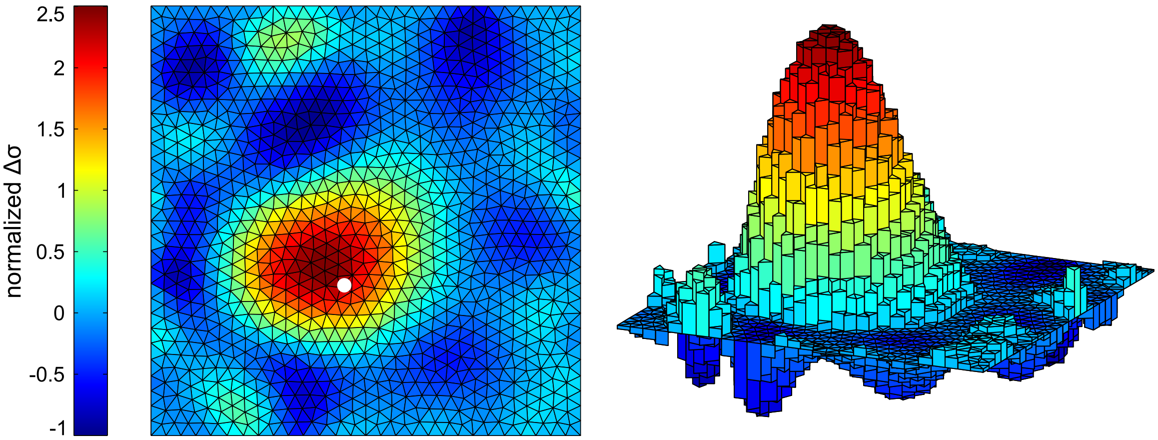

Figure 5.10: EIT reconstruction of a second 3.18 mm hole normalized by its maximum value. The single 6.35 mm diameter through-hole baseline shown in Figure 5.8 D) is subtracted. Damage size and location indicated by the white circle.

5.3.4 Impact Damage Detection

Because low-velocity impacts often induce delamination [124], their detection is an important SHM consideration. Inasmuch, a second, identical GFRP plate is impacted via drop tower at 50 J. The indenter is hemispherical with a diameter of 12.7 mm, and the plate is cut to approximately 101 mm × 152 mm in order to accommodate the impact machine with simply-supported, symmetric boundary conditions. The impact resulted in a slight indentation at the impact location and the formation of a crack initiating at the indentation and running along the fiber direction on the top surface of the plate. The post-impacted plate is shown in Figure 5.11.

While taking EIT measurements after the impact, it is noted that several electrodes are unresponsive, and it is believed that the impact damaged the electrodes. They consequently had to be reapplied. Despite careful meticulousness, it is impossible to replace electrodes with exact precision so some discrepancies exist between electrode placement in the undamaged baseline and the damaged reconstructions. This results in additional errors in the EIT reconstruction. Nonetheless, these errors appear to be minimal. Figure 5.12 shows the EIT image of impact damage. The location of the indenter and the EIT reconstruction align well, and the EIT reconstruction has an elongated region of conductivity change that captures the crack damage.

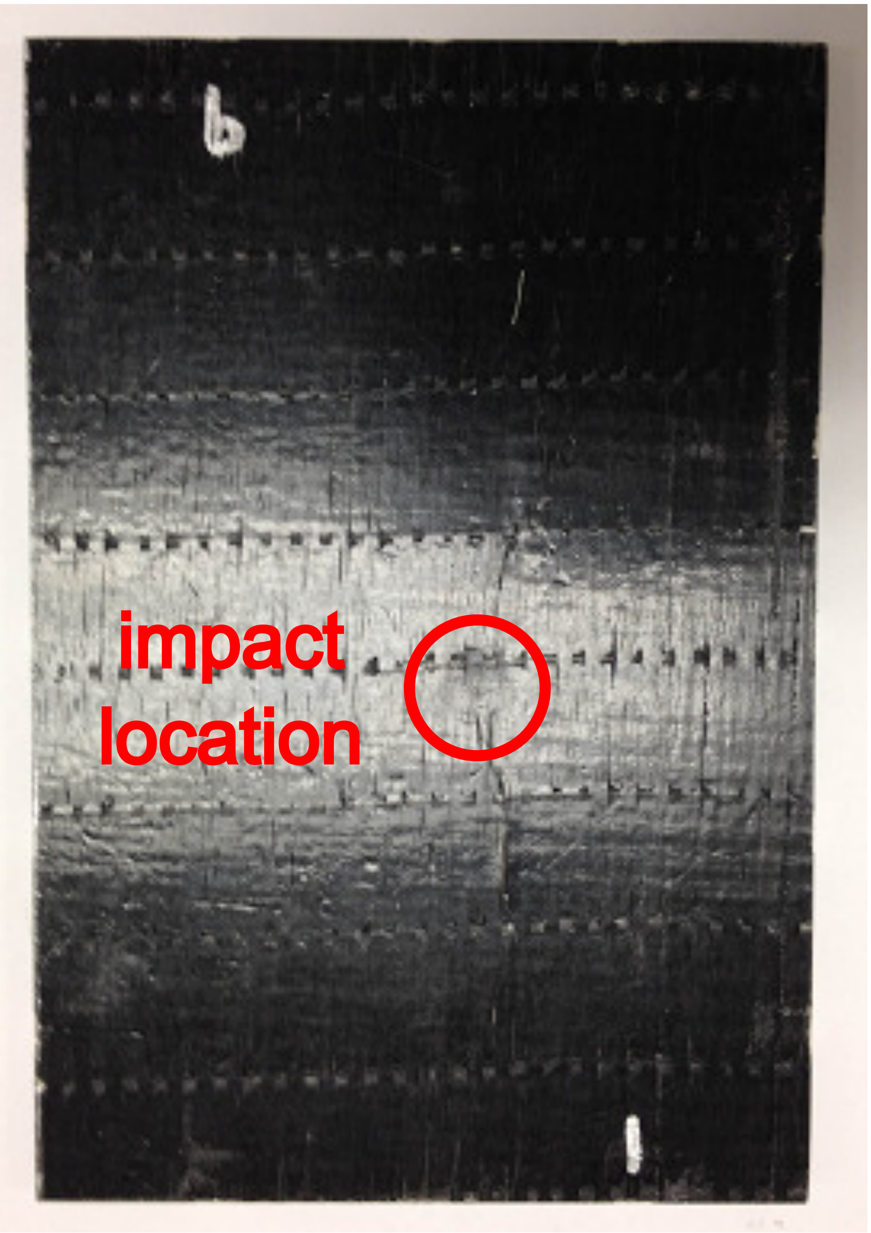

Figure 5.11: Photograph of post-impacted glass fiber/epoxy plate. The plate is impacted slightly off center resulting in a visible indentation and crack.

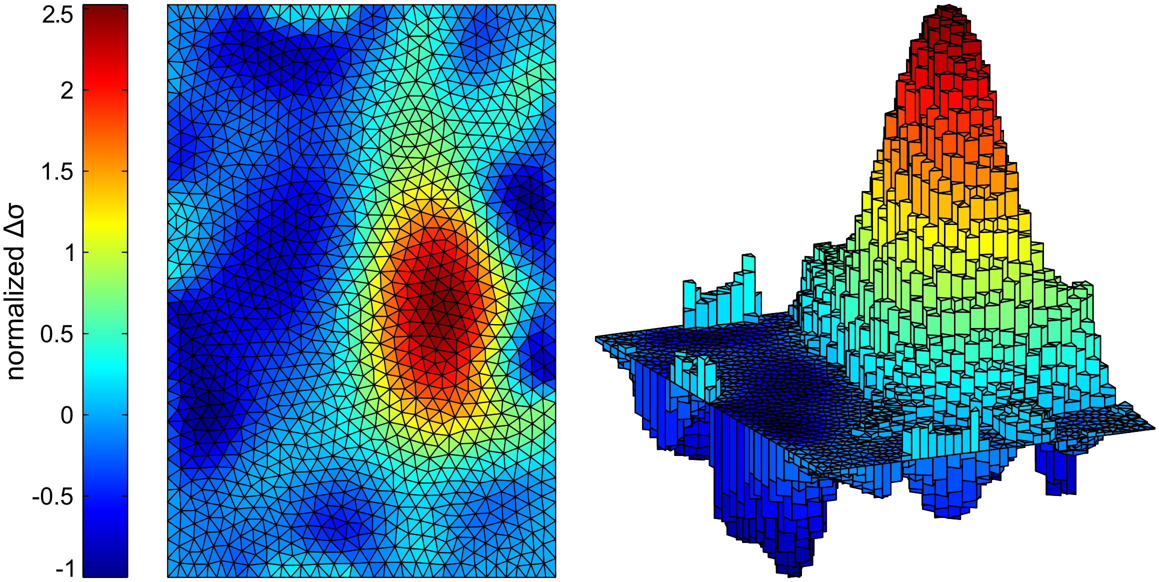

Figure 5.12: EIT image of impact damage detection. Good correlation between the reconstruction peak and the impact location is observed. A conductivity artifact running the length of the plate and originating at the impact location indicates that the crack damage was captured as well.

5.4 Carbon Nanofiber/Polyurethane

5.4.1 Carbon Nanofiber/Polyurethane Manufacturing

CNF/PU specimens are produced using ReoFlex 20 PU from Smooth-On (Easton, PA) and Pyrograf III-PR-24-XT-HHT CNFs from Applied Sciences (Cedarville, OH). The manufacturer's data states that the PU has a Shore hardness of approximately 20A and a tensile modulus of approximately 190 MPa at 100% strain. Measured amounts of PU and CNFs are combined to produce specimens at 7.5, 10.5, 12.5, and 15% filler volume fraction. CNFs and PU are first hand-mixed in a cup to form a dough-like material. This mixture is then placed into a 2-roll mill and shear-mixed. Specimens containing 10.5, 12.5, and 15% CNF filler are shear-mixed for 5 minutes while the specimen containing 7.5% CNF is shear-mixed for 20 minutes in order to obtain good dispersion and similar CNF aspect ratio. Immediately after mixing, the material is spread evenly into an open, rectangular silicone mold measuring 25.4 mm × 76.2 mm × 2.5 mm. A flat cover is then put onto the top of the mold and the material is cured at room temperature for at least 16 hours. Lastly, the material is post-cured for an additional 6 hours at 65 °C to stabilize the mechanical properties of the PU. Portions for scanning electron microscope (SEM) imaging, tensile testing, and EIT imaging are cut from the as-molded specimens using a razor.

The dispersion of CNFs is qualitatively assessed via SEM imaging as shown in Figure 5.13. Additional noteworthy SEM images can be seen in Figures 5.14, 5.15, and 5.16. SEM imaging is performed via a Hitachi SU8000 In-Line SEM in the Lurie Nanofabrication Facility (LNF) at the University of Michigan. CNF/PU specimens are immersed in liquid nitrogen for approximately 10 minutes and then fractured in order to obtain a good surface for imaging.

The CNF/PU nanocomposites were manufactured by Dr. Sila Gungor at the Pennsylvania State University as part of a collaborative project. The manufacturing methods described represent her work but are included for completeness.

5.4.2 Tensile Testing

5.4.2.1 Experimental Setup

Tests of the CNF/PU nanocomposites are performed in order to assess the influence of filler volume fraction and viscoelasticity on piezoresistive response when bonded to a much stiffer substrate undergoing mechanical loading. These tests are important because there is a growing interest in using nanocomposites as discrete strain sensors with higher gauge factors than traditional strain gauges [7] [101]. In strain sensor applications, nanocomposites will necessarily be bonded to much stiffer substrates. Furthermore, this testing gives some insight into the sensitivity of each filler volume fraction and a more controlled look at the influence of viscoelasticity on piezoresistive response.

Thin strips of the CNF/PU specimens measuring 25.4 mm $\times$ 6.35 mm $\times$ 2.5 mm are completely bonded on one side onto polyvinyl chloride (PVC) bars and loaded into a MTS-810 load frame as shown in Figure 5.17 and strained at 0.1 mm/s. Two loading regimens are considered. In the first, the PVC bar is subjected to linearly increasing tension, sinusoidal variation between tension and compression, and finally linearly decreasing compression. The second load regimen applies and holds constant tension intermittently. Longitudinal strain is measured via a strain gauge bonded to the back surface of the PVC bars. Colloidal silver paste electrodes are applied such that the resistance of the CNF/PU can be measured along the 25.4 mm dimension via an Agilent 34401A digital multimeter. The longitudinal strain induced by both load regimens and the nanocomposite piezoresistive responses can be seen in Figure 5.18.

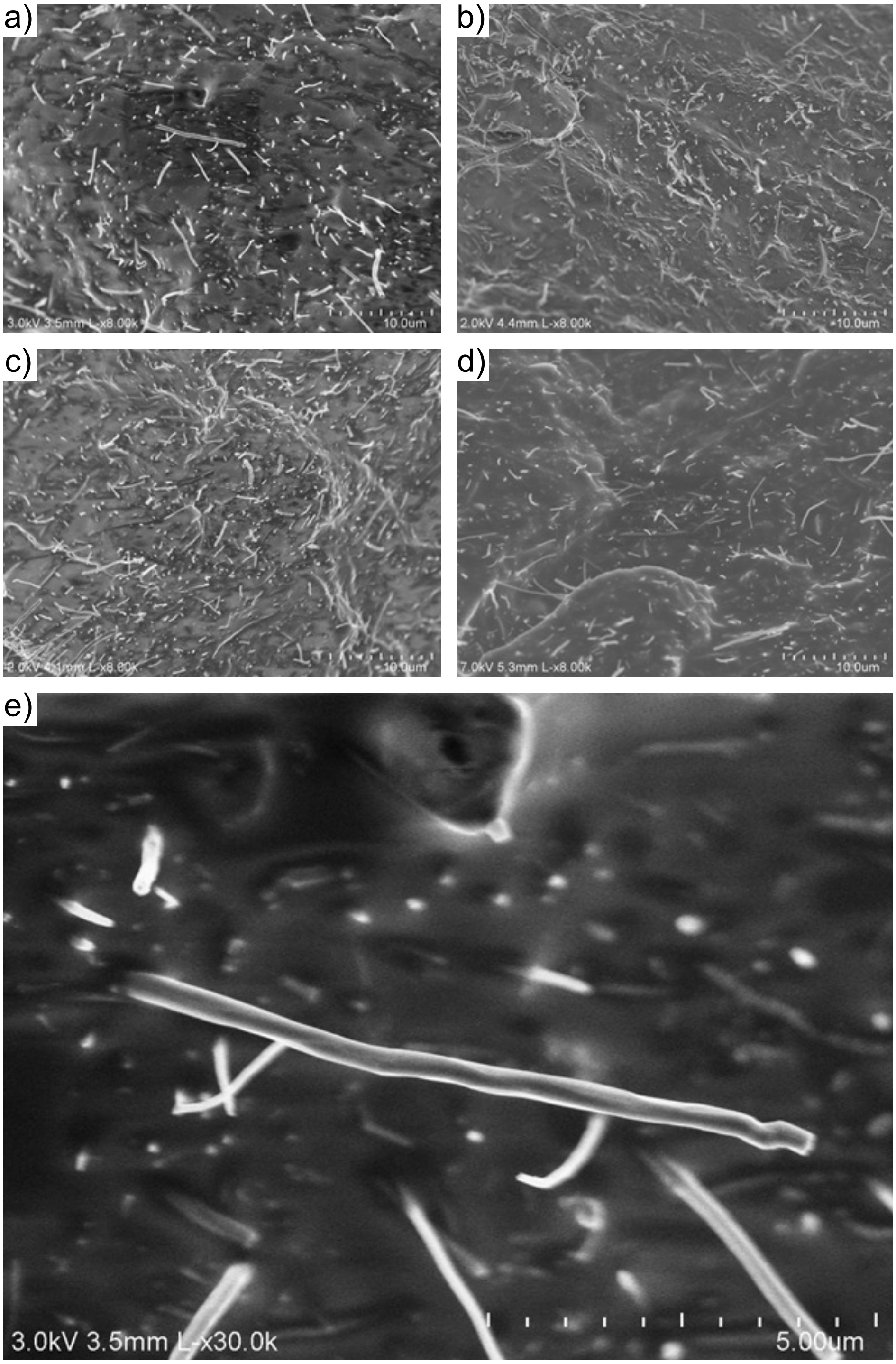

Figure 5.13: SEM images of CNF distribution at a) 7.5% filler volume fraction. b) 10.5% filler volume fraction. c) 12.5% filler volume fraction. d) 15% filler volume fraction. e) Close up of a single CNF within the 7.5% filler volume fraction sample.

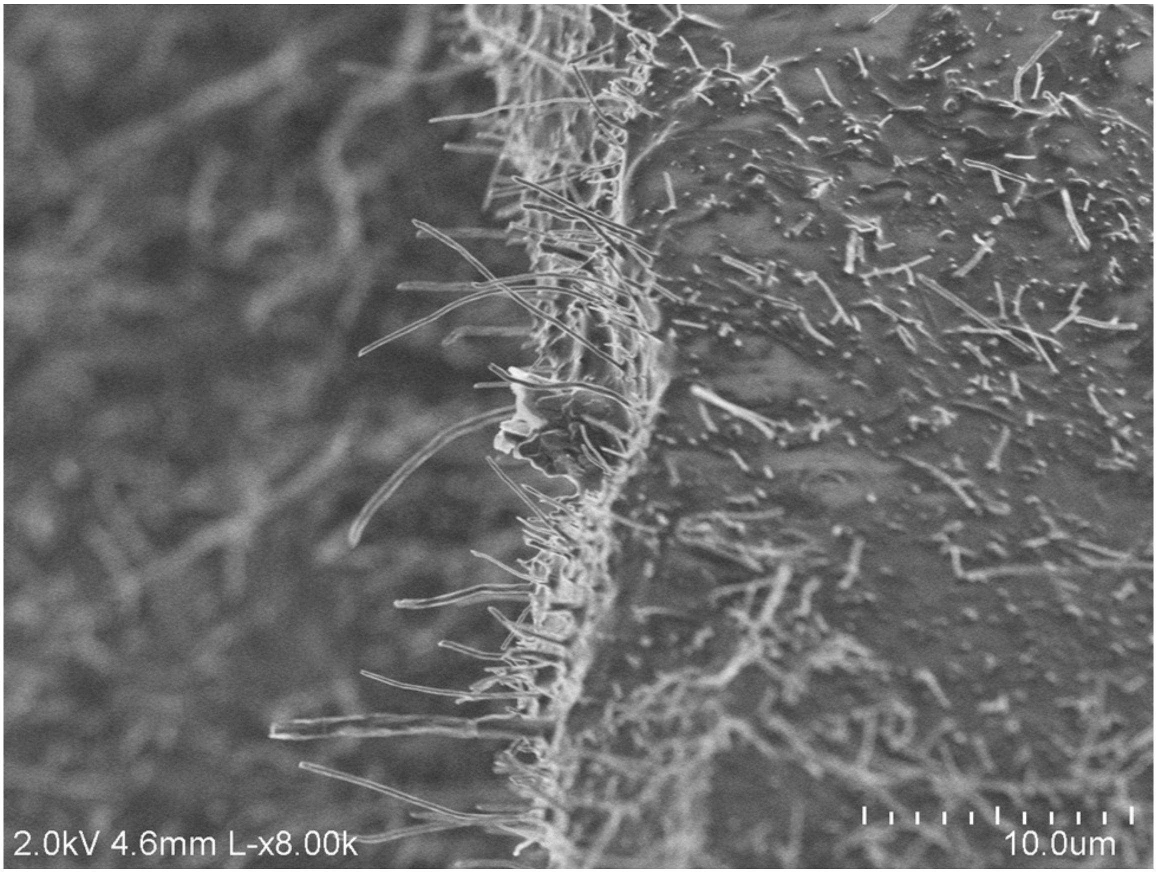

Figure 5.14: Fracture surface of 12.5% filler volume fraction CNF/PU.

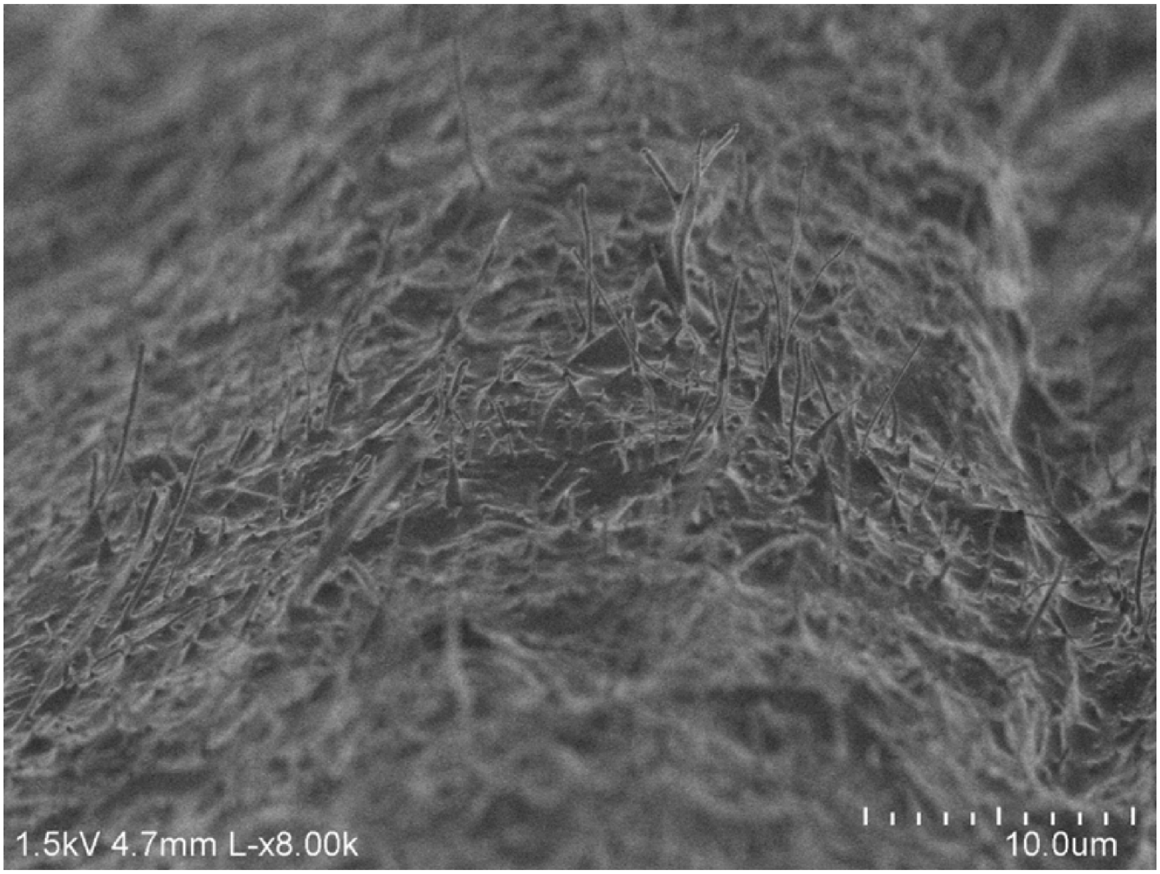

Figure 5.15: CNFs sticking out of a fracture surface at 15% filler volume fraction.

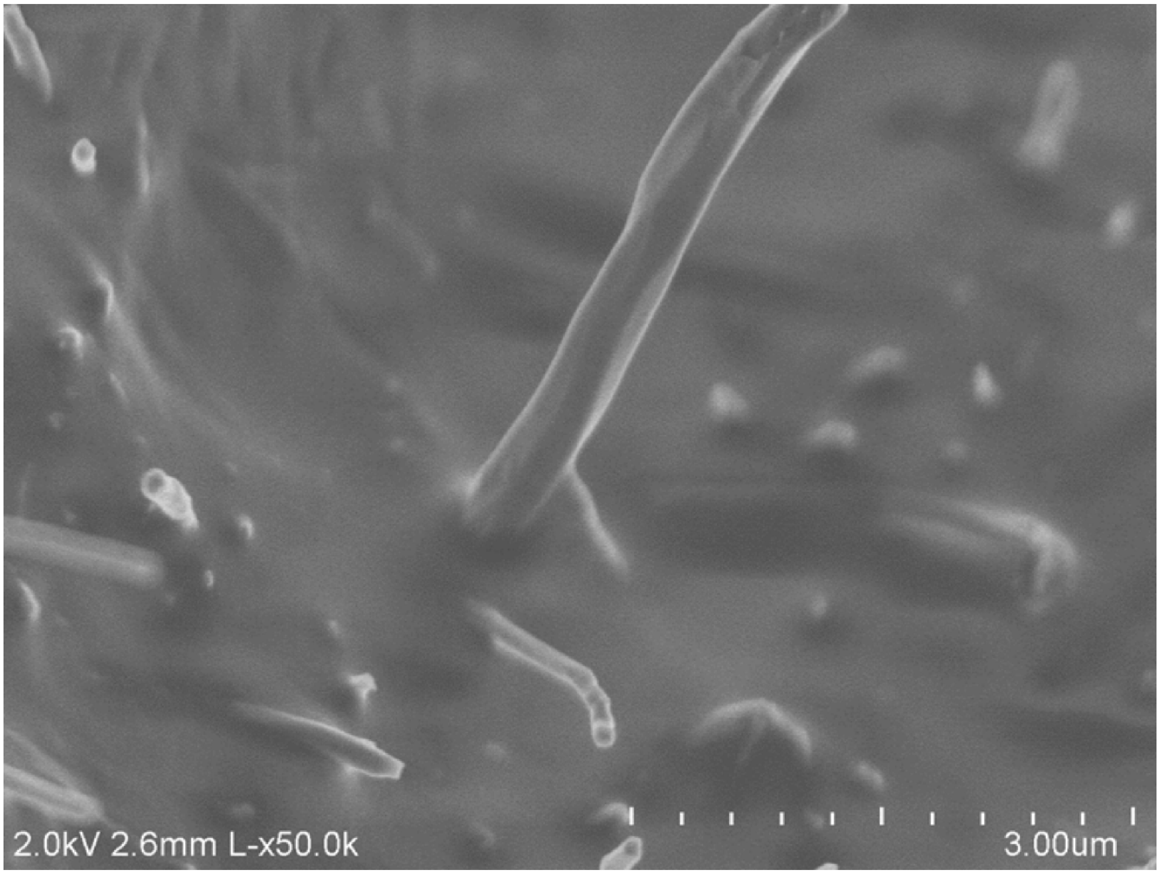

Figure 5.16: Close up of a CNF protruding from the PU at 15% filler volume fraction.

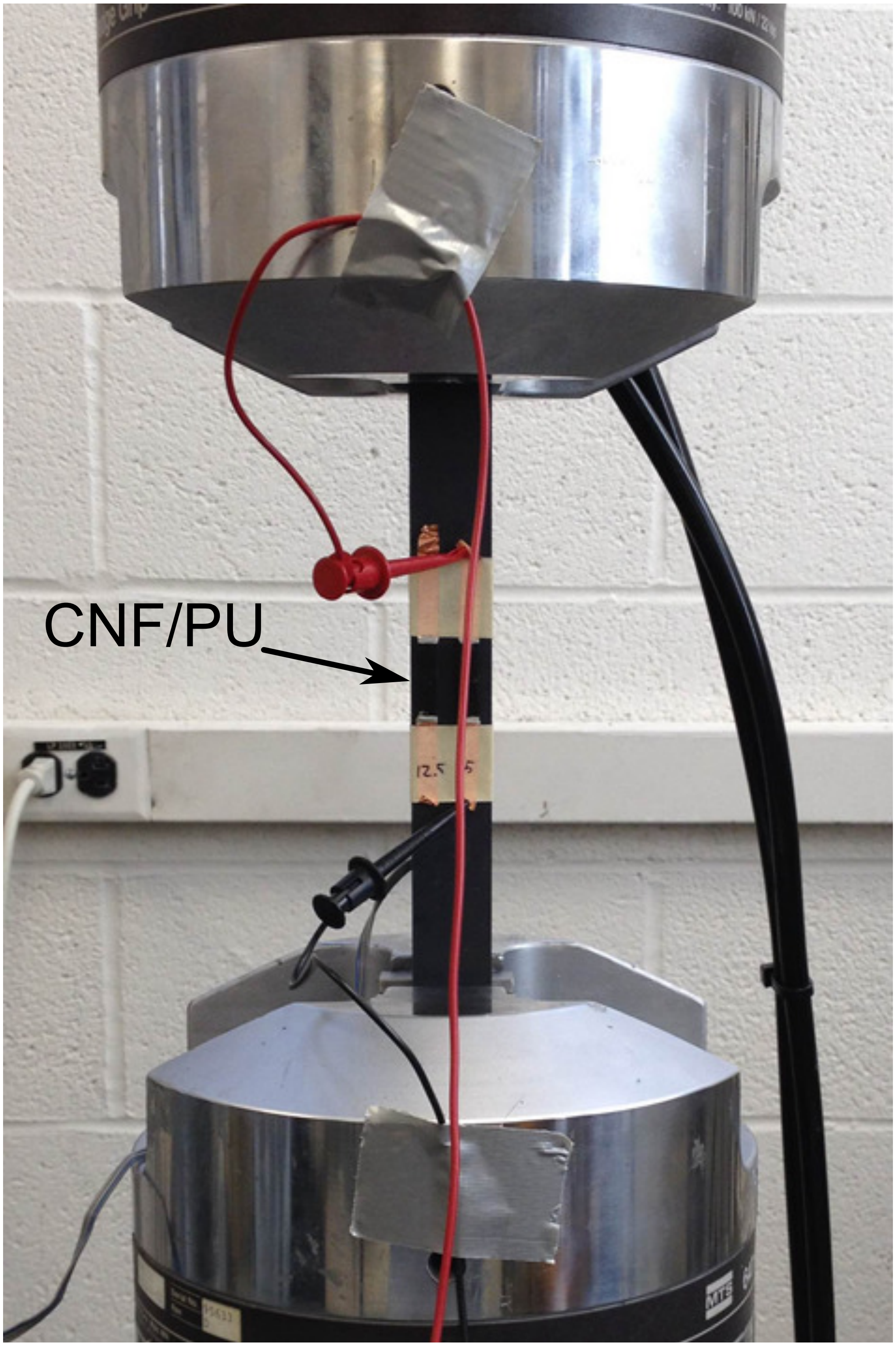

Figure 5.17: CNF/PU bonded to a PVC bar and loaded in MTS-810 load frame.

5.4.2.2 Piezoresistive Response

Consider first the results for the sinusoidally varying strains shown in Figure 5.18. For positive tensile strain, the 7.5% filler volume fraction material first shows a positive piezoresistive response. That is, resistance increases with increasing tension. As the strain cycle goes into compression the material exhibits negative piezoresistivity such that resistance again increases with increasing compression. A similar albeit muted trend is observed for 10.5%. These results also resemble observations by Dubey et al. [125]. However, at 12.5 and 15% filler volume fraction the piezoresistive response of the material changes markedly to the point of appearing out of phase with the strain. While a complete analysis of the nature of negative piezoresistivity exceeds the scope of this study, Cattin and Hubert [78] and Toprakci et al. [126] provide excellent insight into the topic and interested readers are directed to their preceding citations. It is apparent, however, that the dominant mechanism of piezoresistivity in CNF/PU is volume fraction-dependent and changes markedly between 10.5 and 12.5% filler volume fraction.

Now consider the right-most column of Figure 5.18 wherein the PVC bars are put in tension, held, and then released for several cycles. All volume fractions respond immediately to the sudden application of tensile strain. However, the most dramatic change in resistance occurs either with the application of tension to the PVC bar or the release of tension with decay occurring between due to the viscoelastic response of the PU. The influence of a suddenly released load dominates the response for 12.5 and 15% filler volume fraction again suggesting a volume fraction-dependent dominant mechanism of piezoresistivity. Interested readers are directed to Dubey et al. [125] for a discussion on the influence of strain rate on piezoresistive response. It is also important to note that because of shear lag in the viscoelastic CNF/PU strip, determination of the strain state of the CNF/PU is not trivial. It is stress free on all sides except where bonded, and the traction on the bonded side is dictated by the response of the PVC bar which, for regions sufficiently removed from the grips, is in a state of pure uniaxial stress. It is worth reiterating, however, that highly compliant nanocomposite transducers bonded to structures for strain sensing will encounter a similar situation. It is therefore important to conduct tests as herein presented before employing such nanocomposites as discrete, strain-sensing transducers.

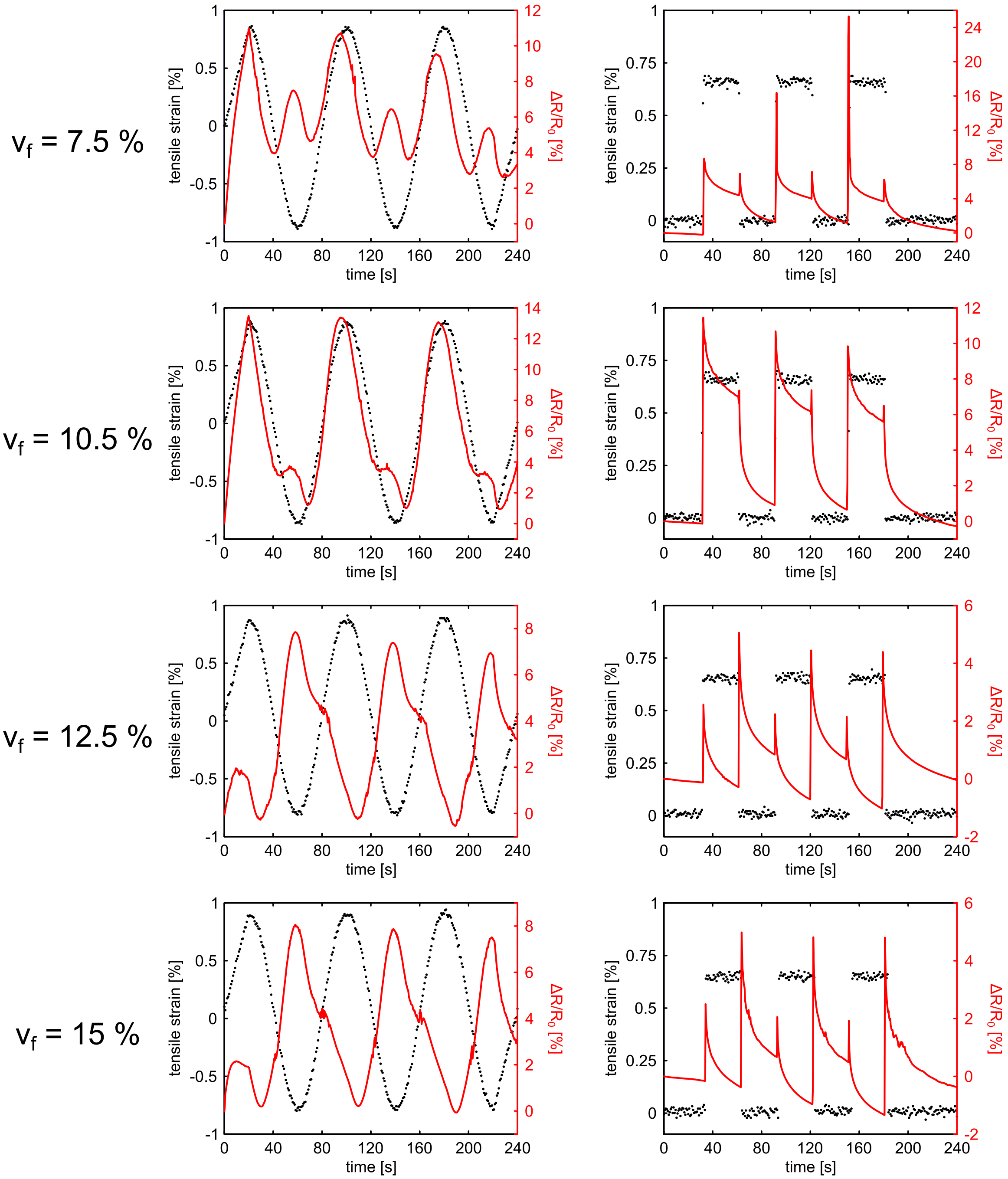

Figure 5.18: Percent change in CNF/PU resistance during tensile loading at 7.5, 10.5, 12.5, and 15% filler volume fraction. The left column shows the response to linearly increasing tension, sinusoidally varying tension and compression, and, lastly, linearly decreasing compression. The right column shows the response to cyclically applied and held tension. Both loading cases show a marked difference in CNF/PU response from 10.5 to 12.5% indicating a volume fraction-dependent change in the dominant piezoresistive mechanism.

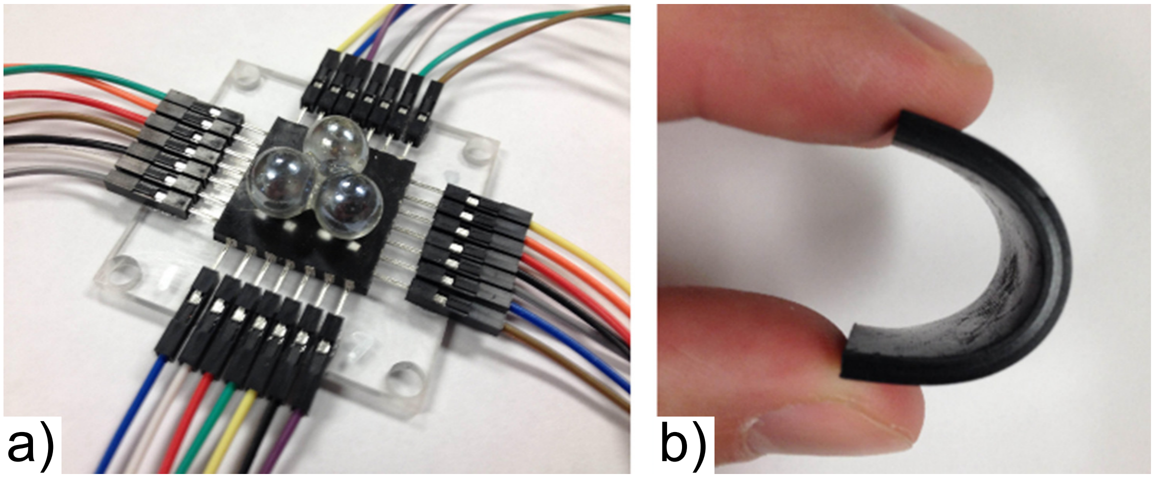

Figure 5.19: a) EIT set up with marble indenters atop the CNF/PU nanocomposite. Electrodes made of patches of colloidal silver paste can be seen on the edges of the composite. b) Demonstration of the flexibility of the CNF/PU nanocomposite. The material is easily deformed and recovers to its original state.

5.4.3 Distributed Strain Sensing

5.4.3.1 Experimental Setup

Electrodes are attached to the CNF/PU composites by first applying seven evenly spaced 1.59 mm patches of colloidal silver paste per side as shown in Figure 5.19. The paste is allowed to dry for at least one hour before jumper wires are pushed lightly into the patches and then glued to an acrylic base. An additional drop of silver paste is then applied where the jumper wire touches the originally applied patch to ensure good electrical contact. A Keithley 6221 current source is used to supply 2.5 mA DC injections between electrodes. Voltages are measured using two 16-channel National Instruments 6368-PXIe data acquisition cards for 10 s at 128 Hz. Data is collected via an in-house LabView code and smoothed using a moving average of half-width 256.

Distributed strain is induced in 25.4 mm $\times$ 25.4 mm CNF/PU samples by resting a 1.2 kg mass atop three bonded glass marbles as shown in Figure 5.19. Spherical glass marbles are used because they are non-conductive and their curvature does not cut into the soft CNF/PU. Three marbles are used to demonstrate the ability of EIT to clearly differentiate between multiple points of contact. In light of the viscoelastic effects observed during tensile testing, the mass is allowed to rest atop the CNF/PU samples for an hour before using a 28-electrode system to image strain-induced conductivity changes.

5.4.3.2 Strain Field Imaging

As shown in Figure 5.20, EIT accurately captures three distinct points of contact due to the spherical indenters for each volume fraction. Larger changes in conductivity are observed for lower volume fractions implying that they are more sensitive to the imposed strain fields. However, the EIT image produced for 7.5% filler volume fraction has a region in which the conductivity change is markedly larger. This is speculated to be due to non-uniform nanofiller dispersion and a region of lower nanofiller density in the vicinity of the region in question. Conversely, as the filler volume fraction increases, such deviations are less pronounced. Contrasting the results shown in Figure 5.20 with the results shown in Figure 5.18, it can be inferred that the type of loading markedly influences the piezoresistive response of CNF/PU. That is, conductivity increases are seen for all filler volume fractions through EIT imaging wherein Hertzian contact-like strains are induced. The CNF/PU, however, displays greatly varying negative piezoresistivity when bonded to a stiffer substrate in dynamic sinusoidal loading. Conductivity increases in the region of the distributed load indicating that the nanofillers are becoming closer together thereby decreasing the tunneling resistance felt by electrons. Additionally, the compression increases the density of the nanofiller network thereby increasing the number of viable tunneling junctions. These factors seemingly dominate the response resulting in a net increase in conductivity.

5.5 Summary and Conclusions

EIT was investigated as a health monitoring technique for damage and strain detection in CNF/epoxy, glass fiber/epoxy laminates with CB filler, and CNF/PU. EIT was able to adeptly locate through-holes in both CNF/epoxy and glass fiber epoxy laminates with CB filler, and a lower detectability limit of 3.18 mm by EIT was experimentally determined. Impact damage was also successfully located in a glass fiber/epoxy laminate.

SEM imaging indicated that uniform nanofiller dispersion was achieved during CNF/PU manufacturing. Tests of the CNF/PU nanocomposite material bonded to a mechanically deformed substrate revealed that the piezoresistive response depends strongly on the nanofiller volume fraction. Distributed strain sensing via EIT, however, resulted in much more consistent results. Three distinct points of contact were imaged via EIT, and sensitivity increased with decreasing filler volume fraction. The relative ease and low cost of CNF/PU manufacturing combined with these results demonstrate the considerable potential of CNF/PU and EIT for tactile imaging and distributed strain sensing.

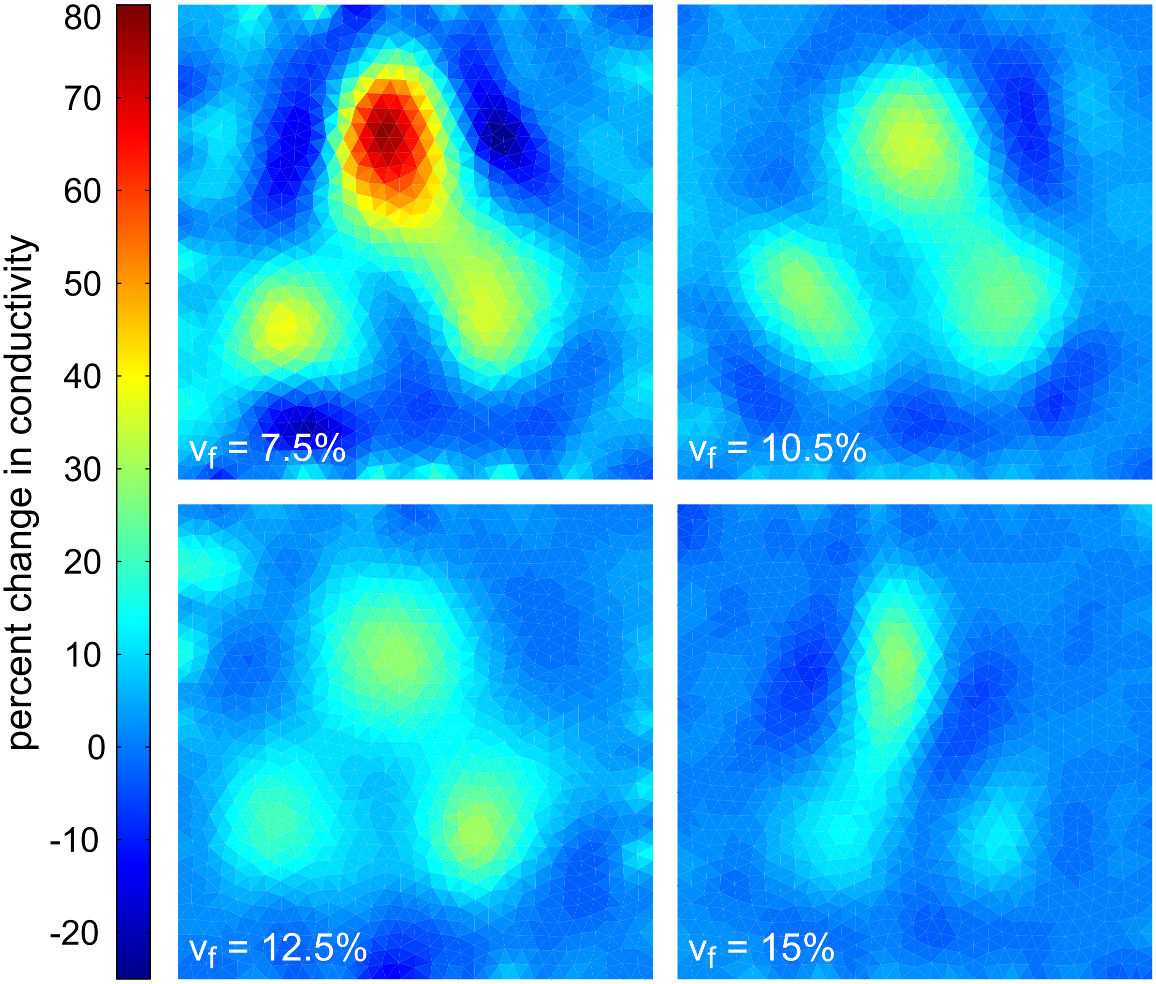

Figure 5.20: EIT images of percent change in conductivity due to distributed straining. EIT clearly captures three distinct points of contact, and larger increases in conductivity are observed for lower volume fractions.

Based on these results, it is believed that conductivity-based health monitoring via EIT has considerable potential. Unlike sensing layer approaches, the nanocomposite matrix approach ensures the entire composite is self-sensing. EIT is also able to accurately locate both through-hole damage and impact damage with only 16 electrodes. This is a considerable improvement over the two-dimensional resistance change methods summarized in the literature review.

CHAPTER 6

Methods for Electrical Impedance Tomography Enhancement

6.1 Introduction

Chapter 5 has established that EIT has considerable potential for damage and strain identification in nanocomposite matrices, and Chapter 4 has elucidated some unique properties of nanocomposites. These two efforts are now brought together to enhance EIT for conductivity-based SHM. First, the electrical anisotropy induced by nanofiller alignment is leveraged to enhance sensitivity to delaminations. This is a novel, microscale approach to enhancing the sensitivity. That is, how nanofillers can be manipulated on microscales through varying degrees of alignment and at various orientations to enhance structural-scale sensitivity to delamination is studied. It is important to acknowledge that achieving the nanofiller tailoring herein described in structural composites remains a challenge, and while this investigation is motivated by delaminations in laminated composites, the forthcoming analysis does not explicitly model the reinforcing structural fibers. Rather, conductivity values are obtained based on the nanocomposite resistor network model developed in Chapter 4, and it is assumed the structural composite has those bulk conductivities. The manufacturing challenge therefore becomes achieving high degrees of nanofiller fidelity in the presence of structural fibers. Nonetheless, this approach shows promise of being a powerful method of enhancing delamination detection.

Second, a method of significantly enhancing the resolution of EIT or, synonymously, decreasing the number of electrodes required to produce quality images is presented. The novel insight to this approach is to specifically address the rank-deficiency of the inverse problem by introducing additional constraints. Although presented as a general mathematical approach and applicable to any system wherein the conductivity can be changed in a known manner, this approach is specifically motivated by piezoresistive nanocomposites.

Multi-physics approaches to overcoming the limitations of EIT have been proposed such as magnetic resonance EIT (MR-EIT) [127] [128] and coupling the EIT reconstruction with localized conductivity changes induced by elastic deformation (sometimes referred to as impediography) [129] [130]. These approaches, though insightful and capable of producing high-quality images, impose upon some of EITs most valuable features – low cost and portability. MR-EIT requires magnetic resonance imaging (MRI) systems, and impediography requires a method of inducing localized conductivity changes such as acoustic arrays or highly engineered meta-materials capable of vibration localization. It is therefore desirable to develop a method of EIT enhancement that does not come at the expense of its other attributes. As opposed to inducing highly localized elastic deformations as in impediography to enhance EIT [129], global conductivity changes have the potential to be integrated without ancillary equipment. In aerospace venues, for example, routine pressurization of the cabin or the added weight of fueling will cause predictable, global strain fields. In a carefully engineered nanocomposite material, the global conductivity changes induced by these strain fields could also be known and therefore easily integrated into an EIT routine for greatly bolstered damage identification.

6.2 Delamination Sensitivity Enhancement through Nanofiller Alignment

6.2.1 The Influence of Anisotropic Conductivity on Boundary Voltage

Care was taken in the description of the nanofiller alignment simulations in Chapter 4 to distinguish the micro or $(\tilde{x}, \tilde{y}, \tilde{z})$ domain. This distinction is important because different orientations of the microscale domain are next considered in the EIT domain. To clarify, alignment refers to fillers being more disposed to run parallel to each other while orientation refers to the direction in which fillers are aligned. The EIT domain is defined within the (x, y, z) basis. In this basis, the structure of interest is a thin plate measuring 10 cm × 10 cm × 3 mm. The x and y-directions span the plate while the z-direction is through the thickness of the plate. Assuming the thin plate has conductive properties determined by the microscale nanofiller alignment analysis, the conductivity in the EIT domain can be expressed using standard tensor rotation rules, $\sigma_{ij} = R(\alpha, \beta, \gamma)_{ki} \tilde{\sigma}_{kl} R(\alpha, \beta, \gamma)_{lj}$. Here, R_{ij} is the rotation tensor formed from the Euler angles α, β, and γ. More explicitly, α is the first rotation of the $(\tilde{x}, \tilde{y}, \tilde{z})$ basis about the z-axis. The second rotation of the $(\tilde{x}, \tilde{y}, \tilde{z})$ basis is by β about the $\tilde{x}$-axis, and the last rotation of the $(\tilde{x}, \tilde{y}, \tilde{z})$ basis is about the $\tilde{z}$-axis by γ. For a prescribed degree of alignment, fillers are equally disposed run in either the $\tilde{x}$

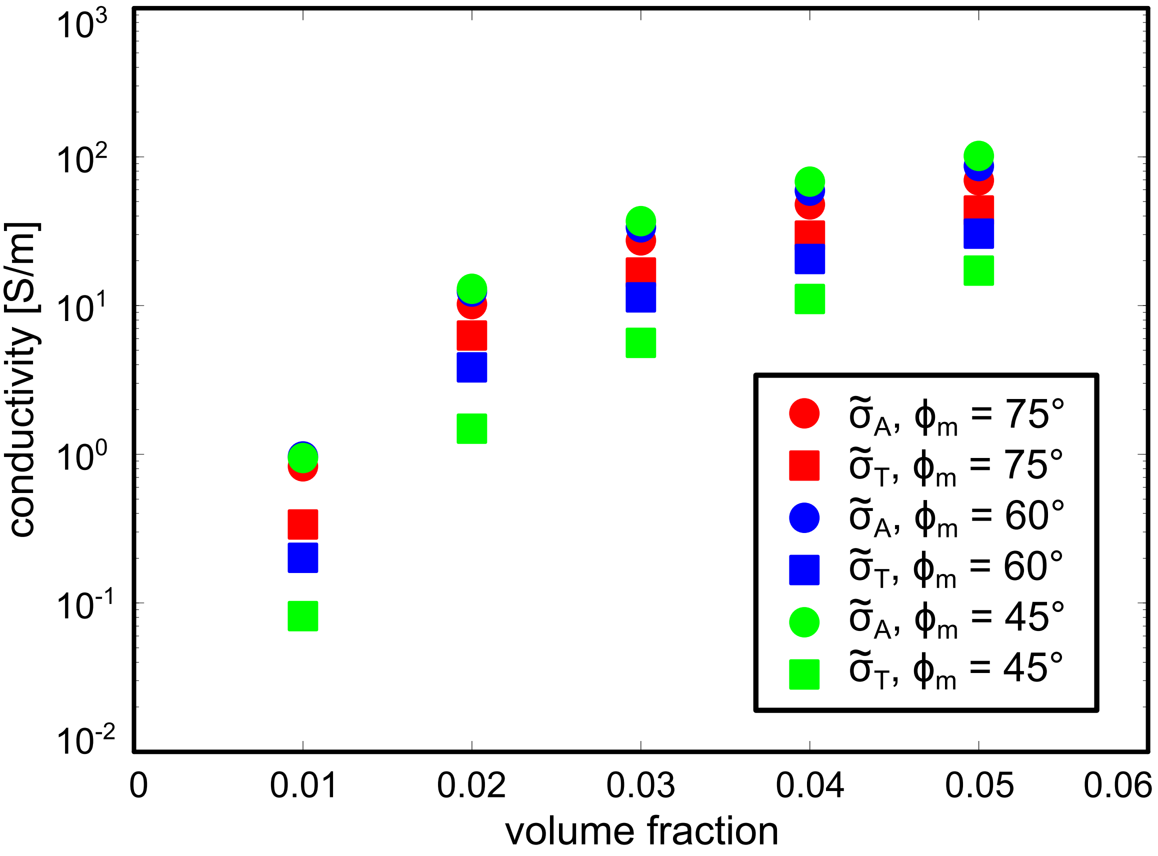

Figure 6.1: Conductivity versus volume fraction in the transverse and alignment directions for three different degrees of alignment..

or $\tilde{y}$-direcion. Because of this, conductivity in the micro-domain is transversely isotropic and the choice of γ is inconsequential. Allowing for different orientations of the micro-domain in the EIT domain is akin to the fillers to be aligned at an angle with respect to the through-thickness direction of a plate. Three degrees of nanofiller alignment are selected for the sensitivity enhancement analysis as shown in Figure 6.1. Because the conductivity is calculated in the microscale domain, $\tilde{\boldsymbol{\sigma}}$ is a diagonal matrix with $\tilde{\sigma}_{11} = \tilde{\sigma}_{22} = \tilde{\sigma}_T$ where $\tilde{\sigma}_T$ is the conductivity transverse to the alignment direction and $\tilde{\sigma}_{33} = \tilde{\sigma}_A$ where where $\tilde{\sigma}_A$ is the conductivity in the nanofiller aligment direction. $\tilde{\sigma}_{ij} = 0$ for $i \neq j$.

Delaminations to be detected by EIT are simulated as thin voids in a reference mesh. The voids are formed by the intersection of two slightly overlapping spheres thereby ensuring a zero-thickness edge as is expected from a real delamination. Delaminations are centered through the plate thickness and located in the plane as shown in Figure 6.2. Two cases are considered. The first case considers a single delamination with a diameter of 1.7 cm and a maximum opening of 0.12 mm. The second case considers a second delamination with a diameter of 1.2 cm and a maximum opening of 0.06 mm in the presence of the original delamination. The sensitivity enhancement analysis begins by examining the influence of filler alignment and orientation on boundary voltage measurements. Because EIT depends on in-plane boundary voltages, it is desirable to tailor the nanocomposite conductivity to enhance boundary voltage changes due to delamination. To this end, for a given damage state and conductivity, the norm of the percent change in boundary voltages due to damage is considered as a function of the Euler angle β. If the aligned conductivity is more sensitive, this norm is expected to increase. The Euler angle α is fixed at 45° for identical conduction in the x and y-directions. As shown in Figure 6.2, both ϕ_m and β have a large influence on the boundary voltage sensitivity. Furthermore, it is observed that the greatest gains are obtained for 1% filler volume fraction. Because the anisotropic ratio is greatest for each value of ϕ_m at 1% filler volume fraction, it can be inferred that higher anisotropic ratios result in greater sensitivities. The symmetry of the curves about $\beta = 90°$ is expected because of the symmetry of the $\tilde{\boldsymbol{\sigma}}$ tensor.

6.2.2 Formulation of the Anisotropic Electrical Impedance Tomography Inverse Problem

The EIT forward problem was presented in general for both isotropic and anisotropic conductivity in Chapter 3. The inverse problem, however, requires more special consideration and will be presented here. In order to proceed, it must first be conceded that a unique solution generally does not exist for anisotropic EIT [131] [132]. Nonetheless, as demonstrated by other researchers [60] [133], a solution can be recovered for mild degrees of anisotropy if it is assumed that the eigenvectors of the conductivity tensor are preserved during the minimization. In light of this assumption, rewrite the conductivity as $\sigma_{ij} = \kappa\sigma_{ij}^0$ and select κ such that $\det(\sigma_{ij}^0 = 1)$ [133]. Immediately discretize κ such that EIT now endeavors to find $\boldsymbol{\kappa}$ to minimize $\|\mathbf{V}_m - \mathbf{F}(\boldsymbol{\kappa}\sigma_{ij}^0)\|^2$. Similar to the isotropic formulation, linearize $\mathbf{F}(\boldsymbol{\kappa}\sigma_{ij}^0)$ by retaining the linear terms of a Taylor series expansion centered about $\boldsymbol{\kappa}_0$ as shown in equation 6.1. This approximation is substituted into the minimization expression resulting in equation 6.2.

$$\mathbf{F}(\boldsymbol{\kappa}\sigma_{ij}^0) \approx \mathbf{F}(\boldsymbol{\kappa}_0\sigma_{ij}^0) + \frac{\partial \mathbf{F}(\boldsymbol{\kappa}_0\sigma_{ij}^0)}{\partial \boldsymbol{\kappa}}(\boldsymbol{\kappa} - \boldsymbol{\kappa}_0) \tag{6.1}$$

$$\mathbf{V}_m - \mathbf{F}(\boldsymbol{\kappa}\sigma_{ij}^0) - \frac{\partial \mathbf{F}(\boldsymbol{\kappa}_0\sigma_{ij}^0)}{\partial \boldsymbol{\kappa}}(\boldsymbol{\kappa} - \boldsymbol{\kappa}_0) = \mathbf{0} \tag{6.2}$$

Substituting $\mathbf{J} = \partial\mathbf{F}(\boldsymbol{\kappa}_0\sigma_{ij}^0)/\partial\boldsymbol{\kappa}$, $\Delta\boldsymbol{\kappa} = \boldsymbol{\kappa} - \boldsymbol{\kappa}_0$, and $\mathbf{V}_e = \mathbf{V}_m - \mathbf{F}(\boldsymbol{\kappa}\sigma_{ij}^0)$, equation 6.2

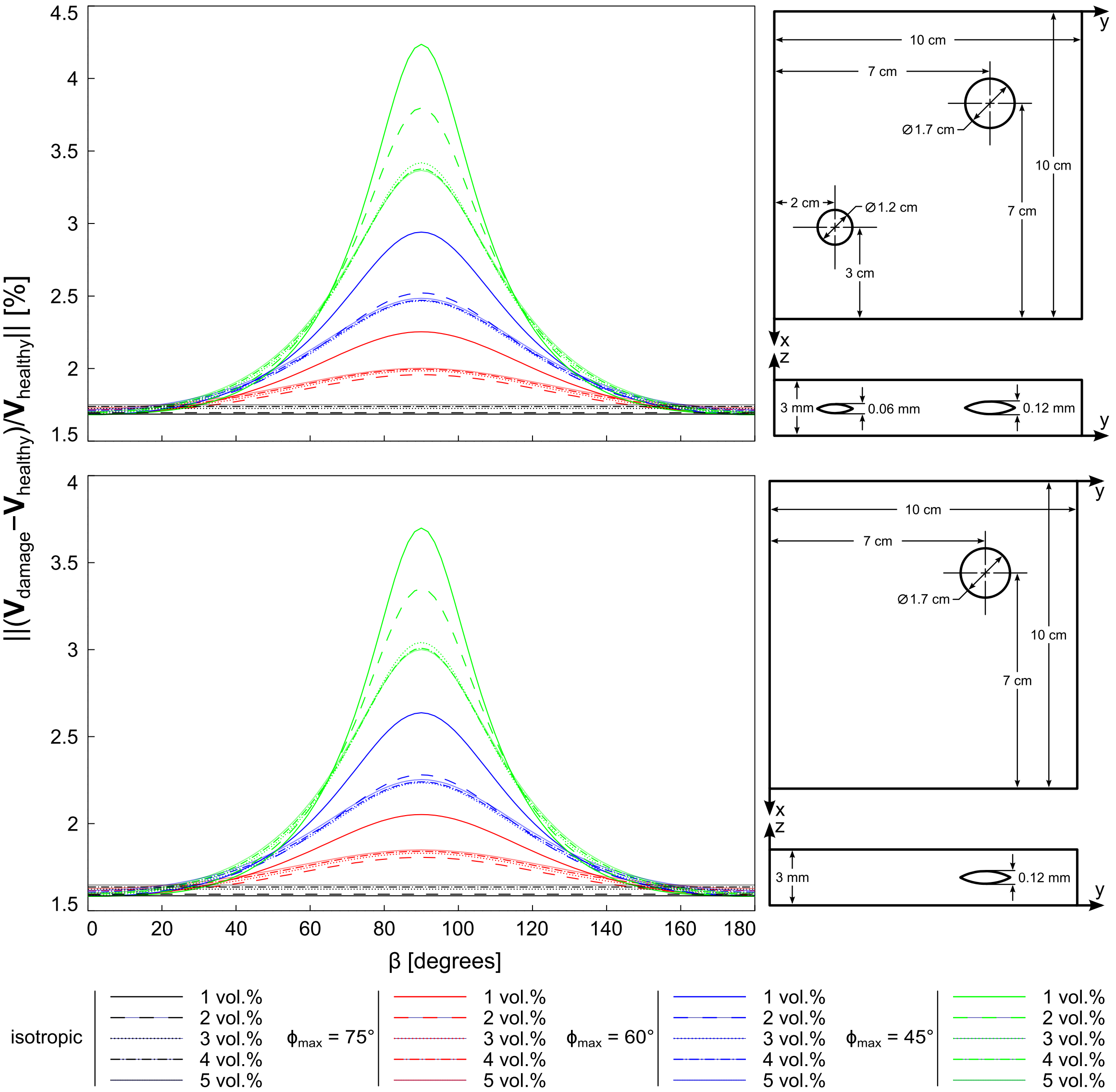

Figure 6.2: Norm of the percent change in boundary voltage due to single and double delamination cases as a function of β for $\phi_m = 45°$, 60°, 75°, and isotropic (90°) conductivities at 1%-5% filler volume fraction. Thickness dimensions in schematic exaggerated for clarity.

can be rewritten as follows.

$$\mathbf{J}\Delta\boldsymbol{\kappa} = \mathbf{V}_e \tag{6.3}$$

The anisotropic sensitivity matrix now takes the form shown in equation 6.4.

$$J_{MN\,e} = -\int_{\Omega_e} \frac{\partial u^M}{\partial x_i}\sigma^0_{ij}\frac{\partial \bar{u}^N}{\partial x_j}\,\mathrm{d}\Omega_e \tag{6.4}$$

Lastly, $\Delta\boldsymbol{\kappa}$ is recovered again via Tikhonov regularization.

$$\Delta\boldsymbol{\kappa} = \left(\mathbf{J}^T\mathbf{J} + \alpha^2\mathbf{L}^T\mathbf{L}\right)^{-1}\mathbf{J}^T\mathbf{V}_e \tag{6.5}$$

This anisotropic formulation simplifies to the isotropic case for $\kappa\sigma^0_{ij} = \kappa\delta_{ij}$. The most important assumption in the preceding was that the eigenvectors of σ^0_{ij} are preserved during minimization. This assumption makes the problem tractable by reducing the possible unknowns per element from six to one. However, anisotropic EIT is not as robust as the isotropic case and prone to diverge for highly anisotropic materials.

6.2.3 Enhanced Delamination Detection through Nanofiller Alignment

The combined effect of anisotropic conductivity induced by filler alignment and EIT for enhanced delamination detection is now presented. Because the greatest gains in Figure 6.2 are seen at 1% filler volume fraction, the analysis is restricted to such for $\beta = 0°$, 30°, 60°, and 90°. Figure 6.3 shows the EIT images for the single delamination case, and Figure 6.4 shows the EIT images for the double delamination case. These figures show that is indeed possible to markedly enhance the sensitivity of EIT to delaminations by microscale nanofiller tailoring. A final example of the enhancement afforded by nanofiller alignment is shown in Figure 6.5 for $\beta = 60°$ and $\phi_m = 45°$ on a more refined mesh with a single delamination.

6.3 Image Enhancement through Incorporation of Known Conductivity Changes

6.3.1 Formulation of the Coupled Inverse Problem

In order to formulate the coupled EIT inverse problem, recall first the standard minimization problem restated below.

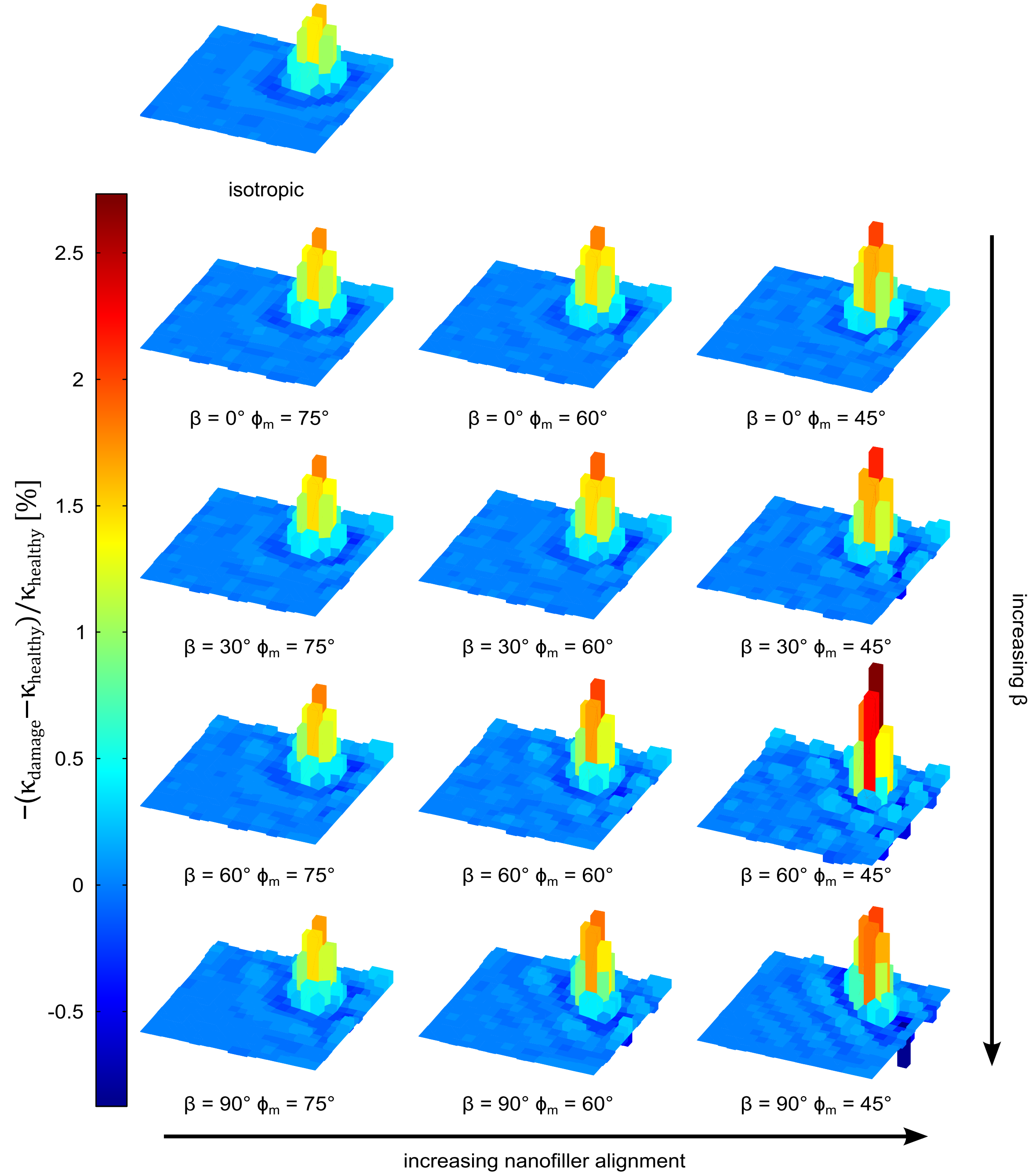

Figure 6.3: Single delamination detection by EIT as a function of β and ϕ_m.

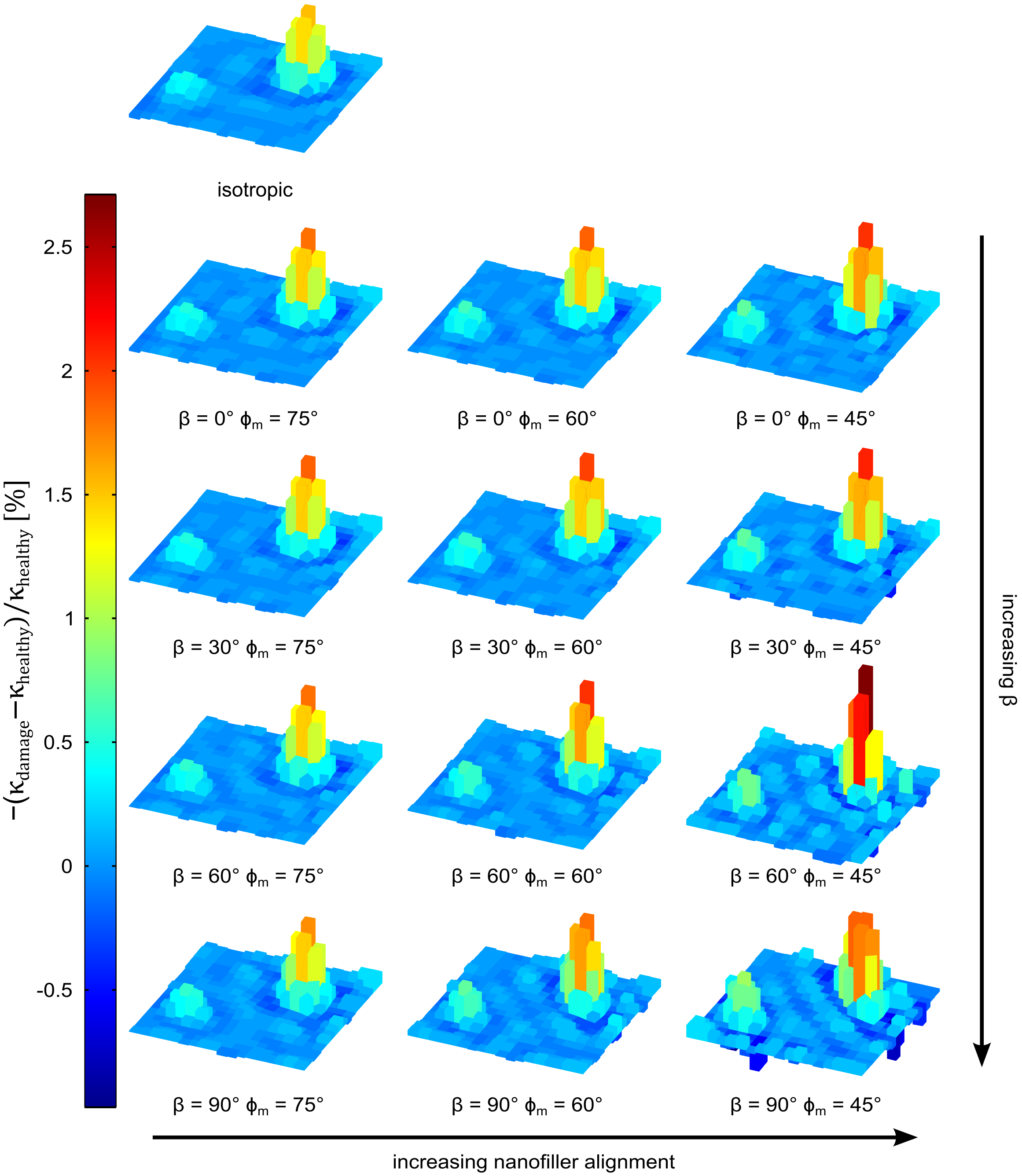

Figure 6.4: Double delamination detection by EIT as a function of β and ϕ_m.

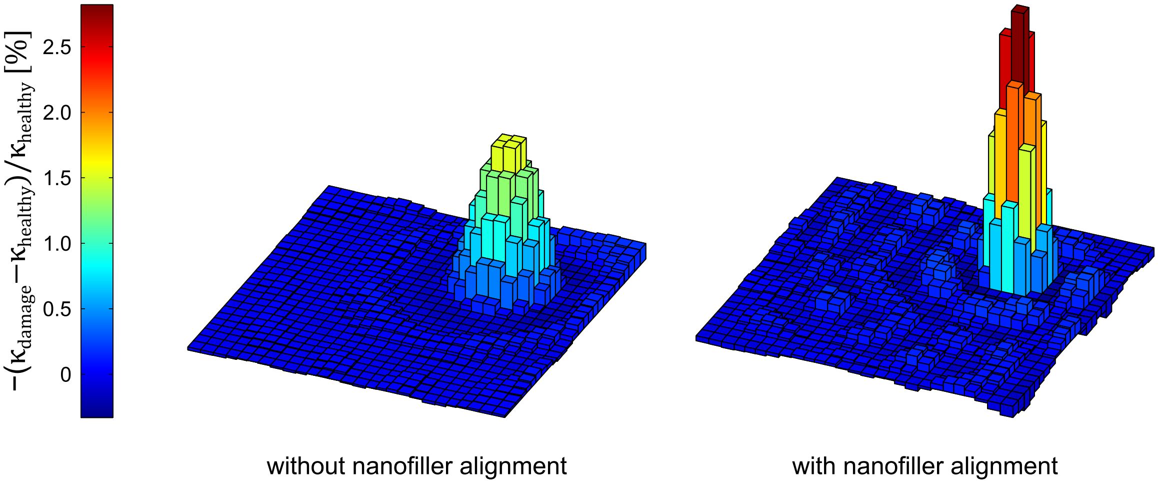

Figure 6.5: Enhanced delamination detection on a more refined mesh with $\beta = 60°$ and $\phi_m = 45°$.

$$\sigma^* = \arg\min_{\sigma} \left(\left\| \mathbf{V}_m - \mathbf{F}(\sigma_0) - \frac{\partial \mathbf{F}(\sigma_0)}{\partial \sigma}(\sigma - \sigma_0) \right\|^2 \right) \tag{6.6}$$

Here, the conductivity distribution has not been boldfaced to indicate discretization by finite elements so that a more general formulation may be considered. Now consider imposing a strain field resulting in a piezoresistive conductivity change on the domain being imaged. As established by the development of an analytical piezoresistivity model in Chapter 4, it can be assumed that there is a known relationship between the unstrained conductivity distribution and the strained conductivity distribution as shown in equation 6.7 where $\bar{\sigma}$ is the strained conductivity.

$$\bar{\sigma} = G(\sigma) \tag{6.7}$$

In the strained state, EIT measurements can again be collected and a new inverse problem formed to find the conductivity distribution, $\bar{\sigma}^*$, that satisfies the minimization shown in equation 6.8.

$$\bar{\sigma}^* = \arg\min_{\bar{\sigma}} \left(\left\| \bar{\mathbf{V}}_m - \mathbf{F}(\bar{\sigma}_0) - \frac{\partial \mathbf{F}(\bar{\sigma}_0)}{\partial \bar{\sigma}}(\bar{\sigma} - \bar{\sigma}_0) \right\|^2 \right) \tag{6.8}$$

Here, $\bar{\mathbf{V}}_m$ is the vector of experimentally collected voltages in the strained state. Equation 6.7 can now be substituted into equation 6.8 resulting in equation 6.9.

$$G(\sigma^*) = \arg\min_{\sigma} \left(\left\| \bar{\mathbf{V}}_m - \mathbf{F}(G(\sigma_0)) - \frac{\partial \mathbf{F}(G(\sigma_0))}{\partial G(\sigma)} (G(\sigma) - G(\sigma_0)) \right\|^2 \right) \tag{6.9}$$

It has herein implicitly been assumed that by knowing G, the initial conductivity estimate σ_0 becomes $G(\sigma_0)$ in the changed stated. Furthermore, assuming G is invertible, the conductivity distribution satisfying the minimization in equation 6.8 can be recovered from $\bar{\sigma}^*$ as $\sigma^* = G^{-1}(\bar{\sigma}^*)$. Appealing to the intuition afforded by piezoresistive nanocomposites, the invertible assumption is akin to a nanocomposite undergoing conductivity change for some prescribed strain and then recovering to the original unstrained conductivity. This effectively adds more constraints to the conductivity distributions which acceptably fit the voltage measurements.

6.3.2 Conductivity Recovery through Discretization

To make practical use of the previously described coupling process, the domain must be discretized by the finite element method described in Chapter 3. In light of this discretization process, it is possible to revisit the minimization and arrive at an explicit solution for the conductivity distribution. Begin by recasting equation 6.6 and equation 6.9 in light of the finite element discretization.

$$\boldsymbol{\sigma}^* = \arg\min_{\boldsymbol{\sigma}} \left(\left\| \mathbf{V}_m - \mathbf{F}(\boldsymbol{\sigma}_0) - \frac{\partial \mathbf{F}(\boldsymbol{\sigma}_0)}{\partial \boldsymbol{\sigma}} (\boldsymbol{\sigma} - \boldsymbol{\sigma}_0) \right\|^2 \right) \tag{6.10}$$

$$\mathbf{G}\boldsymbol{\sigma}^* = \arg\min_{\boldsymbol{\sigma}} \left(\left\| \bar{\mathbf{V}}_m - \mathbf{F}(\mathbf{G}\boldsymbol{\sigma}_0) - \frac{\partial \mathbf{F}(\mathbf{G}\boldsymbol{\sigma}_0)}{\partial \mathbf{G}\boldsymbol{\sigma}} (\mathbf{G}\boldsymbol{\sigma} - \mathbf{G}\boldsymbol{\sigma_0}) \right\|^2 \right) \tag{6.11}$$

$G(\sigma)$ is now expressed as the product of a matrix and a vector. Substituting $\mathbf{J} = \partial \mathbf{F}(\boldsymbol{\sigma}_0)/\partial \boldsymbol{\sigma}$, $\bar{\mathbf{J}} = \partial \mathbf{F}(\mathbf{G}\boldsymbol{\sigma}_0)/\partial \mathbf{G}\boldsymbol{\sigma}$, $\mathbf{V}_e = \mathbf{V}_m - \mathbf{F}(\boldsymbol{\sigma}_0)$, $\bar{\mathbf{V}}_e = \bar{\mathbf{V}}_m - \mathbf{F}(\mathbf{G}\boldsymbol{\sigma}_0)$, $\Delta\boldsymbol{\sigma} = \boldsymbol{\sigma} - \boldsymbol{\sigma}_0$, and $\mathbf{G}\Delta\boldsymbol{\sigma} = \mathbf{G}\boldsymbol{\sigma} - \mathbf{G}\boldsymbol{\sigma}_0$, equation 6.10 and equation 6.11 can now be written as follows.

$$\boldsymbol{\sigma}^* = \arg\min_{\boldsymbol{\sigma}} \left\| \mathbf{V}_e - \mathbf{J}\Delta\boldsymbol{\sigma} \right\|^2 \tag{6.12}$$

$$\mathbf{G}\boldsymbol{\sigma}^* = \arg\min_{\boldsymbol{\sigma}} \left\| \bar{\mathbf{V}}_e - \bar{\mathbf{J}}\mathbf{G}\Delta\boldsymbol{\sigma} \right\|^2 \tag{6.13}$$

Again employing Tikhonov regularization, $\Delta\boldsymbol{\sigma}$ can be recovered from equation 6.12 and equation 6.13 as shown in equation 6.14 and equation 6.15.

$$\Delta\boldsymbol{\sigma} = \left(\mathbf{J}^T\mathbf{J} + \alpha^2\mathbf{L}^T\mathbf{L}\right)^{-1}\mathbf{J}^T\mathbf{V}_e \tag{6.14}$$

$$\Delta\boldsymbol{\sigma} = \left([\bar{\mathbf{J}}\mathbf{G}]^T[\bar{\mathbf{J}}\mathbf{G}] + \alpha^2\mathbf{L}^T\mathbf{L}\right)^{-1}[\bar{\mathbf{J}}\mathbf{G}]^T\bar{\mathbf{V}}_e \tag{6.15}$$

These two equations for $\Delta\boldsymbol{\sigma}$ can be combined as shown in equation 6.16.

$$\Delta\boldsymbol{\sigma} = \left(\begin{bmatrix}\mathbf{J}\\ \bar{\mathbf{J}}\mathbf{G}\end{bmatrix}^T\begin{bmatrix}\mathbf{J}\\ \bar{\mathbf{J}}\mathbf{G}\end{bmatrix} + \alpha^2\mathbf{L}^T\mathbf{L}\right)^{-1}\begin{bmatrix}\mathbf{J}\\ \bar{\mathbf{J}}\mathbf{G}\end{bmatrix}^T\begin{bmatrix}\mathbf{V}_e\\ \bar{\mathbf{V}}_e\end{bmatrix} \tag{6.16}$$

Although the coupling process considered only one conductivity change, this can be repeated for arbitrarily many known conductivity changes. For n known changes, equation 6.16 takes the form of equation 6.17.

$$\Delta\boldsymbol{\sigma} = \left(\begin{bmatrix}\mathbf{J}\\ \vdots\\ \bar{\mathbf{J}}^n\mathbf{G}^n\end{bmatrix}^T\begin{bmatrix}\mathbf{J}\\ \vdots\\ \bar{\mathbf{J}}^n\mathbf{G}^n\end{bmatrix} + \alpha^2\mathbf{L}^T\mathbf{L}\right)^{-1}\begin{bmatrix}\mathbf{J}\\ \vdots\\ \bar{\mathbf{J}}^n\mathbf{G}^n\end{bmatrix}^T\begin{bmatrix}\mathbf{V}_e\\ \vdots\\ \bar{\mathbf{V}}_e^n\end{bmatrix} \tag{6.17}$$

As in the standard EIT formulation, $\boldsymbol{\sigma}^*$ is updated as $\boldsymbol{\sigma}^*_{n+1} = \boldsymbol{\sigma}^*_n + \Delta\boldsymbol{\sigma}$. This approach is expected to be successful if $\mathrm{Rank}\left(\begin{bmatrix}\mathbf{J}\\ \vdots\\ \bar{\mathbf{J}}^n\mathbf{G}^n\end{bmatrix}\right) > \mathrm{Rank}(\mathbf{J})$.

Lastly, it is worth considering the formation of the strained sensitivity matrix, $\bar{\mathbf{J}}$.

$$\bar{J}_{MN\,e} = -\int_{\Omega_e}\frac{\partial u^M(\mathbf{G}\boldsymbol{\sigma})}{\partial x_i}\frac{\partial \bar{u}^N(\mathbf{G}\boldsymbol{\sigma})}{\partial x_i}\,\mathrm{d}\Omega_e \tag{6.18}$$

The functional dependence of $u^M = u^M(\mathbf{G}\boldsymbol{\sigma})$ is written explicitly to emphasize that these forward solutions are evaluated now with the strained conductivity, $\mathbf{G}\boldsymbol{\sigma}$. Also, it is worth reiterating that $\bar{u}$ is the forward solution due to the adjoint injection field whereas bars have been placed over symbols in this chapter to denote a quantity coming from the strained domain.

6.3.3 Simulation Procedures

To test the proposed coupling technique, the conductivity distribution of a reference finite element mesh will be reproduced. Consistent with good EIT practices, the reference mesh is more refined (∼2000 elements) than the EIT mesh (∼1300) elements and there exists no

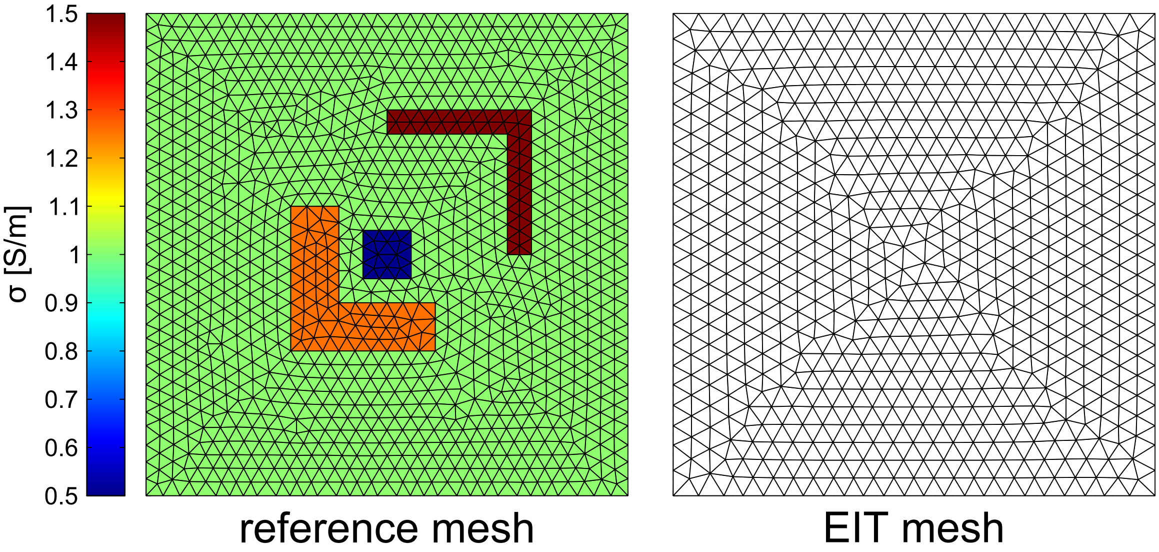

Figure 6.6: Reference mesh with an image to reproduce and the EIT mesh on which the image will be produced.

assemblage of elements in the EIT mesh that exactly matches the conductivity distribution of the reference mesh. Both the reference mesh and the EIT mesh can be seen in Figure 6.6.

In these simulations, a unit current is applied and unit background conductivity is used in a unit square domain. The incorporation of globally known conductivity changes will henceforth be referred to as enhancements. These enhancements take the form of two-dimensional sine waves.

$$G_{ee} = \sigma^e - \frac{\sigma^e}{10}\left(\sin\left(p\pi x_c^e\right)\sin\left(q\pi y_c^e\right)\right) \tag{6.19}$$

Here, $\mathbf{G}$ is a diagonal matrix the eth diagonal element of which is calculated by equation 6.19 where σ^e is the conductivity of the eth element, x_c^e is the x-coordinate of the centroid of the eth element, and y_c^e is the y-coordinate of the centroid of the eth element. p and q are integers ranging from 1 to 5. The form of these enhancements is selected based on the simple intuition regarding the orthogonality of sine waves.

6.3.4 Rank and Image Enhancement

The potential of the proposed coupling process is first assessed by using singular value decomposition to assess the rank of the sensitivity matrices for 4, 8, 12, and 16 electrodes with 0, 5, 15, and 25 enhancements. Singular value decomposition is an effective way to

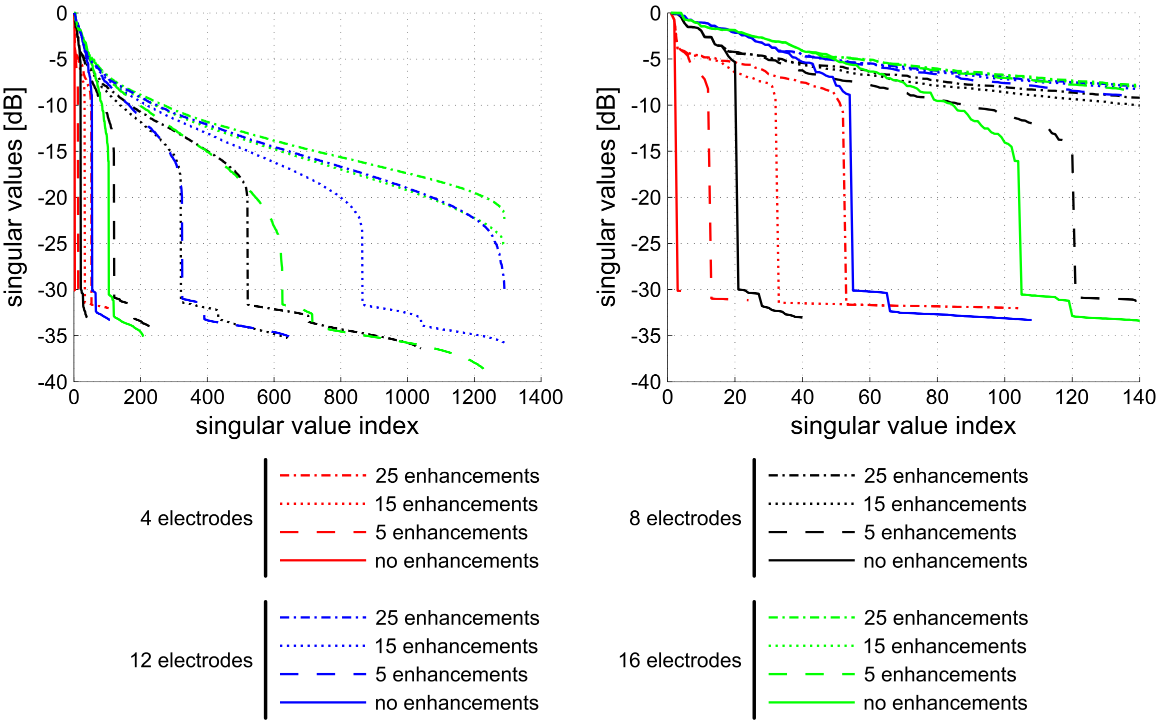

Figure 6.7: Rank assessment of unenhanced and enhanced sensitivity matrices by singular value decomposition. Left: plot of all scenarios considered. Right: close up of singular value indices up to 140.

visually ascertain the rank of large numerical matrices. As shown in Figure 6.7, the index at which there is a sudden drop of singular value corresponds to the rank of the sensitivity matrix.

A couple of important insights can be gleaned from Figure 6.7. First, recalling that there are ∼1300 elements in the EIT mesh, the singular value plots for 16 electrodes with 15 or 25 enhancements and 12 electrodes with 25 enhancements show that it is indeed possible to achieve a full rank sensitivity matrix. And, second, up to the point of being full rank, the rank seems to enhance in direct proportion to the number of enhancements. That is, the unenhanced sensitivity matrix has a rank of $(L-3)L/2$ where L is the total number of electrodes. Consider the 16 electrode case. Unenhanced, the sensitivity matrix has a rank of 104. With 5 enhancements, the singular values drop just past 600 which implies the rank of the enhanced sensitivity matrix is approximately $(1+n)(L-3)L/2$ where n is the number of enhancements.

Next, the potential of this approach is demonstrated by showing how enhancements affect image reconstruction. This is shown in Figure 6.8 where the distribution in Figure

6.7 is being reproduced by EIT. These results make it clear that the proposed coupling method can not only markedly enhance image quality but also significantly reduce the number of electrodes necessary to produce a quality image.

Although there are a couple of scenarios in which the sensitivity matrix is full rank, no perfect conductivity reconstructions exist in Figure 6.8. This is to be expected because of the care that was taken to avoid so called *inverse crimes* [134]. Furthermore, the image quality seems to reach a saturation point. That is, the images stop improving better beyond a certain quality. This is also a consequence of avoiding an *inverse crime*. Simply put, no perfect solution is available to EIT so enhancing the sensitivity matrix past the maximum rank does not produce a better image.

Lastly, a final example of the power of this approach is provided by comparing the image reconstruction with 16 electrodes and no enhancements to the image reconstruction with 16 electrodes and 25 enhancements on a much more complicated reference image as shown in Figure 6.9. In this example, the reference mesh has approximately 4000 elements and the EIT mesh has approximately 3000 thereby ensuring the enhanced sensitivity matrix is not full rank. Here, the unenhanced image captures the basic shape of the reference image, but consistent with the limitations of EIT, it is blurry and identifiable details are not discernable. The enhanced image, however, still is not perfect, but it is significantly improved to the point that the shape can be easily recognized and identified without knowledge of the reference image.

6.4 Summary and Conclusions

In this chapter, the influence of tailoring nanofiller alignment and directionality has been investigated to enhance delamination detection. Anisotropic conductivity values from the equivalent resistor network model developed in Chapter 4 were used to determine how alignment-induced anisotropy influences changes in boundary voltage due to damage. It was found that degree of alignment, orientation through the plate thickness, and anisotropic ratio all have a pronounced influence on sensitivity. Anisotropic EIT was then employed to locate a single and double delamination case for conductivities with $\phi_m = 45°$, 60°, and 75° at $\beta = 0°$, 30°, 60°, and 90° and 1% filler volume fraction. Compared to random nanofiller networks with isotropic conductivity, it was found that anisotropic conductivity markedly enhances EIT sensitivity, but overly anisotropic conductivity degrades the image. This implies that incorporating microscale nanocomposite tailoring has incredible potential to bolster structural-scale SHM and sensitivity to delaminations.

Next, a method of coupling the EIT image reconstruction process with globally known

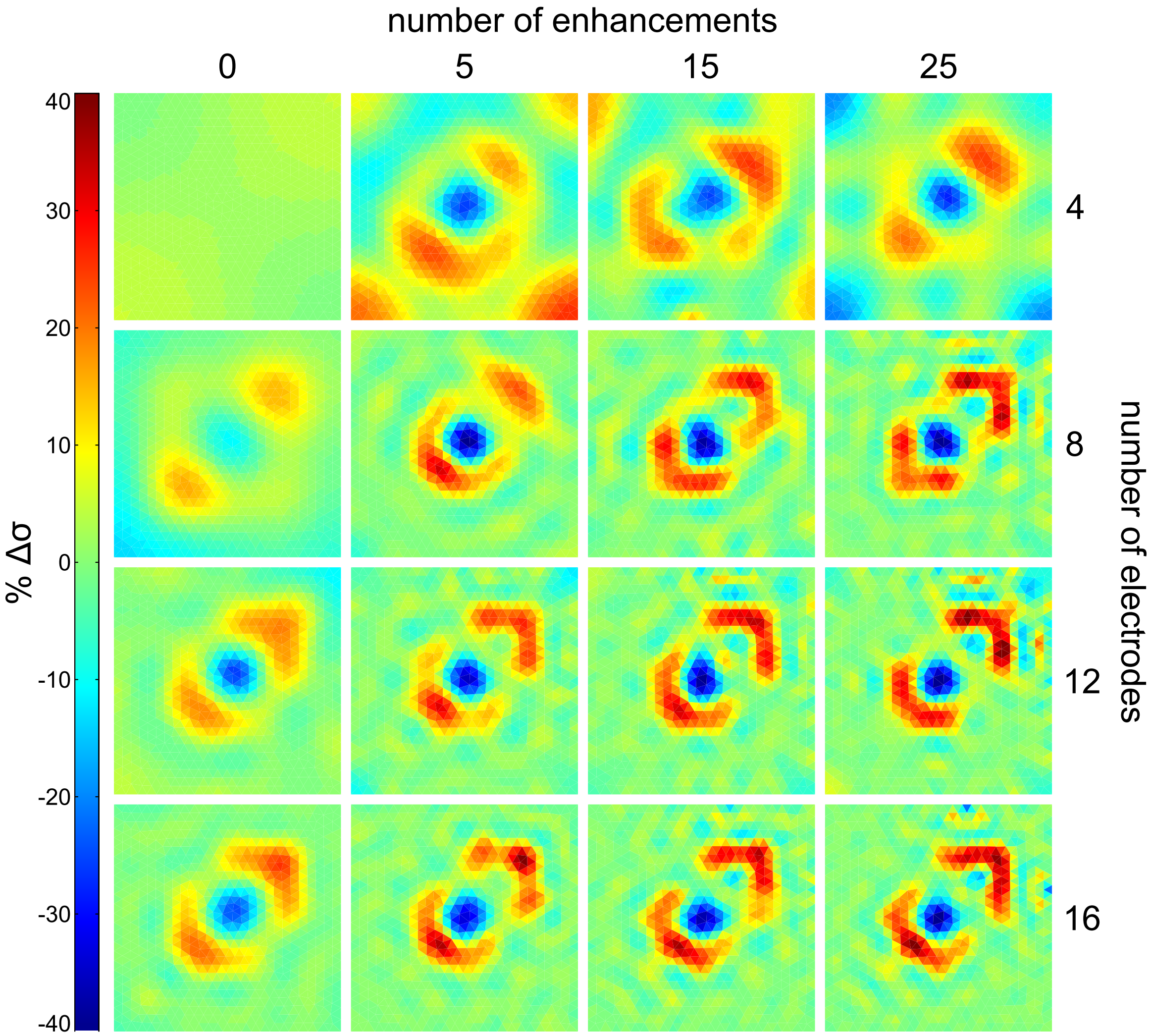

Figure 6.8: Influence of coupling enhancements on EIT images for 4, 8, 12, and 16 electrodes with 0, 5, 15, 25 enhancements. As expected from the singular value decomposition analysis, for a given number of electrodes, adding enhancements significantly improves the image.

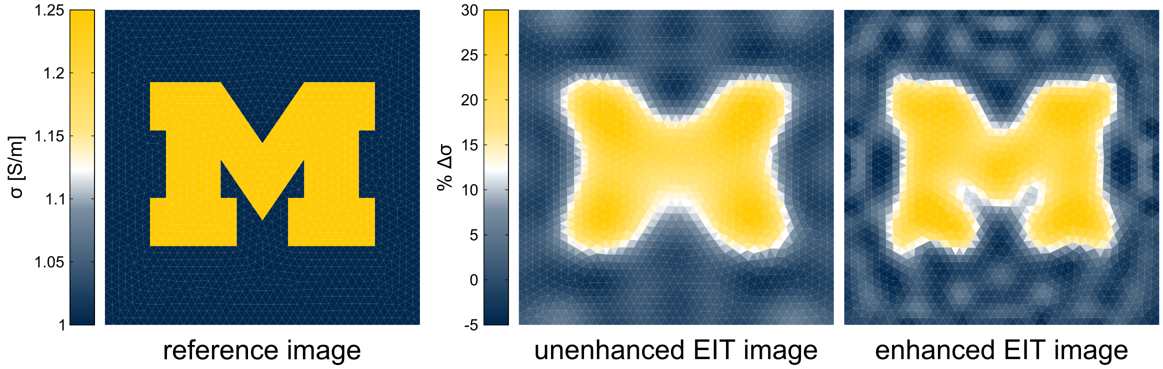

Figure 6.9: Comparison of unenhanced image with an image produced with 25 enhancements. Both use 16 electrodes. In this more complicated example, the enhanced image very decidedly outperforms the unenhanced image.

conductivity changes was postulated and formulated. This approach, motivated by piezoresistive nanocomposites, is predicated on the supposition that adding additional constraints to the sensitivity matrix to enhance its rank will result in a better image or, alternatively, can enable quality images to be produced with fewer electrodes. Singular value decomposition analysis showed that the coupling process does indeed enhance the rank of the sensitivity matrix, and image reconstruction examples demonstrated the potential of this approach by producing markedly superior images. Unlike other multi-physics EIT enhancement techniques, this approach does not necessarily impose upon the advantages of EIT. Particularly for nanocomposite SHM, this technique has considerable potential to significantly enhance image quality or reduce the implementation burden of EIT.

CHAPTER 7

Summary of Scholarly Contributions and Broader Impacts

This research radically expands the potential of EIT for conductivity-based health monitoring of nanocomposites by first extending the fundamental knowledge of nanocomposite conductivity, concretely demonstrating the potential of EIT for strain and damage identification in nanocomposites, and lastly, significantly advancing state of the art EIT by exploiting the unique properties of nanocomposites. The scholarly contributions and broader impacts of each chapter are summarized below.

7.1 Nanocomposite Conductive Properties

Factors influencing nanocomposite conductivity including strain, nanofiller alignment, and electric current-induced temperature loading have been studied in Chapter 4. Because of their potential as high-sensitivity strain sensors, considerable effort has been dedicated to piezoresistivity modeling. Equivalent resistor network piezoresistivity models are computationally burdensome, limited to micro-scale analysis, and over predict piezoresistive response. Percolation-based models have yielded accurate predictions but, again, are limited to tensile strain. An analytical piezoresistivity model for CNT nanocomposites was developed to address this limitation in the state of the art. Model predictions agree well with existing experimental piezoresistivity literature, and the model is amenable to the finite element formulation thereby enabling the analysis of complicated structures subjected to arbitrary strains. This represents an important broader impact and step in transitioning piezoresistive analysis from micro to structural scales.

Next, the influence of nanofiller alignment on transverse properties was studied. While considerable attention has been paid to the influence of alignment on conductivity in the alignment direction, little consideration had been paid to transverse properties. Because of the potential to enhance sensitivity to delaminations, there is a strong interest in aligning nanofillers from a SHM perspective. A knowledge gap therefore existed which was addressed by contributing fundamental insights on transverse percolation and conductivity.

Nanocomposites also exhibit conductivity evolution under electrical loading. Because different nanocomposites demonstrate different conductivity evolution responses, understanding the mechanisms of any particular nanocomposite is important. Chapter 4 experimentally studied the conductivity evolution of a CNF/epoxy. EIS was employed at elevated temperatures to determine that the dominant mechanism of conductivity evolution in CNF/epoxy is thermal expansion. Because of this, CNF/epoxy conductivity decreases with time due to electrical loading. EIT was then modified to image the rate of conductivity change, and it was speculated that the rate of conductivity change is influenced by the nanofiller distribution with regions of more densely packed nanofillers evolving less rapidly and regions of more sparsely packed nanofillers evolving more rapidly. These findings are important scholarly contributions to the fundamental understanding of how CNF/epoxy responds to electrical loading.

7.2 Damage and Strain Detection via Electrical Impedance Tomography

Based on the literature review in Chapter 1, conductivity-based health monitoring has potential for unprecedented levels of integrated and continuous damage detection in fibrous composites. Considerable attention has been devoted to damage detection in fiber-reinforced composites with nanocomposite matrices by resistance change methods in the literature, but these methods employ unpalatable arrays of electrodes. EIT has also been diligently studied for damage detection in CNT thin films and sensing sprays applied to GFRPs. However, no work had previously been done that utilizes EIT for damage detection in fiber-reinforced composites with nanocomposite matrices. This gap in the literature has been addressed by investigating the potential of EIT to detect damage to CNF/epoxy and glass fiber/epoxy laminates with CB filler and strain in CNF/PU. This approach combines the entirely self-sensing capabilities of a nanocomposite matrix with the superior imaging of EIT. A considerable improvement over resistance change methods, damage was detected using only 16 electrodes. And, compared to sensing coat approaches, a completely self-sensing matrix will be sensitive to both internally and externally initiated damage, is immune to superficial damage, and does not contribute parasitic weight. Therefore, important scholarly contributions are made by addressing a gap in existing conductivity-based SHM literature while simultaneously making a broader impact by demonstrating the applicability of EIT for SHM in nanocomposites.

7.3 Methods for Electrical Impedance Tomography Enhancement

Despite the potential of EIT for health monitoring, it has important limitations. Chapter 6 advances the state of the art by contributing insightful knowledge on how EIT can be enhanced. While these advances were motivated by SHM applications and nanocomposite properties, they are potentially applicable to a wide array of EIT applications.

First, the sensitivity of EIT to delamination damage was enhanced. This was done by investigating how nanofillers could be aligned to induce anisotropic conductivity and then investigating which anisotropic conductivity produced the greatest delamination-induced change in boundary voltage. It was found that nanofiller alignment can markedly enhance the sensitivity of EIT to delaminations. However, it was also found that overly anisotropic conductivity, while producing larger delamination-induced boundary voltage changes, was difficult for EIT to reconstruct. This result is an important broader impact because it shows that EIT is indeed capable of robustly detecting one of the most notoriously difficult to detect damage modes of composites, delaminations.

Next, the poor resolution or, synonymously, the need for large electrode arrays was addressed. This was done by identifying the root cause of these limitations to be the rank deficiency of the sensitivity matrix. The rank of the sensitivity matrix was then bolstered by coupling the image reconstruction process with known conductivity changes such as those induced by strain in piezoresistive nanocomposites. It was found that the image quality of EIT can significantly be enhanced by this process. Alternatively, the number of electrodes needed to produce quality images can be significantly abated. This is a potentially high-impact result because not only does it increase the appeal of EIT for SHM applications, but it shows that multi-physics coupling to enhance the rank of the sensitivity matrix can radically improve image quality which is EIT's greatest limitation from a biomedical imaging perspective.

CHAPTER 8

Recommendations for Future Work

This thesis has convincingly demonstrated the potential of EIT for conductivity-based damage and strain identification, developed novel insights into nanocomposite conductive properties, and leveraged these insights to develop a theoretical frame work to fundamentally enhance EIT. However, it is the author's opinion that, while promising, conductivity-based SHM via EIT is a relatively immature field and will require due diligence before it is truly field-worthy. Nonetheless, because of the potential to develop self-sensing fibrous composites with the ability to spatially resolve damage and strain, the author also believes conductivity-base SHM via EIT is worth pursuing. This chapter further details what the author perceives to be important areas of future work.

First, implementation of EIT in the field or on in-service structures has several challenges. Robust, practical electrodes need to be researched and developed. Using silver paste and copper tape works well in laboratory settings, but these methods would fail abysmally on in-service structures. Ideally, electrodes should be manufactured into fiber-reinforced composites rather than being applied as an afterthought. Furthermore, efficient, robust, and adaptable EIT algorithms will be necessary for field deployment. This means that the routine can automatically handle and adapt to, for example, an electrode malfunctioning or a non-convergent solution without human assistance. And, because EIT necessarily consumes power for current injections, future work should concentrate on developing technologies capable of generating and supplying this power while in-service on the structure. Energy harvesting methods, for example, have potential in this regard.

The second area of future research regards the development of fiber-reinforced composites with nanocomposite matrices. At present, it is possible to achieve high conductivities and uniform dispersion without structural fibers, but these properties both drop markedly in the presence of reinforcing fibers. Overly resistive materials will require the application of prohibitively large voltages to conduct EIT. Methods of inducing nanofiller chaining [81], however, show promise to facilitate the formation of well-connected and therefore more conductive nanofiller networks in fiber-reinforced composites. Furthermore, because of the incredible diversity among piezoresistive responses, much more fundamental research is required before nanocomposites can be employed for integrated strain sensing.

The author's success, albeit entirely analytical, with enhancing the image quality of EIT gives him strong reason to believe that, particularly in biomedical applications, EIT has incredible potential to be transformed into a powerful imaging modularity. The key will be to find the multi-physics coupling that not only addresses the rank deficiency of the sensitivity matrix but also retains EIT's most valuable assets such as low cost, portability, and being completely benign in biomedical applications. In addition to further researching methods of enhancing EIT, experimental work should be undertaken to verify the coupling process herein presented. The author recommends doing so by employing phantom tanks as is common practice in medical EIT development. That is, a small tank should be filled with conducting fluid (e.g. saline water) and some artifact to be imaged by EIT placed in the tank. This artifact could be, for example, a gelatin mold with a conductivity that is different than the saline. Next, known conductivity changes can be induced by precisely placing sections of gelatin of a third conductivity with known geometry into the phantom tank and correspondingly updating the forward problem and $\mathbf{G}$ to reflect this. This approach, while far from practical SHM or medical applications, would be an important proof of concept that experimental EIT can indeed be greatly bolstered by addressing the rank deficiency of the sensitivity matrix. A phantom would be the ideal setup to very carefully induce known conductivity changes. An example of an EIT phantom can be seen in Figure 8.1.

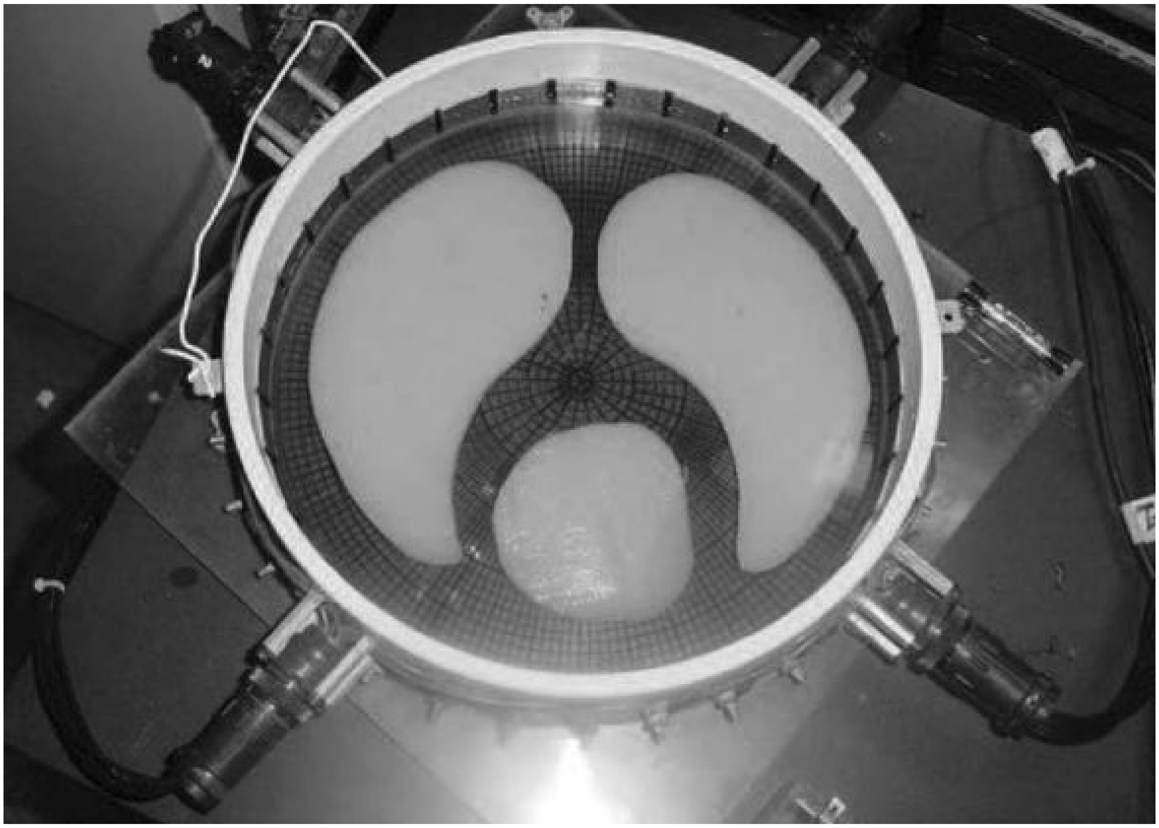

Figure 8.1: Example of an EIT phantom tank [8].

APPENDIX A

Detailed Forward Problem Formulation

A.1 Introduction

This appendix more diligently treats the finite element formulation of the forward problem with explicit solutions for the forward problem CEM matrices in two and three dimensions. This content has been relegated to an appendix because the finite element formulation is necessary to this research but not advanced by it.

Unless otherwise state, indicial notation is used in the following. Summation is implied over repeated subscripts. However, description of the finite element methods can result in a plethora of subscripts and superscripts. Indicial notation has been abandoned in these instances for clarity. Linear interpolation functions are used in this research and the explicitly computed CEM matrices, but the general forms of the CEM matrices are derived for any order of interpolation. Conductivity has also been assumed to be a completely general tensor. Also, because their gradients are constant vectors, only linear triangular and tetrahedral elements are considered in this appendix. Hexahedral elements have been used at several points in the preceding chapters, but converting triangular/tetrahedral code to quadrilateral/hexahedral code is straight-forward.

A.2 Formulation of Steady State Diffusion Weak Form and Discretization

Consider the domain equation for steady-state diffusion [61] [135] [136].

$$-\frac{\partial j_i}{\partial x_i} = \frac{\partial}{\partial x_j}\sigma_{ij}\frac{\partial u}{\partial x_j} = f \tag{A.1}$$

Here, j_i is the current density vector, σ_{ij} is the conductivity tensor, u is the domain potential, and f is an internal current source. It is assumed that the total current flowing through active electrodes is known and no current flows through boundaries of the domain where electrodes are not attached. These conditions are expressed as follows.

$$\int_{E_l} \sigma_{ij} \frac{\partial u}{\partial x_i} n_j \, \mathrm{d}S_l = I_l \tag{A.2}$$

$$\sigma_{ij} \frac{\partial u}{\partial x_i} n_j = 0 \text{ off } \bigcup_{l=1}^{L} E_l \tag{A.3}$$

The outward pointing normal is specified as n_i and the total number of electrodes is L. In addition to the interface condition given in equation 3.2, equation A.4 enforces conservation of charge.

$$\sum_{l=1}^{L} I_l = 0 \tag{A.4}$$

Now, formulate the weak form of equation A.1 according to variational principles by multiplying it by a weighting function ψ that satisfies the Dirichlet boundary conditions and integrating the result over the domain.

$$\int_{\Omega} \psi \frac{\partial}{\partial x_j} \sigma_{ij} \frac{\partial u}{\partial x_j} \, \mathrm{d}\Omega = \int_{\Omega} \psi f \, \mathrm{d}\Omega \tag{A.5}$$

An absence of internal sources is assumed resulting in $f = 0$. Using Green's second identity and the vector identity $\frac{\partial}{\partial x_j} \psi \sigma_{ij} \frac{\partial u}{\partial x_i} = \frac{\partial \psi}{\partial x_i} \sigma_{ij} \frac{\partial u}{\partial x_j} + \psi \frac{\partial}{\partial x_j} \sigma_{ij} \frac{\partial u}{\partial x_j}$, equation A.5 becomes

$$\int_{\Omega} \frac{\partial}{\partial x_j} \psi \sigma_{ij} \frac{\partial u}{\partial x_i} \, \mathrm{d}\Omega - \int_{\Omega} \frac{\partial \psi}{\partial x_i} \sigma_{ij} \frac{\partial u}{\partial x_j} \, \mathrm{d}\Omega = 0. \tag{A.6}$$

By the divergence theorem, equation A.6 can be rewritten as

$$\int_{\Omega} \frac{\partial \psi}{\partial x_i} \sigma_{ij} \frac{\partial u}{\partial x_j} \, \mathrm{d}\Omega = \int_{\partial\Omega} \psi \sigma_{ij} \frac{\partial u}{\partial x_i} n_j \, \mathrm{d}S = \int_{\Gamma} \sigma_{ij} \frac{\partial u}{\partial x_j} n_j \psi \, \mathrm{d}S \tag{A.7}$$

where $\Gamma = \bigcup_l E_l$ is the union of the electrodes and equation A.3 is enforced off the electrodes. Substituting the domain-electrode CEM interface condition from equation 3.2 into equation A.7 results in the following relation.

$$\int_{\Omega} \frac{\partial \psi}{\partial x_i} \sigma_{ij} \frac{\partial u}{\partial x_j} \, \mathrm{d}\Omega = \sum_{l=1}^{L} \int_{E_l} \frac{1}{z_l} \left(V_l - u \right) \psi \, \mathrm{d}S_l \tag{A.8}$$

Equation A.8 is discretized by partitioning the domain Ω into disjoint subsets Ω_e so that it can be expressed as an assembly of subsets.

$$\sum_e \int_{\Omega_e} \frac{\partial \psi_e}{\partial x_i} \sigma_{ij} \frac{\partial u_e}{\partial x_j} \, \mathrm{d}\Omega_e = \sum_e \sum_{l=1}^{L} \int_{\partial\Omega_e} \frac{1}{z_l} \left(V_l - u_e \right) \psi_e \, \mathrm{d}S_e \tag{A.9}$$

Here, $\sum_e(\cdot)$ implies the assembly of elements. u and ψ are now expressed element-wise in the following manner.

$$u_e = \sum_{A=1}^{N} w^A d_e^A \tag{A.10}$$

$$\psi_e = \sum_{A=1}^{N} w^A c_e^A \tag{A.11}$$

d_e^A is the solution to the forward problem at the *A*th node of the *e*th element, and c_e^A is the variation of the *A*th node of the *e*th element. Equation A.10 is the interpolation of the nodal solutions over the *e*th element and summed over N nodes per element. The nodal solutions are recovered by minimizing equation A.9 with respect to the nodal variations.

A.3 Formulation of Complete Electrode Model Matrices

Consider the left hand side of equation A.9 for the *e*th element. Upon substituting equation A.10 and equation A.11 for u_e and ψ_e,

$$\int_{\Omega_e} \frac{\partial \psi_e}{\partial x_i} \sigma_{ij} \frac{\partial u_e}{\partial x_j} \, \mathrm{d}\Omega_e = \sum_{A=1}^{N} \sum_{B=1}^{N} c_e^A \int_{\Omega_e} \frac{\partial w^A}{\partial x_i} \sigma_{ij} \frac{\partial w^B}{\partial x_j} \, \mathrm{d}\Omega_e \, d_e^B. \tag{A.12}$$

Because c_e^A and d_e^A are constants, they are pulled outside of the integral. In order to form the gradients of the interpolation functions, the interpolation functions must first be defined. Defining the interpolation functions as $w^A = w^A(x_i)$ makes evaluating the integrals in equation A.9 unpalatable and computationally inefficient. Instead, define the interpolation functions on an isoparametric domain.

$$x_i = \sum_{A=1}^{N} w^A \left(\zeta \right) x_i^A \tag{A.13}$$

x_i^A is the *i*-coordinate of the *A*th node. This isoparametric mapping is depicted for a tetrahedral element in Figure A.1. Similarly, a triangular element can be mapped to the $\zeta_1 - \zeta_2$ plane of Figure A.1, and a line can be mapped to a bi-unit domain running from $\zeta = -1$ to $\zeta = 1$.

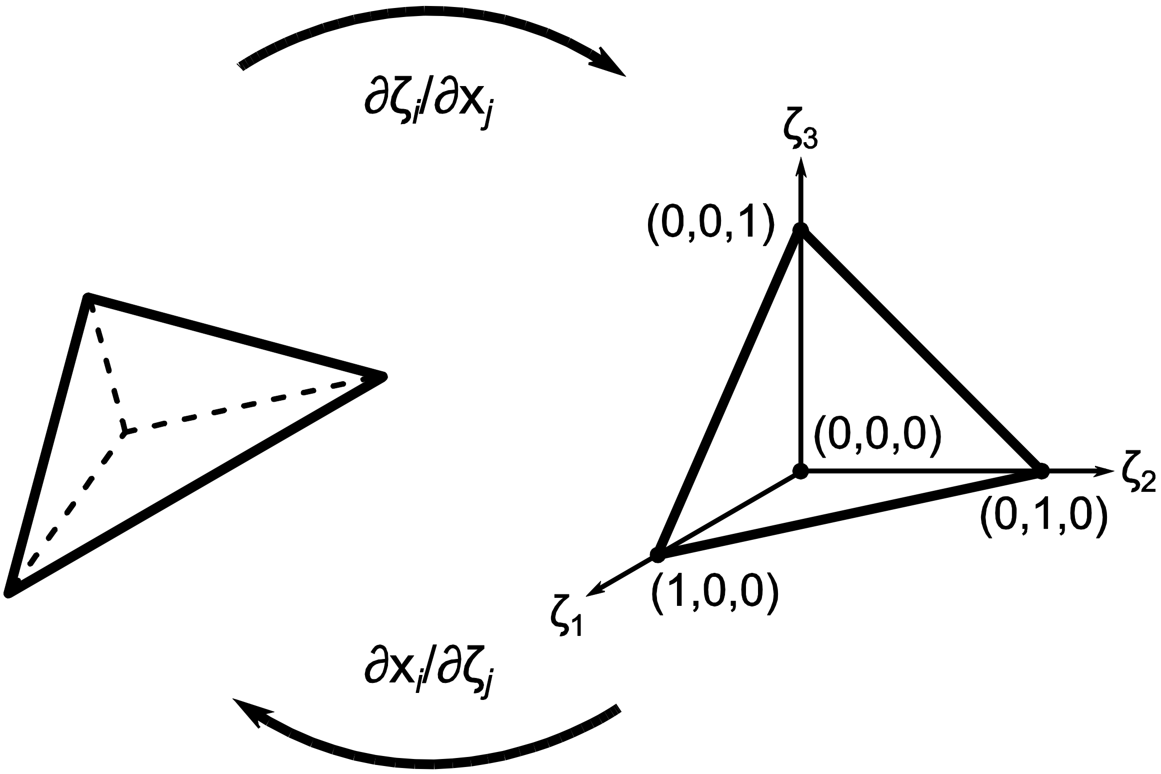

Figure A.1: An arbitrary tetrahedral element depicted to the left is mapped to the isoparametric domain shown to the right by the inverse of the Jacobian operator.

Now the chain rule of differentiation can be employed to form the gradient of the interpolation functions.

$$\frac{\partial w^A}{\partial x_i} = \frac{\partial w^A}{\partial \zeta_j}\frac{\partial \zeta_j}{\partial x_i} \tag{A.14}$$

Recognize $\partial\zeta_i/\partial x_j$ as the inverse of $\partial x_i/\partial\zeta_j$ which can be formed by differentiating equation A.13. Equation A.12 can now be rewritten as follows.

$$\int_{\Omega_e} \frac{\partial \psi_e}{\partial x_i}\sigma_{ij}\frac{\partial u_e}{\partial x_j}\,\mathrm{d}\Omega_e = \sum_{A=1}^{N}\sum_{B=1}^{N} c_e^A \int_{\Omega_e} \frac{\partial w^A}{\partial \zeta_k}\frac{\partial \zeta_k}{\partial x_i}\sigma_{ij}\frac{\partial w^B}{\partial \zeta_l}\frac{\partial \zeta_l}{\partial x_j}\,\mathrm{d}\Omega_e\, d_e^B \tag{A.15}$$

Because of the isoparametric domains selected, integrals over these domains can be evaluated exactly using numerical quadrature with appropriately selected Lagrange polynomials. Linear elements are used in this research, and tetrahedral, triangle, and line elements will be detailed here. That is, $w^1 = \zeta_1$, $w^2 = \zeta_2$, $w^3 = \zeta_3$, and $w^4 = 1 - \zeta_1 - \zeta_2 - \zeta_3$ in three dimensions; $w^1 = \zeta_1$, $w^2 = \zeta_2$, and $w^3 = 1 - \zeta_1 - \zeta_2$ in two dimensions; and $w^1 = {}^1\!/\!{}_2(1-\zeta)$ and $w^2 = {}^1\!/\!{}_2(1+\zeta)$ in one dimension. Expressing equation A.15 in the isoparametric domain requires the integrand be multiplied by $\det\left|\partial x_i/\partial\zeta_j\right|$.

$$\int_{\Omega_e} \frac{\partial \psi_e}{\partial x_i}\sigma_{ij}\frac{\partial u_e}{\partial x_j}\,\mathrm{d}\Omega_e = \sum_{A=1}^{N}\sum_{B=1}^{N} c_e^A \int_{\Omega_{e_\zeta}} \frac{\partial w^A}{\partial \zeta_k}\frac{\partial \zeta_k}{\partial x_i}\sigma_{ij}\frac{\partial w^B}{\partial \zeta_l}\frac{\partial \zeta_l}{\partial x_j}\det\left|\frac{\partial x_m}{\partial \zeta_n}\right|\,\mathrm{d}\Omega_{e_\zeta}\, d_e^B \tag{A.16}$$

Ω_{e_ζ} denotes integration of the *e*th element in the isoparametric domain. The integral in equation A.16 can now be evaluated as a sum of weighted polynomials evaluated at quadrature points as follows.

$$\int_{\Omega_{e_\zeta}} p\left(\zeta_i\right)\,\mathrm{d}\Omega_{e_\zeta} = \sum_{m}^{M} a_m p\left(\zeta_m\right) \tag{A.17}$$

Here, the summation runs over the number of quadrature points and a_m is the *m*th weight. Returning to equation A.16, since the nodal solution and nodal variation have been moved outside the integral, every part of the integrand is known and it can be evaluated to form the local diffusion stiffness matrix for the *e*th element.

$$\int_{\Omega_e} \frac{\partial \psi_e}{\partial x_i} \sigma_{ij} \frac{\partial u_e}{\partial x_j} \, \mathrm{d}\Omega_e = \sum_{A=1}^{N} \sum_{B=1}^{N} c_e^A k_e^{AB} d_e^B$$

$$= \begin{bmatrix} c_e^1 & c_e^2 & \dots & c_e^N \end{bmatrix} \mathbf{k}_e \begin{bmatrix} d_e^1 \\ d_e^2 \\ \vdots \\ d_e^N \end{bmatrix} \tag{A.18}$$

k_e^{AB} is the local diffusion stiffness matrix of the *e*th element and can be assembled into the global diffusion stiffness matrix $\mathbf{A}_M$. As also shown in equation A.18, the summations over the interpolation functions can be expressed through linear algebra.

For two-dimensional analysis with linear triangle elements, the local diffusion stiffness matrix for the *e*th element is

$$\mathbf{k}_e = \frac{1}{2} \begin{bmatrix} 1 & 0 \\ 0 & 1 \\ -1 & -1 \end{bmatrix} \begin{bmatrix} x_1^e - x_3^e & x_2^e - x_3^e \\ y_1^e - y_3^e & y_2^e - y_3^e \end{bmatrix}^{-1} \begin{bmatrix} \sigma_{11} & \sigma_{12} \\ \sigma_{21} & \sigma_{22} \end{bmatrix} \dots$$

$$\dots \begin{bmatrix} x_1^e - x_3^e & x_2^e - x_3^e \\ y_1^e - y_3^e & y_2^e - y_3^e \end{bmatrix}^{-T} \begin{bmatrix} 1 & 0 \\ 0 & 1 \\ -1 & -1 \end{bmatrix}^T \det \left| \begin{bmatrix} x_1^e - x_3^e & x_2^e - x_3^e \\ y_1^e - y_3^e & y_2^e - y_3^e \end{bmatrix} \right| . \tag{A.19}$$

For three-dimensional analysis with linear tetrahedral elements, the local diffusion stiffness matrix for the *e*th element is

$$\mathbf{k}_e = \frac{1}{6}\begin{bmatrix} 1 & 0 & 0 \\ 0 & 1 & 0 \\ 0 & 0 & 1 \\ -1 & -1 & -1 \end{bmatrix} \begin{bmatrix} x_1^e - x_4^e & x_2^e - x_4^e & x_3^e - x_4^e \\ y_1^e - y_4^e & y_2^e - y_4^e & y_3^e - y_4^e \\ z_1^e - z_4^e & z_2^e - z_4^e & z_3^e - z_4^e \end{bmatrix}^{-1} \cdots$$

$$\cdots \begin{bmatrix} \sigma_{11} & \sigma_{12} & \sigma_{13} \\ \sigma_{21} & \sigma_{22} & \sigma_{23} \\ \sigma_{31} & \sigma_{32} & \sigma_{33} \end{bmatrix} \begin{bmatrix} x_1^e - x_4^e & x_2^e - x_4^e & x_3^e - x_4^e \\ y_1^e - y_4^e & y_2^e - y_4^e & y_3^e - y_4^e \\ z_1^e - z_4^e & z_2^e - z_4^e & z_3^e - z_4^e \end{bmatrix}^{-T} \cdots$$

$$\cdots \begin{bmatrix} 1 & 0 & 0 \\ 0 & 1 & 0 \\ 0 & 0 & 1 \\ -1 & -1 & -1 \end{bmatrix}^{T} \det \left| \begin{bmatrix} x_1^e - x_4^e & x_2^e - x_4^e & x_3^e - x_4^e \\ y_1^e - y_4^e & y_2^e - y_4^e & y_3^e - y_4^e \\ z_1^e - z_4^e & z_2^e - z_4^e & z_3^e - z_4^e \end{bmatrix} \right| . \quad \text{(A.20)}$$

Indicial notation has been abandoned here, and x_i^e, y_i^e, or z_i^e is the x-, y-, or z-coordinate of the *i*th node of the *e*th element. This abuse of indicial notation elucidates subscripts and nodal coordinates. The gradients of the interpolation functions with respect to their independent variables have been evaluated in equation A.19 and equation A.20. Because the interpolation functions are linear, their gradients are constant and the integral of equation A.16 can be evaluated immediately. However, equation A.17 will need to be used for higher order interpolation functions. Also, recognize the area of the *e*th triangular element as

$$A^e = \frac{1}{2}\det \left| \begin{bmatrix} x_1^e - x_3^e & x_2^e - x_3^e \\ y_1^e - y_3^e & y_2^e - y_3^e \end{bmatrix} \right| \quad \text{(A.21)}$$

and the volume of the *e*th tetrahedral element as

$$V^e = \frac{1}{6}\det \left| \begin{bmatrix} x_1^e - x_4^e & x_2^e - x_4^e & x_3^e - x_4^e \\ y_1^e - y_4^e & y_2^e - y_4^e & y_3^e - y_4^e \\ z_1^e - z_4^e & z_2^e - z_4^e & z_3^e - z_4^e \end{bmatrix} \right| . \quad \text{(A.22)}$$

$\mathbf{A}_Z$, $\mathbf{A}_W$, and $\mathbf{A}_D$ can be formed by isolating the remaining integrals in equation A.9. Similar to the development of $\mathbf{k}_e$, the integrals in equation A.9 can be written in terms of equation A.10 and equation A.11 with nodal solutions and variations pulled outside the integral as vectors. The right hand side of equation A.9 for the *l*th electrode can be rewritten as follows.

$$\sum_e \int_{\partial\Omega_e} \frac{1}{z_l}\left(V_l - u_e\right)\psi_e \,\mathrm{d}S_e = \sum_e \left(-\int_{\partial\Omega_e} \frac{1}{z_l} u_e \psi_e \,\mathrm{d}S_e + \int_{\partial\Omega_e} \frac{1}{z_l} V_l \psi_e \,\mathrm{d}S_e\right) \tag{A.23}$$

$\mathbf{A}_Z$ and $\mathbf{A}_W$ can be formed by moving the right hand side of equation A.23 to the left hand side of equation A.9 and substituting equation A.10 and equation A.11. First, however, it is important to the CEM formulation to use the correct interpolation functions when forming the CEM matrices. The element diffusion stiffness matrices use interpolation functions that are of the same dimension of the domain, but $\mathbf{A}_Z$ and $\mathbf{A}_W$ are formed using interpolation functions one degree lower than the dimension of the domain. For example, a two-dimensional simulation uses $w_1 = \zeta_1$, $w_2 = \zeta_2$, and $w_3 = 1 - \zeta_1 - \zeta_2$ in the domain, but $w_1 = {}^1\!/\!_2(1-\zeta)$ and $w_2 = {}^1\!/\!_2(1+\zeta)$ are used to form $\mathbf{A}_Z$ and $\mathbf{A}_W$. To form $\mathbf{A}_Z$ and $\mathbf{A}_W$, the explicit steps of expressing integrals in the isoparametric domain will not be shown, but the final expression for linear elements will reflect the transformation.

To form $\mathbf{A}_Z$, use the first integral on the right hand side of equation A.23 and consider the *e*th element of the *l*th electrode.

$$\begin{aligned}\int_{\Omega_e} \frac{1}{z_l} u_e \psi_e \,\mathrm{d}S_e &= \sum_{A=1}^{N}\sum_{B=1}^{N} c_e^A \int_{\Omega_e} \frac{1}{z_l} w^A w^B \,\mathrm{d}S_e \, d_e^B \\ &= \begin{bmatrix} c_e^1 & c_e^2 & \dots c_e^N \end{bmatrix} \mathbf{A}_Z^{el} \begin{bmatrix} d_e^1 \\ d_e^2 \\ \vdots \\ d_e^N \end{bmatrix}\end{aligned} \tag{A.24}$$

The integral in equation A.24 can be evaluated to find the $\mathbf{A}_Z$ matrix of the *e*th element of the *l*th electrode. The $\mathbf{A}_Z$ matrix of the *e*th linear line element of the *l*th electrode in two-dimensional analysis is

$$\begin{aligned}\mathbf{A}_Z^{el} &= \int_{-1}^{1} \frac{h^e}{8z_l} \begin{bmatrix} 1 - 2\zeta + \zeta^2 & 1 - \zeta^2 \\ 1 - \zeta^2 & 1 + 2\zeta + \zeta^2 \end{bmatrix} \mathrm{d}\zeta \\ &= \frac{h^e}{6z_l} \begin{bmatrix} 2 & 1 \\ 1 & 2 \end{bmatrix}.\end{aligned} \tag{A.25}$$

h^e is the line element length. The $\mathbf{A}_Z$ matrix of the *e*th linear triangle element of the *l*th electrode in three-dimensional analysis is

$$\mathbf{A}_Z^{e\,l} = \int_0^1 \int_0^{1-\zeta_1} \frac{2A^e}{z_l} \begin{bmatrix} \zeta_1^2 & \zeta_1\zeta_2 & \zeta_1\left(1-\zeta_1-\zeta_2\right) \\ \zeta_1\zeta_2 & \zeta_2^2 & \zeta_2\left(1-\zeta_1-\zeta_2\right) \\ \zeta_1\left(1-\zeta_1-\zeta_2\right) & \zeta_2\left(1-\zeta_1-\zeta_2\right) & \left(1-\zeta_1-\zeta_2\right)^2 \end{bmatrix} \mathrm{d}\zeta_2\,\mathrm{d}\zeta_1$$
$$= \frac{A^e}{12z_l} \begin{bmatrix} 2 & 1 & 1 \\ 1 & 2 & 1 \\ 1 & 1 & 2 \end{bmatrix}. \tag{A.26}$$

$\mathbf{A}_Z^{e\,l}$ is formed for every element that is part of an electrode. These matrices are then assembled into the global $\mathbf{A}_Z$ matrix.

$\mathbf{A}_W$ links the domain voltage to the electrode voltages. Its number of rows equals the number of nodes in the finite element simulation, and its number of columns equals the number of electrodes. Specifying an electrode corresponds to specifying a column vector in $\mathbf{A}_W$. To form $\mathbf{A}_W$, use the second integral on the right hand side of equation A.23 and consider the *e*th element of the *l*th electrode.

$$-\int_{\Omega_e} \frac{1}{z_l}\psi_e V_l \,\mathrm{d}S_e = -\sum_{A=1}^{N} c_e^A \int_{\Omega_e} \frac{1}{z_l} w^A \,\mathrm{d}S_e \, V_l$$
$$= \begin{bmatrix} c_e^1 & c_e^2 & \ldots & c_e^N \end{bmatrix} \mathbf{A}_W^{e\,l} V_l \tag{A.27}$$

Because the voltage is assumed to be constant on each electrode, V_l is also pulled out of the integral. The $\mathbf{A}_W$ column vector of the *e*th linear line element of the *l*th electrode in two-dimensional analysis is

$$\mathbf{A}_W^{e\,l} = -\int_{-1}^{1} \frac{h^e}{2z_l} \begin{bmatrix} \frac{1}{2}\left(1-\zeta\right) \\ \frac{1}{2}\left(1+\zeta\right) \end{bmatrix} \mathrm{d}\zeta$$
$$= -\frac{h^e}{2z_l} \begin{bmatrix} 1 \\ 1 \end{bmatrix}. \tag{A.28}$$

The $\mathbf{A}_W$ column vector of the *e*th linear triangle element of the *l*th electrode in three-dimensional analysis is

$$\mathbf{A}_W^{el} = -\int_0^1 \int_0^{1-\zeta_1} \frac{2A^e}{z_l} \begin{bmatrix} \zeta_1 \\ \zeta_2 \\ 1-\zeta_1-\zeta_2 \end{bmatrix} \mathrm{d}\zeta_2 \, \mathrm{d}\zeta_1$$

$$= -\frac{A^e}{3z_l} \begin{bmatrix} 1 \\ 1 \\ 1 \end{bmatrix}. \tag{A.29}$$

Computationally, the formation of $\mathbf{A}_D$ is straightforward, but its derivation requires considering the total current in the system and enforcing equation A.4. The current through the *l*th electrode is

$$I_l = \int_{E_l} \frac{1}{z_l} (V_l - u) \, \mathrm{d}S = \frac{1}{z_l} E_l V_l - \int_{E_l} \frac{1}{z_l} u \, \mathrm{d}S. \tag{A.30}$$

Assuming a constant contact impedance and electrode voltage, the first quantity in the right hand side of equation A.30 relates the electrode current to the electrode voltage by E_l/z_l. This accounts for the form of $\mathbf{A}_D$ while the last term in the right hand side of equation A.30 can be recognized as equation A.27 but with the nodal solution instead of the nodal variation. This accounts for the coupling of the domain voltage to the electrode voltage by $\mathbf{A}_W$.

A.4 Matrix Assembly

Local $\mathbf{k}_e$, $\mathbf{A}_Z^{el}$, and $\mathbf{A}_W^{el}$ matrices are assembled into global $\mathbf{A}_M$, $\mathbf{A}_Z$, and $\mathbf{A}_W$ matrices respectively. Assembly of local matrices is most conveniently visualized by considering the assembly of the global nodal variation and the global nodal solution vectors. That is, the vector of nodes belonging to each element is a subset of a global vector of nodes. The global variation vector is $\mathbf{c} = \begin{bmatrix} c^1 & c^2 & \dots & c^n & \dots & c^N \end{bmatrix}$ where c^n corresponds to the nodal variation at the *n*th of N total nodes. Similarly, the global solution vector is $\mathbf{d} = \begin{bmatrix} d^1 & d^2 & \dots & d^n & \dots & d^N \end{bmatrix}$ where d^n corresponds to the nodal solution at the *n*th of N total nodes. The assembly of the global diffusion stiffness matrix can now be expressed as

$$\sum_e \int_{\Omega_e} \frac{\partial \psi_e}{\partial x_i} \sigma_{ij} \frac{\partial u_e}{\partial x_j} \, \mathrm{d}\Omega_e = \mathbf{c}^T \mathbf{A}_M \mathbf{d}. \tag{A.31}$$

Elements of each local diffusion stiffness matrix must be placed in the global matrix such that they still contract out with the appropriate nodal variations and solutions. Because elements may share nodes, some entries to the global matrix will be additive. Consider, for example, the local diffusion stiffness matrices of the eth and the eth$+1$ elements for linear triangles. Furthermore, let the eth and the eth$+1$ elements share a side as shown in Figure A.2.

$$\mathbf{c}_e^T \mathbf{A}_M^e \mathbf{d}_e = \begin{bmatrix} c_e^1 & c_e^2 & c_e^3 \end{bmatrix} \begin{bmatrix} k_e^{11} & k_e^{12} & k_e^{13} \\ k_e^{21} & k_e^{22} & k_e^{23} \\ k_e^{31} & k_e^{32} & k_e^{33} \end{bmatrix} \begin{bmatrix} d_e^1 \\ d_e^2 \\ d_e^3 \end{bmatrix} \tag{A.32}$$

$$\mathbf{c}_{e+1}^T \mathbf{A}_M^{e+1} \mathbf{d}_{e+1} = \begin{bmatrix} c_{e+1}^1 & c_{e+1}^2 & c_{e+1}^3 \end{bmatrix} \begin{bmatrix} k_{e+1}^{11} & k_{e+1}^{12} & k_{e+1}^{13} \\ k_{e+1}^{21} & k_{e+1}^{22} & k_{e+1}^{23} \\ k_{e+1}^{31} & k_{e+1}^{32} & k_{e+1}^{33} \end{bmatrix} \begin{bmatrix} d_{e+1}^1 \\ d_{e+1}^2 \\ d_{e+1}^3 \end{bmatrix} \tag{A.33}$$

Additionally, let the nodes belonging to the eth and eth$+1$ elements corresponding to the following global nodes.

$$\begin{bmatrix} c_e^1 & c_e^2 & c_e^3 \end{bmatrix} \mapsto \begin{bmatrix} c^4 & c^5 & c^6 \end{bmatrix}$$

$$\begin{bmatrix} d_e^1 & d_e^2 & d_e^3 \end{bmatrix} \mapsto \begin{bmatrix} d^4 & d^5 & d^6 \end{bmatrix}$$

$$\begin{bmatrix} c_{e+1}^1 & c_{e+1}^2 & c_{e+1}^3 \end{bmatrix} \mapsto \begin{bmatrix} c^5 & c^7 & c^6 \end{bmatrix}$$

$$\begin{bmatrix} d_{e+1}^1 & d_{e+1}^2 & d_{e+1}^3 \end{bmatrix} \mapsto \begin{bmatrix} d^5 & d^7 & d^6 \end{bmatrix}$$

These local matrices are assembled into the global matrix as follows.

$$\mathbf{c}^T \mathbf{A}_M \mathbf{d} = \begin{bmatrix} \vdots \\ c^4 \\ c^5 \\ c^6 \\ c^7 \\ \vdots \end{bmatrix}^T \begin{bmatrix} & & & \\ k_e^{11} & k_e^{12} & k_e^{13} & \\ k_e^{21} & k_e^{22} + k_{e+1}^{11} & k_e^{23} + k_{e+1}^{12} & k_{e+1}^{13} \\ k_e^{31} & k_e^{32} + k_{e+1}^{21} & k_e^{33} + k_{e+1}^{22} & k_{e+1}^{23} \\ & k_{e+1}^{31} & k_{e+1}^{32} & k_{e+1}^{33} \\ & & & \end{bmatrix} \begin{bmatrix} \vdots \\ d^4 \\ d^5 \\ d^6 \\ d^7 \\ \vdots \end{bmatrix} \tag{A.34}$$

Because the two elements considered share the fifth and sixth global nodes, the corre-

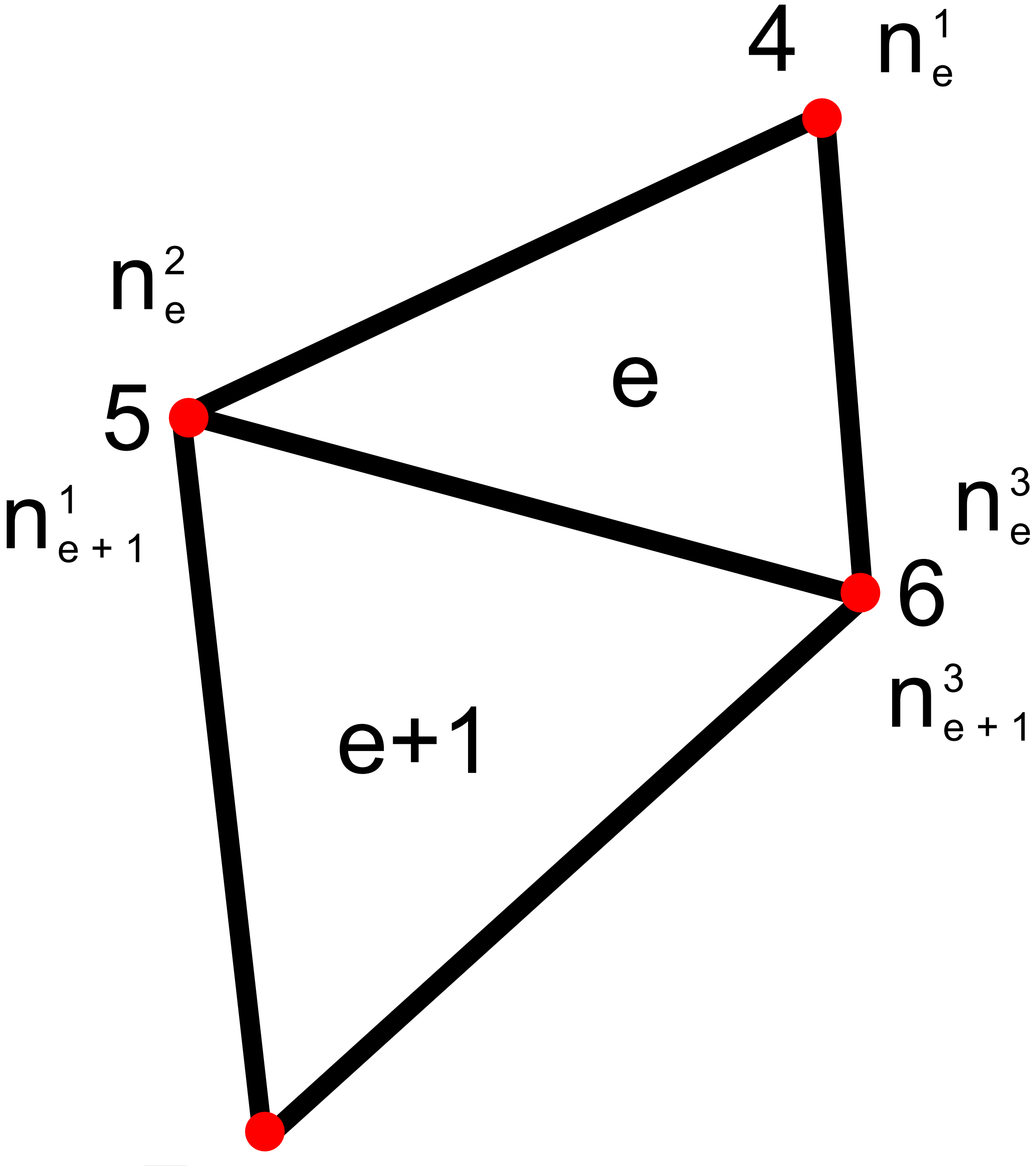

Figure A.2: Two arbitrary triangular elements with local and global nodes labeled.

sponding entries to the global diffusion stiffness matrix has a contribution from each. It is important to remember that this is merely an illustrative example considering two elements in isolation. A real mesh will have more shared entries and local matrices may not be confined to blocks in the global matrix. The assembly process can be automated in a loop with knowledge of the nodal connectivity matrix. The global $\mathbf{A}_Z$ is assembled in an identical manner, and the global $\mathbf{A}_W$ matrix is assembled in a similar manner. The difference is that electrode voltage degrees of freedom must match in the contractions instead of nodal voltage solutions.

A.5 Sparse Indexing in MATLAB

The forward problem and EIT code used in this research was written entirely in MATLAB (The MathWorks Inc., Natick, MA) by the author. The finite element method necessitates the inversion of large matrices. Fortunately, these matrices are sparse and the memory requirements for inversion can be considerably reduced by using the *sparse*( ) command in MATLAB. However, MATLAB has a reputation of being unpalatable for finite element analysis because the manner in which it indexes and populates sparse matrices is very time consuming especially when the *sparse*( ) command is embedded in a loop. Triplet indexing circumvents this. Triplet indexing forms three vectors as matrix entries are calculated – one vector of the row number, one vector for the column number, and one vector for the value of a particular entry. The *sparse*( ) command is not called until the triplet vectors have been populated. This approach enables fine meshes to be solved quite expeditiously in MATLAB.

A.6 Mesh Generation and Post-Processing

Meshing is the process of discretizing a domain into disjoint subsets; that is, breaking a domain into many connected elements. Many commercial and open sources meshers exist, and, in the author's experience, they all have a bit of a learning curve. It is therefore recommended that users find one available to them and then commit to learning it. The author prefers Cubit (Sandia Corporation, Sandia National Laboratories, Albuquerque, NM) where available. Netgen is also a good open source option for tetrahedral elements.

Post-processing is the process of visualizing data. ParaView (Sandia Corporation, Kitware Inc. Sandia National Laboratories, Albuquerque, NM) is a powerful open source post-processor capable of rendering both forward problem solutions and conductivity distributions recovered during the inverse problem. All figures herein, however, were generated via code written by the author in MATLAB.

APPENDIX B

Detailed Sensitivity Matrix Calculations

B.1 Introduction

The sensitivity matrix can look intimidating to the uninitiated, but forming its entries is really no more difficult than forming the finite element stiffness matrix for steady-state diffusion as was presented in Appendix A. Here, the exact form of sensitivity matrix entries will be derived for linear triangle and tetrahedral elements, but, again, it is a easy extension to quadrilateral or hexahedral elements. This will also be put in the context of some psuedo-code necessary to build up the entire matrix.

B.2 Evaluation of the Sensitivity Matrix Entries

Begin by recalling the form of the sensitivity matrix for anisotropic conductivity. This simplifies to the isotropic case when δ_{ij} is substituted for σ_{ij}. Note, also, that the superscript 0 has been dropped from σ_{ij} for notational convenience.

$$J_{QR\,e} = -\int_{\Omega_e} \frac{\partial u^Q}{\partial x_i} \sigma_{ij} \frac{\partial \bar{u}^R}{\partial x_j} \mathrm{d}\Omega_e \tag{B.1}$$

Again, repeated subscripts imply summation over the domain of the problem. Also note that now QR is an index of the sensitivity matrix instead of the previously used MN. This is just to avoid using the same indices as are used to sum over the number of nodes per element. Just as in the formulation of the finite element matrices, proceed by substituting the explicit forms for u shown in equation A.10.

$$
\begin{aligned}
J_{QR\,e} &= -\int_{\Omega_e} \frac{\partial u^Q}{\partial x_i}\sigma_{ij}\frac{\partial \bar{u}^R}{\partial x_j}\mathrm{d}\Omega_e \\
&= -\sum_{A=1}^{N}\sum_{B=1}^{N} d_e^{A\,Q} \int_{\Omega_e} \frac{\partial w^A}{\partial x_i}\sigma_{ij}\frac{\partial w^B}{\partial x_j}\,\mathrm{d}\Omega_e\,\bar{d}_e^{B\,R}
\end{aligned} \tag{B.2}
$$

$d_e^{A\,Q}$ refers to the *A*th nodal solution of the *e*th element due to the *Q*th injection, and $\bar{d}_e^{B\,R}$ refers to the *B*th nodal solution of the *e*th element due to a unit current injection by the *R*th electrode measurement pair. Now the gradients of the interpolations functions can be evaluated via the chain rule as in equation A.14.

$$
-\int_{\Omega_e} \frac{\partial u^Q}{\partial x_i}\sigma_{ij}\frac{\partial \bar{u}^R}{\partial x_j}\mathrm{d}\Omega_e = -\sum_{A=1}^{N}\sum_{B=1}^{N} d_e^{A\,Q} \int_{\Omega_e} \frac{\partial w^A}{\partial \zeta_k}\frac{\partial \zeta_k}{\partial x_i}\sigma_{ij}\frac{\partial w^B}{\partial \zeta_l}\frac{\partial \zeta_l}{\partial x_j}\,\mathrm{d}\Omega_e\,\bar{d}_e^{B\,R} \tag{B.3}
$$

This integral is then carried out in the isoparametric domain by multiplying it by $\det|\partial x_i/\partial \zeta_j|$.

$$
-\int_{\Omega_e} \frac{\partial u^Q}{\partial x_i}\sigma_{ij}\frac{\partial \bar{u}^R}{\partial x_j}\mathrm{d}\Omega_e = -\sum_{A=1}^{N}\sum_{B=1}^{N} d_e^{A\,Q} \int_{\Omega_{e_\zeta}} \frac{\partial w^A}{\partial \zeta_k}\frac{\partial \zeta_k}{\partial x_i}\sigma_{ij}\frac{\partial w^B}{\partial \zeta_l}\frac{\partial \zeta_l}{\partial x_j}\det\left|\frac{\partial x_m}{\partial \zeta_n}\right|\,\mathrm{d}\Omega_e\,\bar{d}_e^{B\,R} \tag{B.4}
$$

Now express the summations through linear algebra.

$$
\begin{aligned}
-\int_{\Omega_e} \frac{\partial u^Q}{\partial x_i}\sigma_{ij}\frac{\partial \bar{u}^R}{\partial x_j}\mathrm{d}\Omega_e &= \sum_{A=1}^{N}\sum_{B=1}^{N} d_e^{A\,Q} j_e^{AB} d_e^{B\,R} \\
&= \begin{bmatrix} d_e^{1\,Q} & d_e^{2\,Q} & \dots & d_e^{N\,Q} \end{bmatrix} \mathbf{j}_e \begin{bmatrix} \bar{d}_e^{1\,R} \\ \bar{d}_e^{2\,R} \\ \vdots \\ \bar{d}_e^{N\,R} \end{bmatrix}
\end{aligned} \tag{B.5}
$$

$\mathbf{j}_e$ can now be evaluate for triangular elements.

$$\mathbf{j}_e = -\frac{1}{2}\begin{bmatrix}1 & 0\\ 0 & 1\\ -1 & -1\end{bmatrix}\begin{bmatrix}x_1^e - x_3^e & x_2^e - x_3^e\\ y_1^e - y_3^e & y_2^e - y_3^e\end{bmatrix}^{-1}\begin{bmatrix}\sigma_{11} & \sigma_{12}\\ \sigma_{21} & \sigma_{22}\end{bmatrix}\cdots$$

$$\cdots\begin{bmatrix}x_1^e - x_3^e & x_2^e - x_3^e\\ y_1^e - y_3^e & y_2^e - y_3^e\end{bmatrix}^{-T}\begin{bmatrix}1 & 0\\ 0 & 1\\ -1 & -1\end{bmatrix}^{T}\det\left|\begin{bmatrix}x_1^e - x_3^e & x_2^e - x_3^e\\ y_1^e - y_3^e & y_2^e - y_3^e\end{bmatrix}\right| \tag{B.6}$$

Similarly for tetrahedral elements.

$$\mathbf{j}_e = -\frac{1}{6}\begin{bmatrix}1 & 0 & 0\\ 0 & 1 & 0\\ 0 & 0 & 1\\ -1 & -1 & -1\end{bmatrix}\begin{bmatrix}x_1^e - x_4^e & x_2^e - x_4^e & x_3^e - x_4^e\\ y_1^e - y_4^e & y_2^e - y_4^e & y_3^e - y_4^e\\ z_1^e - z_4^e & z_2^e - z_4^e & z_3^e - z_4^e\end{bmatrix}^{-1}\cdots$$

$$\cdots\begin{bmatrix}\sigma_{11} & \sigma_{12} & \sigma_{13}\\ \sigma_{21} & \sigma_{22} & \sigma_{23}\\ \sigma_{31} & \sigma_{32} & \sigma_{33}\end{bmatrix}\begin{bmatrix}x_1^e - x_4^e & x_2^e - x_4^e & x_3^e - x_4^e\\ y_1^e - y_4^e & y_2^e - y_4^e & y_3^e - y_4^e\\ z_1^e - z_4^e & z_2^e - z_4^e & z_3^e - z_4^e\end{bmatrix}^{-T}\cdots$$

$$\cdots\begin{bmatrix}1 & 0 & 0\\ 0 & 1 & 0\\ 0 & 0 & 1\\ -1 & -1 & -1\end{bmatrix}^{T}\det\left|\begin{bmatrix}x_1^e - x_4^e & x_2^e - x_4^e & x_3^e - x_4^e\\ y_1^e - y_4^e & y_2^e - y_4^e & y_3^e - y_4^e\\ z_1^e - z_4^e & z_2^e - z_4^e & z_3^e - z_4^e\end{bmatrix}\right| \tag{B.7}$$

These matrices are of course identical to equation A.19 and equation A.20, but they were derived just to solidify that the evaluation of the sensitivity matrix really is quite straight-forward. The major difference is that each entry calculated in the sensitivity matrix is a scalar, not a matrix like in the formation of the diffusion stiffness matrix. This is because the nodal solutions $d_e^{A\,Q}$ and $\bar{d}_e^{B\,R}$ are known vectors so the linear algebra shown in equation B.6 now results in a scalar whereas in the formation of the diffusion stiffness matrices the contracting vectors were either variations to be minimized or solutions to be recovered.

B.3 Indexing the Sensitivity Matrix

Indexing the sensitivity matrix is often counter-intuitive due to the QR index of J_{QRe}. Here, the structure used in this research to populate the sensitivity matrix will be presented as pseudo-code. Casual MATLAB-esque language will be used. As before, let L be the total number of electrodes, E be the total number of elements in the mesh, and N be the number of nodes per element.

```
begin sensitivity matrix

solve forward problem for prescribed current injections between all electrode pairs, save domain solutions

solve forward problem for unit current injections between all electrode pairs, save domain solutions

initialize sensitivity matrix, $\mathbf{J}$ =zeros($L^2$,$E$)

initialize indexing counter, $l = 0$

for $i = 1 : L$

    for $j = 1 : L$

    $l = l + 1$

        for $k = 1 : E$

            recall $[d_k^{1\,i}\, d_k^{2\,i}\, \ldots\, d_k^{N\,i}]$

            recall $[\bar{d}_k^{1\,j}\, \bar{d}_k^{2\,j}\, \ldots\, \bar{d}_k^{N\,j}]$

            find the coordinates of the nodes belonging to the kth element

            evaluate equation B.6 or equation B.7
```

```
            evaluate equation B.5, store as $J_{ij\,k}$
            update $\mathbf{J}$ as $J(l,k) = J(l,k) + J_{ij\,k}$
        end for $k = 1 : E$
    end for $j = 1 : L$
end for $i = 1 : L$
end sensitivity matrix
```

The author is not a computer scientist so there are most certainly more efficient ways of populating the sensitivity matrix. However, it is hoped that the pseudo-code provided will be sufficient as a starting point.

BIBLIOGRAPHY

[1] Kuan, H.-C., Ma, C.-C. M., Chang, W.-P., Yuen, S.-M., Wu, H.-H., and Lee, T.-M., "Synthesis, thermal, mechanical and rheological properties of multiwall carbon nanotube/waterborne polyurethane nanocomposite," *Composites Science and Technology*, Vol. 65, No. 11, 2005, pp. 1703–1710.

[2] Ma, P.-C., Liu, M.-Y., Zhang, H., Wang, S.-Q., Wang, R., Wang, K., Wong, Y.-K., Tang, B.-Z., Hong, S.-H., Paik, K.-W., et al., "Enhanced electrical conductivity of nanocomposites containing hybrid fillers of carbon nanotubes and carbon black," *ACS applied materials & interfaces*, Vol. 1, No. 5, 2009, pp. 1090–1096.

[3] Zhang, D., Ye, L., Wang, D., Tang, Y., Mustapha, S., and Chen, Y., "Assessment of transverse impact damage in GF/EP laminates of conductive nanoparticles using electrical resistivity tomography," *Composites Part A: Applied Science and Manufacturing*, Vol. 43, No. 9, 2012, pp. 1587–1598.

[4] Viets, C., Kaysser, S., and Schulte, K., "Damage mapping of GFRP via electrical resistance measurements using nanocomposite epoxy matrix systems," *Composites Part B: Engineering*, 2013.

[5] Naghashpour, A. and Van Hoa, S., "A technique for real-time detecting, locating, and quantifying damage in large polymer composite structures made of carbon fibers and carbon nanotube networks," *Structural Health Monitoring*, Vol. 14, No. 1, 2015, pp. 35–45.

[6] Hou, T.-C., Loh, K. J., and Lynch, J. P., "Spatial conductivity mapping of carbon nanotube composite thin films by electrical impedance tomography for sensing applications," *Nanotechnology*, Vol. 18, No. 31, 2007, pp. 315501.

[7] Hu, N., Karube, Y., Arai, M., Watanabe, T., Yan, C., Li, Y., Liu, Y., and Fukunaga, H., "Investigation on sensitivity of a polymer/carbon nanotube composite strain sensor," *Carbon*, Vol. 48, No. 3, 2010, pp. 680–687.

[8] Isaacson, D., Mueller, J. L., Newell, J. C., and Siltanen, S., "Reconstructions of chest phantoms by the D-bar method for electrical impedance tomography," *Medical Imaging, IEEE Transactions on*, Vol. 23, No. 7, 2004, pp. 821–828.

[9] Chakraborty, D., "Delamination of laminated fiber reinforced plastic composites under multiple cylindrical impact," *Materials & design*, Vol. 28, No. 4, 2007, pp. 1142–1153.

[10] Abrate, S., *Impact engineering of composite structures*, Vol. 526, Springer, 2011.

[11] Carden, E. P. and Fanning, P., “Vibration based condition monitoring: a review,” *Structural Health Monitoring*, Vol. 3, No. 4, 2004, pp. 355–377.

[12] Montalvão, D., Maia, N. M. M., and Ribeiro, A. M. R., “A review of vibration-based structural health monitoring with special emphasis on composite materials,” *Shock and Vibration Digest*, Vol. 38, No. 4, 2006, pp. 295–326.

[13] Leng, J. and Asundi, A., “Structural health monitoring of smart composite materials by using EFPI and FBG sensors,” *Sensors and Actuators A: Physical*, Vol. 103, No. 3, 2003, pp. 330–340.

[14] Lee, B., “Review of the present status of optical fiber sensors,” *Optical Fiber Technology*, Vol. 9, No. 2, 2003, pp. 57–79.

[15] Abot, J. L., Song, Y., Vatsavaya, M. S., Medikonda, S., Kier, Z., Jayasinghe, C., Rooy, N., Shanov, V. N., and Schulz, M. J., “Delamination detection with carbon nanotube thread in self-sensing composite materials,” *Composites Science and Technology*, Vol. 70, No. 7, 2010, pp. 1113–1119.

[16] Raghavan, A. and Cesnik, C. E., “Review of guided-wave structural health monitoring,” *Shock and Vibration Digest*, Vol. 39, No. 2, 2007, pp. 91–116.

[17] Raghavan, A., *Guided-wave structural health monitoring*, Ph.D. thesis, The University of Michigan, 2007.

[18] de Villoria, R. G., Yamamoto, N., Miravete, A., and Wardle, B. L., “Multiphysics damage sensing in nano-engineered structural composites,” *Nanotechnology*, Vol. 22, No. 18, 2011, pp. 185502.

[19] Thiagarajan, C., Sturland, I. M., Tunnicliffe, D. L., and Irving, P., “Electrical potential techniques for damage sensing in composite structures,” *Smart Structures and Materials: Second European Conference*, International Society for Optics and Photonics, 1994, pp. 128–131.

[20] Schulte, K. and Baron, C., “Load and failure analyses of CFRP laminates by means of electrical resistivity measurements,” *Composites Science and Technology*, Vol. 36, No. 1, 1989, pp. 63–76.

[21] Lange, R. and Mook, G., “Structural analysis of CFRP using eddy current methods,” *NDT & E International*, Vol. 27, No. 5, 1994, pp. 241–248.

[22] Mook, G., Lange, R., and Koeser, O., “Non-destructive characterisation of carbon-fibre-reinforced plastics by means of eddy-currents,” *Composites science and technology*, Vol. 61, No. 6, 2001, pp. 865–873.

[23] Yin, W., Withers, P. J., Sharma, U., and Peyton, A. J., "Noncontact characterization of carbon-fiber-reinforced plastics using multifrequency eddy current sensors," *Instrumentation and Measurement, IEEE Transactions on*, Vol. 58, No. 3, 2009, pp. 738–743.

[24] Zhu, Y., Bakis, C. E., and Adair, J. H., "Effects of carbon nanofiller functionalization and distribution on interlaminar fracture toughness of multi-scale reinforced polymer composites," *Carbon*, Vol. 50, No. 3, 2012, pp. 1316–1331.

[25] Tsantzalis, S., Karapappas, P., Vavouliotis, A., Tsotra, P., Kostopoulos, V., Tanimoto, T., and Friedrich, K., "On the improvement of toughness of CFRPs with resin doped with CNF and PZT particles," *Composites Part A: Applied Science and Manufacturing*, Vol. 38, No. 4, 2007, pp. 1159–1162.

[26] Arai, M., Noro, Y., Sugimoto, K.-i., and Endo, M., "Mode I and mode II interlaminar fracture toughness of CFRP laminates toughened by carbon nanofiber interlayer," *Composites Science and Technology*, Vol. 68, No. 2, 2008, pp. 516–525.

[27] Thostenson, E. T., Li, C., and Chou, T.-W., "Nanocomposites in context," *Composites Science and Technology*, Vol. 65, No. 3, 2005, pp. 491–516.

[28] Iijima, S. et al., "Helical microtubules of graphitic carbon," *nature*, Vol. 354, No. 6348, 1991, pp. 56–58.

[29] Al-Saleh, M. H. and Sundararaj, U., "Review of the mechanical properties of carbon nanofiber/polymer composites," *Composites Part A: Applied Science and Manufacturing*, Vol. 42, No. 12, 2011, pp. 2126–2142.

[30] Lau, A. K.-T. and Hui, D., "The revolutionary creation of new advanced materials-carbon nanotube composites," *Composites Part B: Engineering*, Vol. 33, No. 4, 2002, pp. 263–277.

[31] Ebbesen, T., Lezec, H., Hiura, H., Bennett, J., Ghaemi, H., and Thio, T., "Electrical conductivity of individual carbon nanotubes," 1996.

[32] Gungor, S., *Electric-Field-Induced Alignment of Carbon Nanofillers in Multifunctional Glass-Epoxy Composites*, Ph.D. thesis, The Pennsylvania State University, December 2013.

[33] Thostenson, E. T., Ren, Z., and Chou, T.-W., "Advances in the science and technology of carbon nanotubes and their composites: a review," *Composites science and technology*, Vol. 61, No. 13, 2001, pp. 1899–1912.

[34] Böger, L., Wichmann, M. H., Meyer, L. O., and Schulte, K., "Load and health monitoring in glass fibre reinforced composites with an electrically conductive nanocomposite epoxy matrix," *Composites Science and Technology*, Vol. 68, No. 7, 2008, pp. 1886–1894.

[35] Nofar, M., Hoa, S., and Pugh, M., "Failure detection and monitoring in polymer matrix composites subjected to static and dynamic loads using carbon nanotube networks," *Composites Science and Technology*, Vol. 69, No. 10, 2009, pp. 1599–1606.

[36] Thostenson, E. T. and Chou, T.-W., "Real-time in situ sensing of damage evolution in advanced fiber composites using carbon nanotube networks," *Nanotechnology*, Vol. 19, No. 21, 2008, pp. 215713.

[37] Loh, K. J., Hou, T.-C., Lynch, J. P., and Kotov, N. A., "Carbon nanotube sensing skins for spatial strain and impact damage identification," *Journal of Nondestructive Evaluation*, Vol. 28, No. 1, 2009, pp. 9–25.

[38] Hu, N., Karube, Y., Yan, C., Masuda, Z., and Fukunaga, H., "Tunneling effect in a polymer/carbon nanotube nanocomposite strain sensor," *Acta Materialia*, Vol. 56, No. 13, 2008, pp. 2929–2936.

[39] Zhang, W., Suhr, J., and Koratkar, N., "Carbon nanotube/polycarbonate composites as multifunctional strain sensors," *Journal of Nanoscience and Nanotechnology*, Vol. 6, No. 4, 2006, pp. 960–964.

[40] Zhou, X., Shin, E., Wang, K., and Bakis, C., "Interfacial damping characteristics of carbon nanotube-based composites," *Composites Science and Technology*, Vol. 64, No. 15, 2004, pp. 2425–2437.

[41] Liu, A., Wang, K., and Bakis, C. E., "Effect of functionalization of single-wall carbon nanotubes (SWNTs) on the damping characteristics of SWNT-based epoxy composites via multiscale analysis," *Composites Part A: Applied Science and Manufacturing*, Vol. 42, No. 11, 2011, pp. 1748–1755.

[42] Liu, A., Wang, K., and Bakis, C. E., "Multiscale damping model for polymeric composites containing carbon nanotube ropes," *Journal of Composite Materials*, Vol. 44, No. 19, 2010, pp. 2301–2323.

[43] Bauhofer, W. and Kovacs, J. Z., "A review and analysis of electrical percolation in carbon nanotube polymer composites," *Composites Science and Technology*, Vol. 69, No. 10, 2009, pp. 1486–1498.

[44] Grossiord, N., Loos, J., Van Laake, L., Maugey, M., Zakri, C., Koning, C. E., and Hart, A. J., "High-Conductivity Polymer Nanocomposites Obtained by Tailoring the Characteristics of Carbon Nanotube Fillers," *Advanced Functional Materials*, Vol. 18, No. 20, 2008, pp. 3226–3234.

[45] Sandler, J., Shaffer, M., Prasse, T., Bauhofer, W., Schulte, K., and Windle, A., "Development of a dispersion process for carbon nanotubes in an epoxy matrix and the resulting electrical properties," *Polymer*, Vol. 40, No. 21, 1999, pp. 5967–5971.

[46] Gojny, F., Wichmann, M., Köpke, U., Fiedler, B., and Schulte, K., "Carbon nanotube-reinforced epoxy-composites: enhanced stiffness and fracture toughness

at low nanotube content," *Composites Science and Technology*, Vol. 64, No. 15, 2004, pp. 2363–2371.

[47] Tibbetts, G. G. and McHugh, J. J., "Mechanical properties of vapor-grown carbon fiber composites with thermoplastic matrices," *Journal of Materials Research*, Vol. 14, No. 07, 1999, pp. 2871–2880.

[48] Bal, S., "Experimental study of mechanical and electrical properties of carbon nanofiber/epoxy composites," *Materials & Design*, Vol. 31, No. 5, 2010, pp. 2406–2413.

[49] Lozano, K. and Barrera, E., "Nanofiber-reinforced thermoplastic composites. I. Thermoanalytical and mechanical analyses," *Journal of Applied Polymer Science*, Vol. 79, No. 1, 2001, pp. 125–133.

[50] Hu, N., Masuda, Z., Yamamoto, G., Fukunaga, H., Hashida, T., and Qiu, J., "Effect of fabrication process on electrical properties of polymer/multi-wall carbon nanotube nanocomposites," *Composites Part A: Applied Science and Manufacturing*, Vol. 39, No. 5, 2008, pp. 893–903.

[51] Sandler, J., Kirk, J., Kinloch, I., Shaffer, M., and Windle, A., "Ultra-low electrical percolation threshold in carbon-nanotube-epoxy composites," *Polymer*, Vol. 44, No. 19, 2003, pp. 5893–5899.

[52] Huang, J.-C., "Carbon black filled conducting polymers and polymer blends," *Advances in Polymer Technology*, Vol. 21, No. 4, 2002, pp. 299–313.

[53] Thostenson, E. T. and Chou, T.-W., "Carbon nanotube networks: sensing of distributed strain and damage for life prediction and self healing," *Advanced Materials*, Vol. 18, No. 21, 2006, pp. 2837–2841.

[54] Gao, L., Thostenson, E. T., Zhang, Z., and Chou, T.-W., "Coupled carbon nanotube network and acoustic emission monitoring for sensing of damage development in composites," *Carbon*, Vol. 47, No. 5, 2009, pp. 1381–1388.

[55] Kim, K. J., Yu, W.-R., Lee, J. S., Gao, L., Thostenson, E. T., Chou, T.-W., and Byun, J.-H., "Damage characterization of 3D braided composites using carbon nanotube-based in situ sensing," *Composites Part A: Applied Science and Manufacturing*, Vol. 41, No. 10, 2010, pp. 1531–1537.

[56] Gao, L., Chou, T.-W., Thostenson, E. T., and Zhang, Z., "A comparative study of damage sensing in fiber composites using uniformly and non-uniformly dispersed carbon nanotubes," *Carbon*, Vol. 48, No. 13, 2010, pp. 3788–3794.

[57] Gao, L., Chou, T.-W., Thostenson, E. T., Zhang, Z., and Coulaud, M., "In situ sensing of impact damage in epoxy/glass fiber composites using percolating carbon nanotube networks," *Carbon*, Vol. 49, No. 10, 2011, pp. 3382–3385.

[58] Pedrazzoli, D., Dorigato, A., and Pegoretti, A., "Monitoring the mechanical behavior under ramp and creep conditions of electrically conductive polymer composites," *Composites Part A: Applied Science and Manufacturing*, Vol. 43, No. 8, 2012, pp. 1285–1292.

[59] Naghashpour, A. and Van Hoa, S., "A technique for real-time detection, location and quantification of damage in large polymer composite structures made of electrically non-conductive fibers and carbon nanotube networks," *Nanotechnology*, Vol. 24, No. 45, 2013, pp. 455502.

[60] Loyola, B. R., Briggs, T. M., Arronche, L., Loh, K. J., La Saponara, V., O'Bryan, G., and Skinner, J. L., "Detection of spatially distributed damage in fiber-reinforced polymer composites," *Structural Health Monitoring*, Vol. 12, No. 3, 2013, pp. 225–239.

[61] Holder, D. S., *Electrical impedance tomography: methods, history and applications*, CRC Press, 2004.

[62] Calderón, A. P., "On an inverse boundary value problem," *Computational & Applied Mathematics*, Vol. 25, No. 2-3, 2006, pp. 133–138.

[63] Loke, M. and Barker, R., "Practical techniques for 3D resistivity surveys and data inversion," *Geophysical prospecting*, Vol. 44, No. 3, 1996, pp. 499–523.

[64] Loke, M. H. and Barker, R., "Rapid least-squares inversion of apparent resistivity pseudosections by a quasi-Newton method," *Geophysical prospecting*, Vol. 44, No. 1, 1996, pp. 131–152.

[65] Brown, B. H., "Medical impedance tomography and process impedance tomography: a brief review," *Measurement Science and Technology*, Vol. 12, No. 8, 2001, pp. 991.

[66] Holder, D., *Clinical and physiological applications of electrical impedance tomography*, CRC Press, 1993.

[67] Henderson, R. P. and Webster, J. G., "An impedance camera for spatially specific measurements of the thorax," *Biomedical Engineering, IEEE Transactions on*, , No. 3, 1978, pp. 250–254.

[68] Barber, D., Brown, B., and Freeston, I., "Imaging spatial distributions of resistivity using applied potential tomography: APT," *Information Processing in Medical Imaging*, Springer, 1984, pp. 446–462.

[69] Yorkey, T. J., Webster, J. G., and Tompkins, W. J., "Comparing reconstruction algorithms for electrical impedance tomography," *Biomedical Engineering, IEEE Transactions on*, , No. 11, 1987, pp. 843–852.

[70] Cheney, M., Isaacson, D., and Newell, J. C., "Electrical impedance tomography," *SIAM review*, Vol. 41, No. 1, 1999, pp. 85–101.

[71] Dobson, D. C., "Convergence of a reconstruction method for the inverse conductivity problem," *SIAM Journal on Applied Mathematics*, Vol. 52, No. 2, 1992, pp. 442–458.

[72] Adler, A. and Guardo, R., "Electrical impedance tomography: regularized imaging and contrast detection," *Medical Imaging, IEEE Transactions on*, Vol. 15, No. 2, 1996, pp. 170–179.

[73] Dobson, D. C., "Recovery of blocky images in electrical impedance tomography," *Inverse problems in medical imaging and nondestructive testing*, Springer, 1997, pp. 43–64.

[74] Borsic, A., Graham, B. M., Adler, A., and Lionheart, W., "In vivo impedance imaging with total variation regularization," *Medical Imaging, IEEE Transactions on*, Vol. 29, No. 1, 2010, pp. 44–54.

[75] Andersen, K. D., Christiansen, E., Conn, A. R., and Overton, M. L., "An efficient primal-dual interior-point method for minimizing a sum of Euclidean norms," *SIAM Journal on Scientific Computing*, Vol. 22, No. 1, 2000, pp. 243–262.

[76] Chan, T. F., Golub, G. H., and Mulet, P., "A nonlinear primal-dual method for total variation-based image restoration," *SIAM Journal on Scientific Computing*, Vol. 20, No. 6, 1999, pp. 1964–1977.

[77] Hallaji, M., Seppänen, A., and Pour-Ghaz, M., "Electrical impedance tomography-based sensing skin for quantitative imaging of damage in concrete," *Smart Materials and Structures*, Vol. 23, No. 8, 2014, pp. 085001.

[78] Cattin, C. and Hubert, P., "Piezoresistance in Polymer Nanocomposites with High Aspect Ratio Particles," *ACS applied materials & interfaces*, Vol. 6, No. 3, 2014, pp. 1804–1811.

[79] Sharma, A., Bakis, C., and Wang, K., "A new method of chaining carbon nanofibers in epoxy," *Nanotechnology*, Vol. 19, No. 32, 2008, pp. 325606.

[80] Thostenson, E. T. and Chou, T.-W., "Aligned multi-wall carbon nanotube-reinforced composites: processing and mechanical characterization," *J. Phys. D: Appl. Phys.*, Vol. 35, No. 10, 2002, pp. 77–80.

[81] Gungor, S. and Bakis, C. E., "Anisotropic networking of carbon black in glass/epoxy composites using electric field," *Journal of Composite Materials*, 2014, pp. 0021998314521256.

[82] Domingues, D., Logakis, E., and Skordos, A., "The use of an electric field in the preparation of glass fibre/epoxy composites containing carbon nanotubes," *Carbon*, Vol. 50, No. 7, 2012, pp. 2493–2503.

[83] Loh, K. J., Lynch, J. P., Shim, B., and Kotov, N., "Tailoring piezoresistive sensitivity of multilayer carbon nanotube composite strain sensors," *Journal of Intelligent Material Systems and Structures*, Vol. 19, No. 7, 2008, pp. 747–764.

[84] Cardoso, P., Silva, J., Agostinho Moreira, J., Klosterman, D., van Hattum, F., Simoes, R., and Lanceros-Mendez, S., "Temperature dependence of the electrical conductivity of vapor grown carbon nanofiber/epoxy composites with different filler dispersion levels," *Physics Letters A*, Vol. 376, No. 45, 2012, pp. 3290–3294.

[85] Kumar, S., Rath, T., Mahaling, R., Reddy, C., Das, C., Pandey, K., Srivastava, R., and Yadaw, S., "Study on mechanical, morphological and electrical properties of carbon nanofiber/polyetherimide composites," *Materials Science and Engineering: B*, Vol. 141, No. 1, 2007, pp. 61–70.

[86] Mei, Q., Wang, J., Wang, F., Huang, Z., Yang, X., and Wei, T., "Conductive behaviors of carbon nanofibers reinforced epoxy composites," *Journal of Wuhan University of Technology-Mater. Sci. Ed.*, Vol. 23, No. 1, 2008, pp. 139–142.

[87] Simmons, J. G., "Generalized formula for the electric tunnel effect between similar electrodes separated by a thin insulating film," *Journal of Applied Physics*, Vol. 34, No. 6, 2004, pp. 1793–1803.

[88] Taya, M., Kim, W., and Ono, K., "Piezoresistivity of a short fiber/elastomer matrix composite," *Mechanics of materials*, Vol. 28, No. 1, 1998, pp. 53–59.

[89] Rahman, R. and Servati, P., "Effects of inter-tube distance and alignment on tunnelling resistance and strain sensitivity of nanotube/polymer composite films," *Nanotechnology*, Vol. 23, No. 5, 2012, pp. 055703.

[90] Deng, F. and Zheng, Q.-S., "An analytical model of effective electrical conductivity of carbon nanotube composites," *Applied Physics Letters*, Vol. 92, No. 7, 2008, pp. 071902.

[91] Takeda, T., Shindo, Y., Kuronuma, Y., and Narita, F., "Modeling and characterization of the electrical conductivity of carbon nanotube-based polymer composites," *Polymer*, Vol. 52, No. 17, 2011, pp. 3852–3856.

[92] Lu, C. and Mai, Y.-W., "Anomalous electrical conductivity and percolation in carbon nanotube composites," *Journal of Materials Science*, Vol. 43, No. 17, 2008, pp. 6012–6015.

[93] Kirkpatrick, S., "Percolation and conduction," *Reviews of modern physics*, Vol. 45, No. 4, 1973, pp. 574.

[94] Grillard, F., Jaillet, C., Zakri, C., Miaudet, P., Derré, A., Korzhenko, A., Gaillard, P., and Poulin, P., "Conductivity and percolation of nanotube based polymer composites in extensional deformations," *Polymer*, Vol. 53, No. 1, 2012, pp. 183–187.

[95] Du, F., Fischer, J. E., and Winey, K. I., “Effect of nanotube alignment on percolation conductivity in carbon nanotube/polymer composites,” *Departmental Papers (MSE)*, 2005, pp. 79.

[96] Zeng, X., Xu, X., Shenai, P. M., Kovalev, E., Baudot, C., Mathews, N., and Zhao, Y., “Characteristics of the electrical percolation in carbon nanotubes/polymer nanocomposites,” *The Journal of Physical Chemistry C*, Vol. 115, No. 44, 2011, pp. 21685–21690.

[97] Celzard, A., McRae, E., Deleuze, C., Dufort, M., Furdin, G., and Marêché, J., “Critical concentration in percolating systems containing a high-aspect-ratio filler,” *Physical Review B*, Vol. 53, 1996, pp. 6209–6214.

[98] Balberg, I., Anderson, C., Alexander, S., and Wagner, N., “Excluded volume and its relation to the onset of percolation,” *Physical review B*, Vol. 30, No. 7, 1984, pp. 3933.

[99] Yu, Y., Song, G., and Sun, L., “Determinant role of tunneling resistance in electrical conductivity of polymer composites reinforced by well dispersed carbon nanotubes,” *Journal of Applied Physics*, Vol. 108, No. 8, 2010, pp. 084319.

[100] Song, Y. S. and Youn, J. R., “Modeling of effective elastic properties for polymer based carbon nanotube composites,” *Polymer*, Vol. 47, No. 5, 2006, pp. 1741–1748.

[101] Kang, I., Schulz, M. J., Kim, J. H., Shanov, V., and Shi, D., “A carbon nanotube strain sensor for structural health monitoring,” *Smart materials and structures*, Vol. 15, No. 3, 2006, pp. 737.

[102] Dalmas, F., Dendievel, R., Chazeau, L., Cavaillé, J.-Y., and Gauthier, C., “Carbon nanotube-filled polymer composites. Numerical simulation of electrical conductivity in three-dimensional entangled fibrous networks,” *Acta materialia*, Vol. 54, No. 11, 2006, pp. 2923–2931.

[103] Bao, W., Meguid, S., Zhu, Z., and Meguid, M., “Modeling electrical conductivities of nanocomposites with aligned carbon nanotubes,” *Nanotechnology*, Vol. 22, No. 48, 2011, pp. 485704.

[104] Bao, W., Meguid, S., Zhu, Z., Pan, Y., and Weng, G., “A novel approach to predict the electrical conductivity of multifunctional nanocomposites,” *Mechanics of Materials*, Vol. 46, 2012, pp. 129–138.

[105] Li, C., Thostenson, E. T., and Chou, T.-W., “Dominant role of tunneling resistance in the electrical conductivity of carbon nanotube–based composites,” *Applied Physics Letters*, Vol. 91, No. 22, 2007, pp. 223114.

[106] Thostenson, E. T., Gangloff Jr, J. J., Li, C., and Byun, J.-H., “Electrical anisotropy in multiscale nanotube/fiber hybrid composites,” *Applied physics letters*, Vol. 95, No. 7, 2009, pp. 073111.

[107] Li, C. and Chou, T.-W., "Electrical conductivities of composites with aligned carbon nanotubes," *Journal of nanoscience and nanotechnology*, Vol. 9, No. 4, 2009, pp. 2518–2524.

[108] Hu, N., Masuda, Z., Yan, C., Yamamoto, G., Fukunaga, H., and Hashida, T., "The electrical properties of polymer nanocomposites with carbon nanotube fillers," *Nanotechnology*, Vol. 19, No. 21, 2008, pp. 215701.

[109] White, S. I., DiDonna, B. A., Mu, M., Lubensky, T. C., and Winey, K. I., "Simulations and electrical conductivity of percolated networks of finite rods with various degrees of axial alignment," *Physical Review B*, Vol. 79, No. 2, 2009, pp. 024301.

[110] Gong, S. and Zhu, Z. H., "On the mechanism of piezoresistivity of carbon nanotube polymer composites," *Polymer*, Vol. 55, No. 16, 2014, pp. 4136–4149.

[111] Ono, U., Aoki, T., and Ogasawara, T., "Mechanical and electrical properties of carbon nanotube based composites," *Proceedings of the 48th conference on structures strength*, 2006, pp. 141–143.

[112] Horikawamachi, Saiwai-ku, shi, K., and Kanazawa, "Research Report," Tech. rep., Nano Carbon Technologies Co., Ltd, 2004.

[113] Pipes, R. B., Frankland, S., Hubert, P., and Saether, E., "Self-consistent properties of carbon nanotubes and hexagonal arrays as composite reinforcements," *Composites Science and Technology*, Vol. 63, No. 10, 2003, pp. 1349–1358.

[114] Balberg, I., Binenbaum, N., and Wagner, N., "Percolation thresholds in the three-dimensional sticks system," *Physical Review Letters*, Vol. 52, No. 17, 1984, pp. 1465.

[115] Loyola, B. R., La Saponara, V., and Loh, K. J., "In situ strain monitoring of fiber-reinforced polymers using embedded piezoresistive nanocomposites," *Journal of materials science*, Vol. 45, No. 24, 2010, pp. 6786–6798.

[116] Yakuphanoglu, F., Yahia, I., Barim, G., and Filiz Senkal, B., "Double-walled carbon nanotube/polymer nanocomposites: Electrical properties under dc and ac fields," *Synthetic Metals*, Vol. 160, No. 15, 2010, pp. 1718–1726.

[117] Loh, K. J., Kim, J., Lynch, J. P., Kam, N. W. S., and Kotov, N. A., "Multifunctional layer-by-layer carbon nanotube–polyelectrolyte thin films for strain and corrosion sensing," *Smart Materials and Structures*, Vol. 16, No. 2, 2007, pp. 429.

[118] Hou, T.-C. and Lynch, J. P., "Electrical impedance tomographic methods for sensing strain fields and crack damage in cementitious structures," *Journal of Intelligent Material Systems and Structures*, Vol. 20, No. 11, 2009, pp. 1363–1379.

[119] Hallaji, M. and Pour-Ghaz, M., "A new sensing skin for qualitative damage detection in concrete elements: Rapid difference imaging with electrical resistance tomography," *NDT & E International*, Vol. 68, 2014, pp. 13–21.

[120] Hallaji, M., Seppänen, A., and Pour-Ghaz, M., "Electrical resistance tomography to monitor unsaturated moisture flow in cementitious materials," *Cement and Concrete Research*, Vol. 69, 2015, pp. 10–18.

[121] Tee, B. C., Wang, C., Allen, R., and Bao, Z., "An electrically and mechanically self-healing composite with pressure-and flexion-sensitive properties for electronic skin applications," *Nature nanotechnology*, Vol. 7, No. 12, 2012, pp. 825–832.

[122] Lipomi, D. J., Vosgueritchian, M., Tee, B. C., Hellstrom, S. L., Lee, J. A., Fox, C. H., and Bao, Z., "Skin-like pressure and strain sensors based on transparent elastic films of carbon nanotubes," *Nature nanotechnology*, Vol. 6, No. 12, 2011, pp. 788–792.

[123] Mannsfeld, S. C., Tee, B. C., Stoltenberg, R. M., Chen, C. V. H., Barman, S., Muir, B. V., Sokolov, A. N., Reese, C., and Bao, Z., "Highly sensitive flexible pressure sensors with microstructured rubber dielectric layers," *Nature materials*, Vol. 9, No. 10, 2010, pp. 859–864.

[124] Abrate, S., "Impact on laminated composite materials," *Applied mechanics reviews*, Vol. 44, No. 4, 1991, pp. 155–190.

[125] Dubey, K., Mondal, R., Grover, V., Bhardwaj, Y., and Tyagi, A., "Development of a novel strain sensor based on fluorocarbon–elastomeric nanocomposites: Effect of network density on the electromechanical properties," *Sensors and Actuators A: Physical*, Vol. 221, 2015, pp. 33–40.

[126] Toprakci, H. A., Kalanadhabhatla, S. K., Spontak, R. J., and Ghosh, T. K., "Polymer Nanocomposites Containing Carbon Nanofibers as Soft Printable Sensors Exhibiting Strain-Reversible Piezoresistivity," *Advanced Functional Materials*, Vol. 23, No. 44, 2013, pp. 5536–5542.

[127] Zhang, N., *Electrical impedance tomography based on current density imaging*, 1992.

[128] Ider, Y. Z., Onart, S., and Lionheart, W. R., "Uniqueness and reconstruction in magnetic resonance–electrical impedance tomography (MR–EIT)," *Physiological measurement*, Vol. 24, No. 2, 2003, pp. 591.

[129] Ammari, H., Bonnetier, E., Capdeboscq, Y., Tanter, M., and Fink, M., "Electrical impedance tomography by elastic deformation," *SIAM Journal on Applied Mathematics*, 2008, pp. 1557–1573.

[130] Ammari, H., Garnier, J., and Jing, W., "Resolution and stability analysis in acousto-electric imaging," *Inverse Problems*, Vol. 28, No. 8, 2012, pp. 084005.

[131] Abascal, J.-F. P., Lionheart, W. R., Arridge, S. R., Schweiger, M., Atkinson, D., and Holder, D. S., "Electrical impedance tomography in anisotropic media with known eigenvectors," *Inverse Problems*, Vol. 27, No. 6, 2011, pp. 065004.

[132] Lionheart, W., “Conformal uniqueness results in anisotropic electrical impedance imaging,” *Inverse Problems*, Vol. 13, No. 1, 1997, pp. 125.

[133] Abascal, J.-F. P., Arridge, S. R., Atkinson, D., Horesh, R., Fabrizi, L., De Lucia, M., Horesh, L., Bayford, R. H., and Holder, D. S., “Use of anisotropic modelling in electrical impedance tomography; description of method and preliminary assessment of utility in imaging brain function in the adult human head,” *NeuroImage*, Vol. 43, No. 2, 2008, pp. 258–268.

[134] Adler, A. and Lionheart, W. R., “Uses and abuses of EIDORS: an extensible software base for EIT,” *Physiological measurement*, Vol. 27, No. 5, 2006, pp. S25.

[135] Boverman, G., Kim, B. S., Isaacson, D., and Newell, J. C., “The complete electrode model for imaging and electrode contact compensation in electrical impedance tomography,” *Engineering in Medicine and Biology Society, 2007. EMBS 2007. 29th Annual International Conference of the IEEE*, IEEE, 2007, pp. 3462–3465.

[136] Somersalo, E., Cheney, M., and Isaacson, D., “Existence and uniqueness for electrode models for electric current computed tomography,” *SIAM Journal on Applied Mathematics*, Vol. 52, No. 4, 1992, pp. 1023–1040.